191153

120 P

NASA Contractor Report 191550

A Feasibility Study of a Microgravity Enhancement System for Space Station Freedom

Preston S. Diamond
Robert H. Tolson

The George Washington University
Joint Institute for Advancement of Flight Sciences
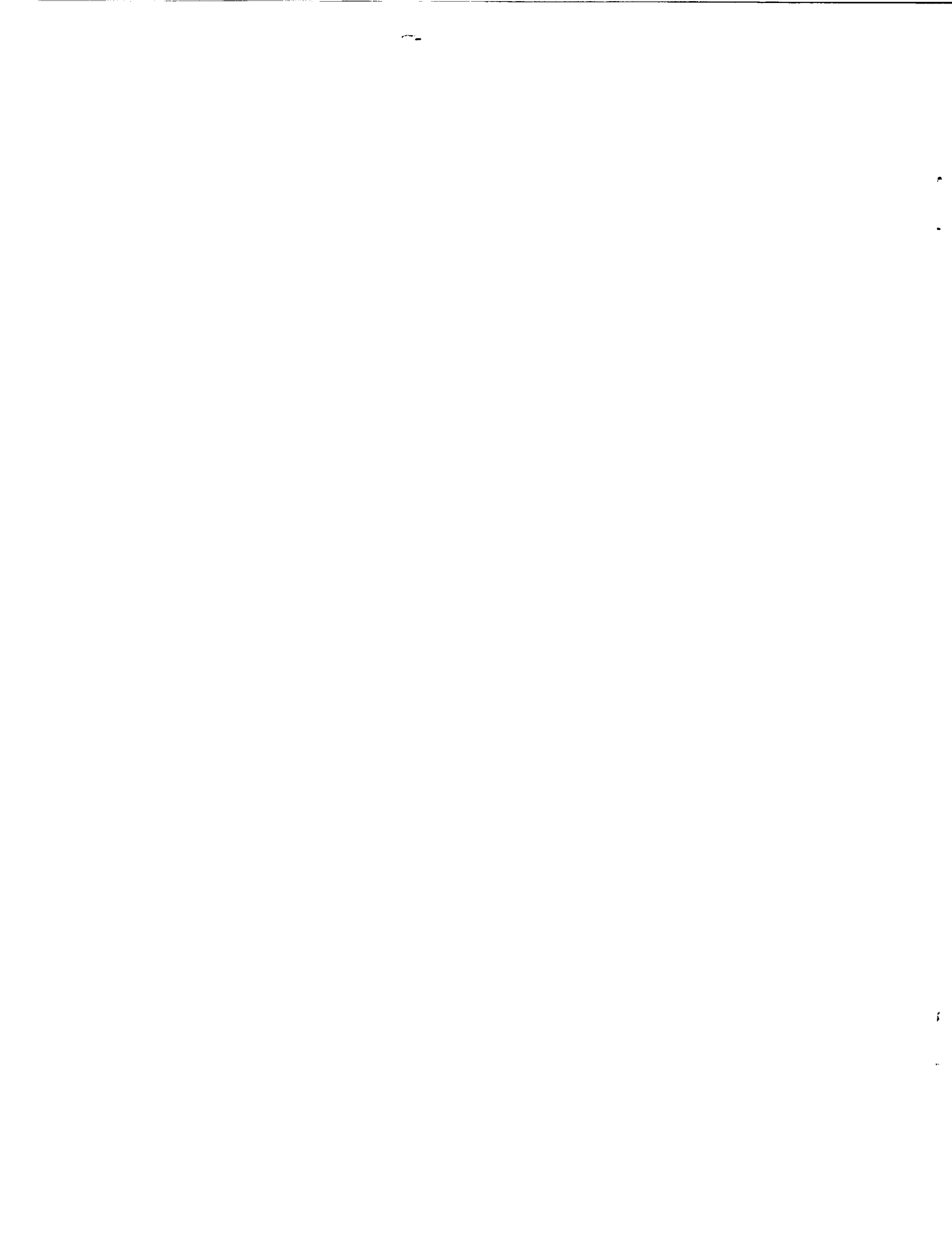Langley Research Center
Hampton, Virginia

Cooperative Agreement NCC1-104
October 1993

National Aeronautics and
Space Administration

Langley Research Center
Hampton, Virginia 23681-0001

ABSTRACT

The current low frequency microgravity requirements for Space Station Freedom (SSF) call for a level of less than 1 μ-g over 50% of all the laboratory racks for continuous periods of 30 days for at least 180 days per year. While this requirement is attainable for some of the laboratory modules for the Permanently Manned Configuration (PMC), it can not be met for the Man-Tended Configuration (MTC). In addition, many experiments would prefer even lower acceleration levels. To improve the microgravity environment, the Microgravity Enhancement System (MESYS) will apply a continuous thrust to SSF, to negate the disturbing gravity gradient and drag forces.

The MESYS consists of a sensor, throttle-able thrusters and a control system. Both a proof mass system and accelerometer were evaluated for use as the sensor. The net result of the MESYS will be to shift the microgravity contours from the center of mass to a chosen location. Results indicate the MESYS is not feasible for MTC since it will require 5,073 kg of hydrazine fuel and 7,660 watts of power for 30 days of operation during average atmospheric conditions. For PMC, the MESYS is much more practical since only 4,008 kg of fuel and 5,640 watts of power are required.

PAGE_____ INTENTIONALLY BLANK

TABLE OF CONTENTS

LIST OF FIGURES

LIST OF TABLES

NOTATION

A	Cross sectional area of SSF, m^2
a_d	Atmospheric drag acceleration, m/s^2
B	SSF ballistic coefficient, kg/m^2
c	Speed of light, m/s
C_d	Coefficient of drag
$c_y\ c_z$	Center of pressure, m
F	Total force, N
F_a	Atmospheric force vector, N
F_c	Control force, N
F_{css}	Steady state control force, N
$F_d\ F_{drag}$	Atmospheric drag force, N
F_l	Atmospheric lift force, N
F_s	Atmospheric side force, N
g	Acceleration due to gravity, 9.81 m/s
I	Moment of inertia matrix of SSF, kgm^2
$K_I\ K_P\ K_D$	Control gain matrices
L	3-2-1 transformation matrix from the orbital reference frame to the body reference frame
m	Mass of SSF, kg
N	Total torque, Nm
N_a	Atmospheric torque, Nm
N_c	Control torque, Nm
N_{gg}	Gravity gradient torques produced on SSF, Nm
P_{earth}	Earth radiation pressure, N/m^2
P_{solar}	Solar radiation pressure, N/m^2
R	Radius vector from center of the Earth to the proof mass, inertial reference frame, m
R_{cm}	Radius vector from the center of the Earth to the center of mass of SSF, inertial reference frame, m
R_e	Radius of the Earth, m
S	Solar constant, kw/m^2
v	Orbital velocity, m/s
$x\ y\ z$	Small displacement of proof mass wrt the center of the proof mass cavity, m
$x_0\ y_0\ z_0$	Position of the center of the proof mass cavity wrt SSF center of mass, body reference frame, m
α	Earth albedo
β	Reflectivity
Ω	Magnitude of ω_{orbit}, radians/second
$\theta_x\ \theta_y\ \theta_z$	Small angle displacements from, radians
$\theta_{x0}\ \theta_{y0}\ \theta_{z0}$	Angular displacement from orbital reference frame to body reference frame, radians

μ	Gravitational parameter
ρ	Atmospheric density, kg/m^3
ρ	Position vector from SSF center of mass to proof mass, m
ω	Angular velocity of SSF in inertial reference frame, radians/second
ω_{body}	Angular velocity of SSF in orbital reference frame, radians/second
ω_{orbit}	Angular velocity of orbital reference frame, radians/second

ABBREVIATIONS

ACS	Attitude Control System
DISCOS	Disturbance Compensation System
EUV	Extreme Ultraviolet
GP-B	Gravity Probe-B
GRM	Geopotential Research Mission
HiRAP	High Resolution Accelerometer Package
I_{sp}	Specific Impulse
ITA	Integrated Truss Assembly
JEM	Japanese Experiment Module
kg	kilogram
km	kilometer
kw	kilowatt
lb	pound
lbm	pound mass
LVLH	Local Vertical-Local Horizontal
m	meter
MESYS	Microgravity Enhancement System
MET	Marshall Engineering Thermosphere
MTC	Man-Tended Configuration
N	newton
nmi	nautical mile
PM	Propulsion Module
PMC	Permanently Manned Configuration
PPS	Primary Propulsion System
OARE	Orbiter Acceleration Research Experiment
REM	Rocket Engine Module
SSF	Space Station Freedom
TCS	Thermal Control System
TDRSS	Tracking and Data Relay Satellite System

1.0 INTRODUCTION

1.1 STATEMENT OF PROBLEM

Microgravity experiments are expected to make up a large portion of the experiments performed on Space Station Freedom (SSF). The current requirements state that from Man Tended Configuration (MTC) a minimum of 50% of all user payload racks in each of the pressurized laboratories and a minimum of 50% of the Japanese Experiment Module (JEM) Exposed Facility shall have acceleration levels not exceeding 1×10^{-6} g at frequencies less than or equal to 0.1 Hz for continuous periods of at least 30 days for at least 180 days per year[1]. There are two major forces which combine to erode the microgravity environment on SSF: atmospheric drag and gravity gradient forces resulting from the fact that the laboratory module is not at the center of mass of SSF. While this requirement is achievable, it is dependant on atmospheric drag forces, which are in turn dependant on orbital altitude and solar activity. Combinations of high solar activity and low altitudes will violate this requirement. In addition, even lower acceleration levels would be preferable for many experiments. Figure 11-1 shows the desired acceleration levels for several material processes and the acceleration requirements for SSF[2]. Standard vibration isolation methods can be used to meet the requirements in the upper frequency range and newer techniques can be used in the middle frequency range. However, there is currently no plan to control accelerations in the low frequency range.

In order to take full advantage of the facilities on SSF, a way should be found to guarantee that the microgravity requirements can be met, regardless of the atmospheric conditions or mass distribution of SSF. Also, a way should be found to meet the low frequency microgravity requirements of planned experiments.
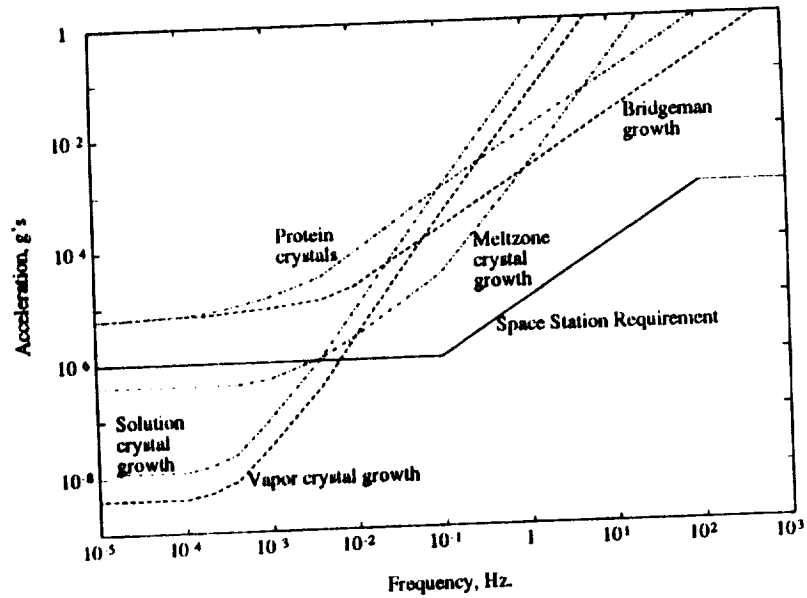
Figure 11-1 Desired microgravity levels for various experiments[2].

1.2 MESYS CONCEPT

To improve the microgravity environment on SSF, a continuous thrust could be applied to SSF in such a way as to cancel the disturbing drag and gravity gradient forces. This improvement would be achieved by adding a Microgravity Enhancement SYStem (MESYS) to SSF. The MESYS is composed of: a sensor to detect the disturbing forces (either a proof mass or the Orbital Acceleration Research Experiment (OARE) accelerometer, both described below), 10 or 20 low thrust throttle-able arcjet thrusters and a feedback control system. This paper will compare the performance of both the proof mass sensor and the OARE accelerometer and will recommend one of them based on their performance and cost. All studies performed in this paper were derived for use on the 6th stage of construction of SSF known as Man-Tended Configuration (MTC) and will include an analysis of requirements for use on the 17th and final stage of construction of SSF, known as Permanently Manned Configuration (PMC).

There are advantages and disadvantages for using either the proof mass or OARE

accelerometer. The proof mass has an advantage in that it is comprised of simple, proven technology with no moving parts, while the OARE must be calibrated by rotating the sensor platform. The OARE has an advantage in that by changing a few constants in the control system, any point on SSF can be chosen to have optimal microgravity conditions. With the proof mass system, only that point where the proof mass is located has optimal conditions.

The MESYS must use a continuous control system because the bang-bang system would place momentary accelerations on SSF that would destroy the microgravity environment. Further, the system has to cancel the drag continuously if an ideal environment is to be created for microgravity experiments. This is why low thrust throttle-able arcjet thrusters were chosen for use. They have the ability to operate continuously and have a high specific impulse for efficient operation.

1.3 DRAG FREE CONCEPT

The MESYS works on the principle of the 'drag free' satellite which was first proposed by Lange in 1964[3]. A satellite achieves drag free flight by sensing disturbing forces and then firing thrusters to cancel them. Satellites have historically used a proof mass system (described below) to sense the disturbing forces but recent advances in technology have lead to accelerometers such as the HiRAP and OARE (described below) that are a viable alternative to the proof mass systems. Previous and planned satellites use either a continuous control system or a discrete (bang-bang) control system. In a continuous control system, throttle-able thrusters continuously apply the compensation force canceling the disturbance. In a bang-bang control system, when the non-gravitational forces produce a predetermined disturbance on the satellite,

fixed thrust thrusters fire. These thrusters inevitably over compensate and the satellite is left to 'drift' until the disturbing forces again produce sufficient disturbance causing the thrusters to fire again, repeating the cycle. A satellite with a bang-bang system is considered drag free because the net force acting on it averages to zero over a period of time, whereas a satellite with a continuous control system is drag free at any point in time. The TRIAD satellite and the proposed Geopotential Research Mission (GRM) satellite use a bang-bang proof mass system while the proposed Gravity Probe-B satellite uses the continuous proof mass system. All three are described below.

1.3.1 Proof Mass Systems

The drag free concept was successfully demonstrated for the first time in 1972 when the U.S. Navy sponsored the experimental TRIAD satellite. The satellite contained a DISturbance COmpensation System (DISCOS) designed to reduce all external accelerations on the satellite to below 10^{-11} g's. DISCOS consists of a 22 mm diameter metal ball, or proof mass, placed in a 40 mm diameter cavity in the TRIAD satellite. The satellite shields the proof mass from non-gravitational forces such as radiation pressure, atmospheric drag and micrometeorite impacts. Thus, the proof mass trajectory is purely gravitational. As non-gravitational forces perturbed the orbit of the outer satellite, the proof mass moves within the cavity. This motion is detected by electrostatic sensors on the wall of the cavity. Once the proof mass moves more than 1 mm from the center, gas jets in a bang-bang control system propel the satellite so that the proof mass returns to the center of the cavity. Ground tracking of the 849 by 760 km polar orbit confirmed that the proof mass was free of all external disturbances to better than $<10^{-11}$ g's when averaged over the satellite's life[4]. The proof mass concept is described in greater detail in section 2.2.2.

The drag free concept will also be implemented with the Stanford Gravity Probe-B Relativity Gyroscope Experiment (GP-B) satellite. The satellite will test two unproven consequences of Einstein's general theory of relativity which predicts two orthogonal precessions for a Newtonian gyroscope placed in a polar orbit. These precessions are known as geodetic and frame-dragging precessions and are predicted to be 6.6 arc-sec/yr and 0.042 arc-sec/yr, respectively, for a 650 km orbit. In order to detect the precession, all non-gravitational forces must be canceled to below 10^{-10} g's[5]. To accomplish this, a 38 mm diameter proof mass will be placed in a 38.2 mm diameter cavity to achieve 'drag-free' flight. Boil off from the liquid helium used to cool the experiment gyros will be used in the proportional thrusters to cancel the disturbing forces[5]. A unique feature of the GP-B is that the drag free control system will run out of fuel at the same time that the gyros are no longer cooled and lose their effectiveness.

In the early 1980's, NASA proposed the Geopotential Research Mission (GRM) to determine high precision gravitational and magnetic fields of the Earth over the entire globe. The GRM experiment (once referred to as GRAVSAT/MAGSAT) called for two drag free satellites in coincident 160 km polar orbits. The satellites will be separated by 100 to 600 km. An on board Satellite-to-Satellite Tracking system (SST) will be used to calculate the line of sight range-rates between the two satellites. A disturbance compensation system similar to TRIAD's will be used to control the satellites through a bang-bang control system. With the DISCOS in operation, the two satellites will be extremely sensitive to the gravity field. Data from the SST will then be used to accurately map variations in the gravity potential as the satellites orbit. It was estimated that each satellite would require between 763 kg and 1056 kg of fuel for 6 months of operation[6].

1.3.2 Accelerometers

In addition to these satellites using the proof mass concept, there have been advances in accelerometer technology. Since 1983, several Space Shuttle missions have flown the High Resolution Accelerometer Package (HiRAP). The HiRAP is a tri-axial, 1×10^{-6} g resolution, pendulous, gas-damped accelerometer designed to measure low-frequency aerodynamic accelerations. A disadvantage of the HiRAP accelerometer is the required ground calibration factors and flight derived calibration factors[7].

As a follow-on to the HiRAP accelerometer, the Orbital Acceleration Research Experiment (OARE) accelerometer was designed in the late 1980's. The OARE has flown twice on the Space Shuttle. It uses an electrostatically balanced cylindrical proof mass accelerometer with three orthogonal axis outputs and has three scale settings that allow resolution to 3.2 nano-g's. To achieve nano-g resolution, OARE contains a precision in-flight calibration subsystem to compute scale factor and bias[8]. The OARE accelerometer is described in greater detail in section 2.2.1.

1.4 CONTROLLING GRAVITY GRADIENT ACCELERATIONS

As stated above, the TRIAD and the planned GP-B will use the drag fee concept to compensate primarily for atmospheric disturbance. Using the concept to compensate for gravity gradient disturbances is a new concept. To get an idea of how the concept works and the magnitude of control system thrust required, consider the following examples. A satellite with a proof mass is placed in orbit at an altitude h and the proof mass is assumed to be in a purely 2-body circular orbit with the Earth. Let the proof mass be placed a distance d from the center

of mass in the Z (cross track) direction (see Figure 14-1). The acceleration vector of the proof mass is in the x direction only while the acceleration vector of the spacecraft has a component in the z direction. This component is given by

$$
a_z = g_{cm}\sin\theta = \frac{\mu}{(R_e+h)^2} \frac{d}{(R_e+h)}
$$

$$
= \frac{\mu d}{(R_e+h)^3}
$$

(14-1)

To negate this acceleration so that the relative position of the proof mass does not change throughout the orbit, a thrust of ma_z applied to the spacecraft in the -Z direction will cause the center of mass to remain in line with the proof mass. SSF has a mass m of 90,000 kg and orbits at an altitude of 407 km. Assuming d is 10 m, the thrust required is 1.15 newtons.
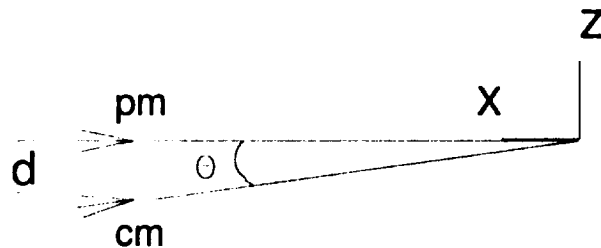
Figure 14-1 Proof mass displaced in the cross track direction.

Now suppose the proof mass is placed a distance d in the radial direction toward the Earth (see Figure 14-2). By definition, in a circular orbit, the gravitational force acts in the radial direction toward the attracting body is exactly canceled by the centripetal force of the satellite, which is equal to the orbital angular velocity squared times the orbit radius. i.e. $g_{local} = \Omega^2 r$.

Since in this case the proof mass is in a lower orbit, it feels a greater gravitational acceleration and therefore has a greater angular velocity. With no control system, the proof mass will have a greater orbital angular velocity than the center of mass and the two will not remain radially aligned. But, if we 'trick' the center of mass into believing it is in a lower orbit by adding to the gravitational acceleration acting on it, the center of mass will orbit at a greater angular velocity. The difference in acceleration between the proof mass and center of mass is given by

$$\Delta a = \frac{\mu}{(R_e + h - d)^2} - \frac{\mu}{(R_e + h)^2}$$
$$\approx \frac{2\mu d}{(R_e + h)^3} \tag{14-2}$$

A thrust of $m\Delta a$ applied in the radial direction toward the Earth will be required to keep the proof mass and center of mass radially aligned. Using the same values as above, this force is 2.30 newtons.
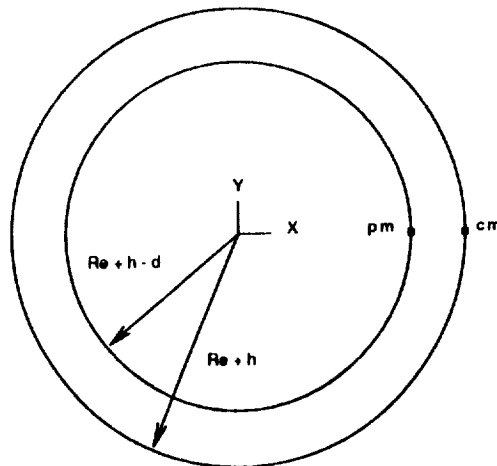
Figure 14-2 Proof mass displaced in the radial direction.

And finally, suppose the proof mass is placed a distance d in front of the center of mass, in the Y direction (see Figure 14-3). To a first order approximation, the proof mass is still in the same orbit as the center of mass and therefore not move with respect to the center of mass.
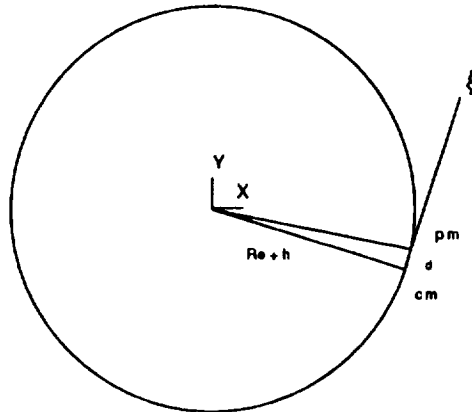
Figure 14-3 Proof mass displaced in the along track direction.

Remember that these analyses are approximate because of the small displacement assumption and not all dynamical effects are included here.

2.0 MESYS HARDWARE

This chapter describes the hardware necessary to implement the MESYS. This includes the general configuration of SSF, the accelerometers that will be studied and the arcjets that will be required.

2.1 SPACE STATION FREEDOM

For this study, all references to SSF refer to the configuration which emerged from the restructuring activity performed between January and June of 1991. The design calls for 17 assembly flights of the Space Shuttle to reach the final stage, known as Permanently Manned Configuration (PMC) as shown in Figure 21-1. As of this writing, the assembly flights were to
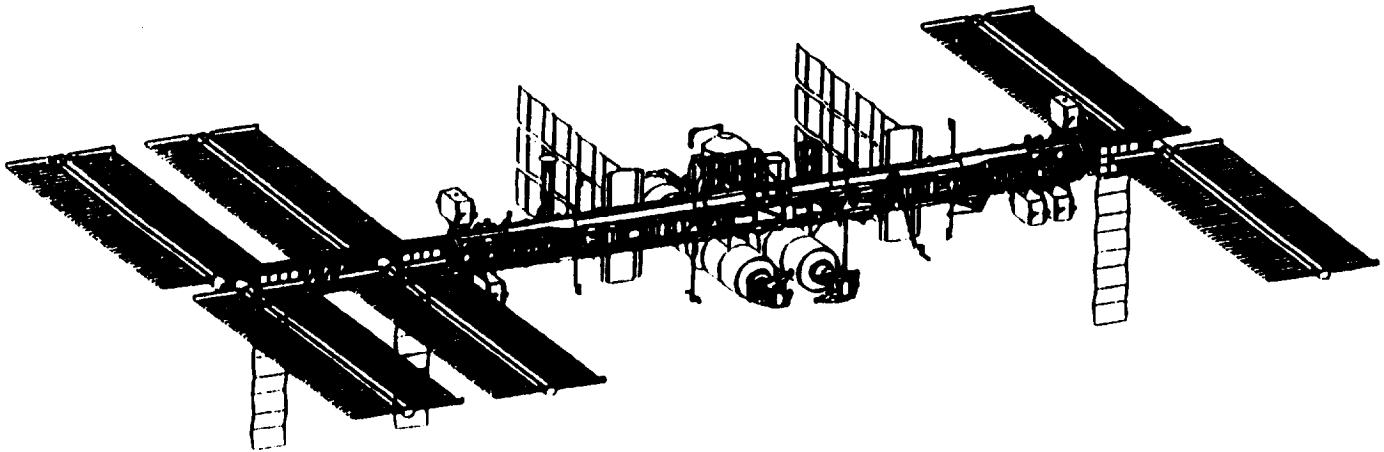
Figure 21-1 Space Station Freedom, Permanently Manned Configuration.

have taken place between 1997 and 2000.

2.1.1 Man-Tended Configuration

After the sixth assembly flight, SSF will have reached a milestone known as Man-Tended
Configuration (MTC). It is at this point at which astronauts will be able to temporarily man the
station to make use of the laboratory facilities. In relation to PMC, MTC will consist of half the
main truss, 2 of the 6 propulsion modules, 1 pair of the 3 pairs of solar arrays, 1 of the 2 node
modules, 1 of the 2 Thermal Control System (TCS) radiator arrays and the U.S. laboratory
module (see Figure 21-2).
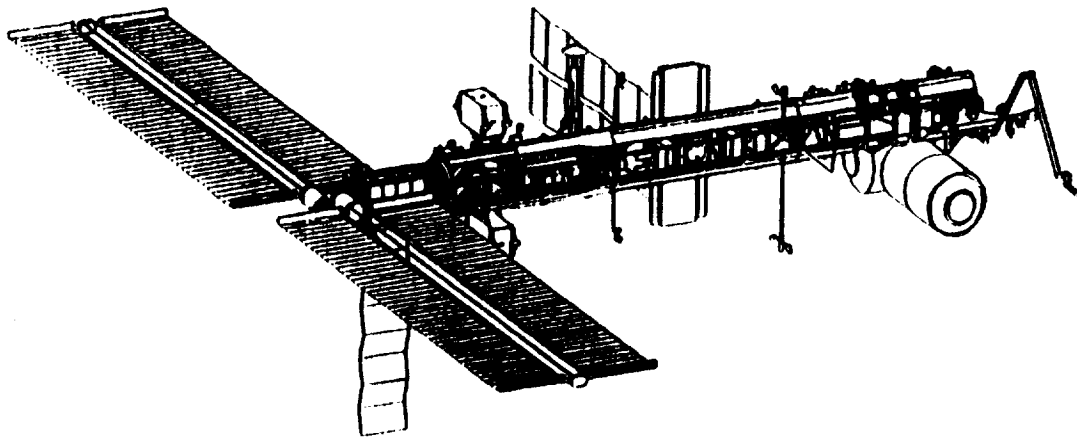
Figure 21-2 Space Station Freedom, Manned-Tended Configuration.

SSF MTC has the following properties:

Mass: 91,880 kg (202,550 lbm)

$$I: \begin{vmatrix} 2.2980 \times 10^7 & -3.4703 \times 10^5 & 5.4791 \times 10^5 \\ -3.4703 \times 10^5 & 2.5275 \times 10^6 & 2.1013 \times 10^6 \\ 5.4791 \times 10^5 & 2.1013 \times 10^6 & 2.3555 \times 10^7 \end{vmatrix} \ \text{kg m}^2$$

Center of Mass: $| -0.396 \quad 9.685 \quad 1.75 |$ m

Center of Pressure, x face $| \ 0 \quad 14.787 \quad 3.335 |$ m

Ballistic Coefficient: 52.9 kg/m^2

Total Power Available: 18.75 kw

Total Propellant Available: 9,120 kg

The center of mass and all other positions listed in this study are measured in the Space Station Analysis Coordinate System centered at the geometric center of the middle Integrated Truss Assembly (ITA) (see Figure 21-3). The x-axis is perpendicular to the ITA and is positive in the nominal LVLH flight direction. The y-axis is along the longitudinal axis of the ITA and is positive toward starboard. The z-axis is positive toward nadir and completes the right-handed system[9].
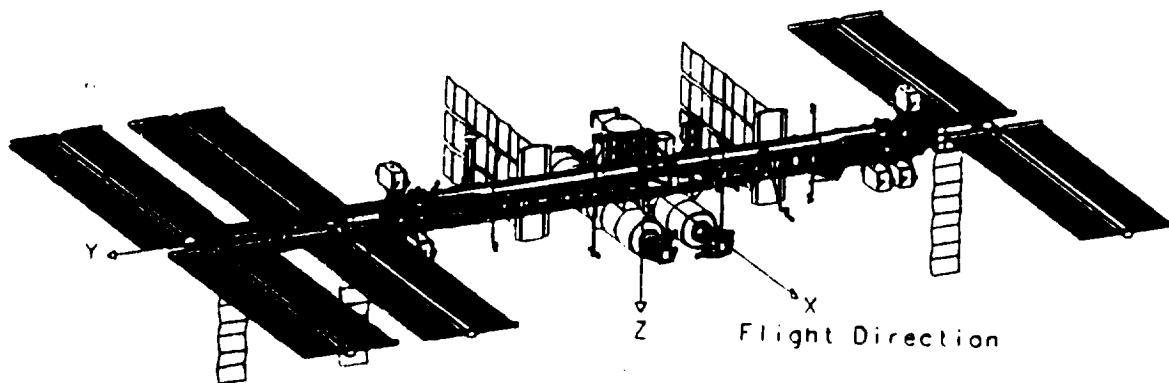
Figure 21-3 Space Station Analysis Coordinate System.

2.1.2 Permanently Manned Configuration

SSF PMC has the following properties:

Mass: 274,700 kg (604,340 lbm)

$$I: \quad \begin{vmatrix} 1.0972 \times 10^8 & -1.9664 \times 10^6 & 2.1422 \times 10^6 \\ -1.9664 \times 10^6 & 1.4940 \times 10^7 & 1.7168 \times 10^6 \\ 2.1422 \times 10^6 & 1.7168 \times 10^6 & 1.1896 \times 10^8 \end{vmatrix} \quad kg\ m^2$$

Center of mass: $| \ -2.424 \quad 1.744 \quad 2.321 \ | \quad m$

Center of Pressure, x face: $| \ 0 \quad 7.627 \quad 0.4060 | \quad m$

Ballistic Coefficient: $60.8 \ kg/m^2$

Total Power Available: 75 kw

Total Propellant Available: 27,360 kg

2.1.3 Laboratory Module Layout

There are 24 experiments racks in the laboratory module. The racks are divided equally along the ceiling, starboard wall, floor and port wall. Figure 21-4 shows the laboratory module layout and rack nomenclature. Table 21-1 lists the approximate location of each rack measured in the Space Station Analysis Coordinate System. Note that the table lists only the first 5 racks along the ceiling, walls and floor. The sixth rack contains system and storage equipment and will be ignored when evaluating the microgravity environment. For this study, the centroid of the laboratory module is assumed to be at $| \ 2.33 \quad -3.25 \quad 4.85 \ |$ meters[10]. All references to the laboratory module will refer to this specific point.
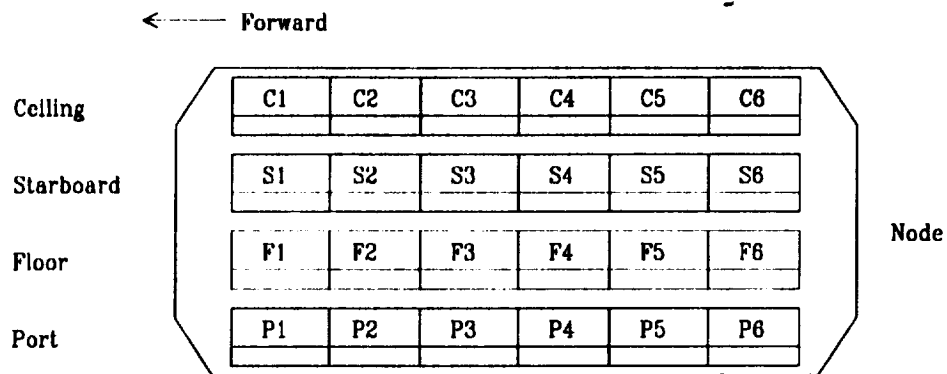
Figure 21-4 Laboratory experiment rack layout and nomenclature.

Table 21-1 Experiment Rack locations.

	Rack 1	Rack 2	Rack 3	Rack 4	Rack 5
Ceiling	4.13 -3.25 3.23	3.40 -3.25 3.23	2.69 -3.25 3.23	1.97 -3.25 3.23	1.25 -3.25 3.23
Starboard	4.13 -1.63 4.85	3.40 -1.63 4.85	2.69 -1.63 4.85	1.97 -1.63 4.85	1.25 -1.63 4.85
Floor	4.13 -3.25 6.47	3.40 -3.25 6.47	2.69 -3.25 6.47	1.97 -3.25 6.47	1.25 -3.25 6.47
Port	4.13 -4.87 4.85	3.40 -4.87 4.85	2.69 -4.87 4.85	1.97 -4.87 4.85	1.25 -4.87 4.85

2.1.4 Flight Orientations

There are 2 primary flight orientations for SSF: Local Vertical-Local Horizontal (LVLH), and Arrow. Under normal operations, SSF will orbit in the LVLH flight mode. In LVLH, the x-axis is aligned in the direction of flight and the z-axis is aligned with nadir (see Figure 21-5).

Arrow flight mode is achieved by a -90° rotation about the LVLH z-axis which results in the station y-axis aligning with the positive LVLH x-axis (see Figure 21-5). Reboost will occur in the Arrow flight orientation[9].

2.1.5 Orbit Altitude Strategy

SSF is to be expected to be reboosted 4 times per year, approximately 90 days apart. Reboost will occur shortly after the departure of the Space Shuttle and SSF will be allowed to decay over the next 90 day period until the next Shuttle rendezvous. Reboost altitude is that starting altitude at which after 270 days, SSF will have decayed to the minimum allowable altitude of 150 nm (277.8 km). For this study, it is assumed that this reboost altitude will vary between 200 nm and 240 nm (370.4 km and 444.5 km), depending on solar activity[9].

2.1.6 Propulsion System

The Primary Propulsion System (PPS) on MTC consists of 2 self-contained Propulsion Modules (PMs) (see Figure 21-6) located on the upper and lower sides of the starboard ITA. Each PM contains both reboost and Attitude Control System (ACS) thrusters. The reboost thrusters are located on the aft end of the PM to provide a velocity change in the +X LVLH direction. Since reboost for MTC will occur in the Arrow flight mode, the reboost thrusters will not be used until after the ninth assembly flight when the port side PMs are attached. The ACS thrusters are refurbishable monopropellant hydrazine thrusters located on five sides of each PM to provide attitude control in those five directions. The thrusters operate in a blowdown system and have a thrust range of 25 to 9 lbf (111.1 to 40.0 N). There are 5 ACS Rocket Engine Modules (REMs) containing 2 thrusters each on each PM. Each PM has 6 titanium propellant tanks containing up to 1672 lbm (760 kg) of hydrazine in each tank for a total of 10,032 lbm

(a) MTC LVLH Flight Mode

b_2 ← Y

X (Flight Path) b_1

Z (Nadir) b_3

(b) MTC Arrow Flight Mode

Y ←

X (Flight Path)

Z (Nadir)
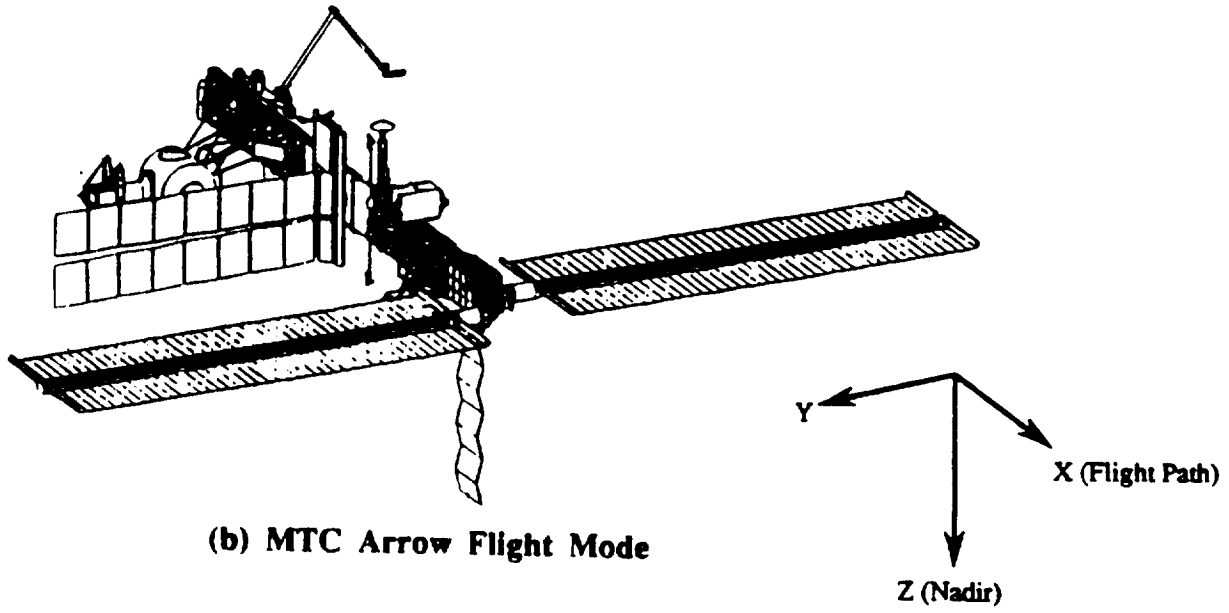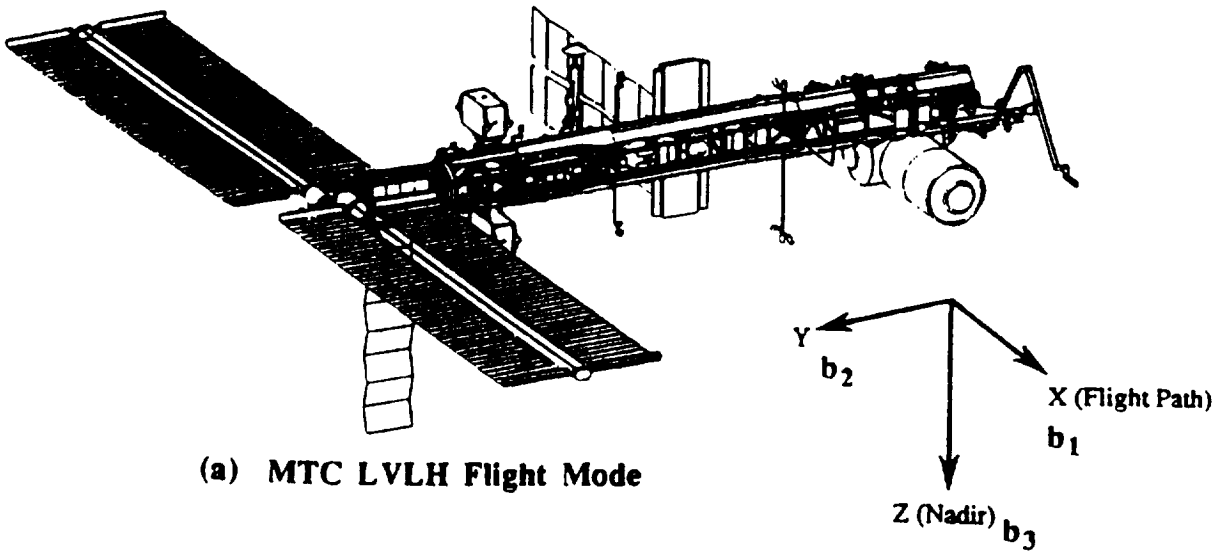
Flight Orientation	X	Y	Z
LVLH	b_1	b_2	b_3
Arrow	b_2	$-b_1$	b_3

(c) Coordinate Relationships

Figure 21-5 SSF flight orientations.

(4560 kg) of propellant per PM[11].
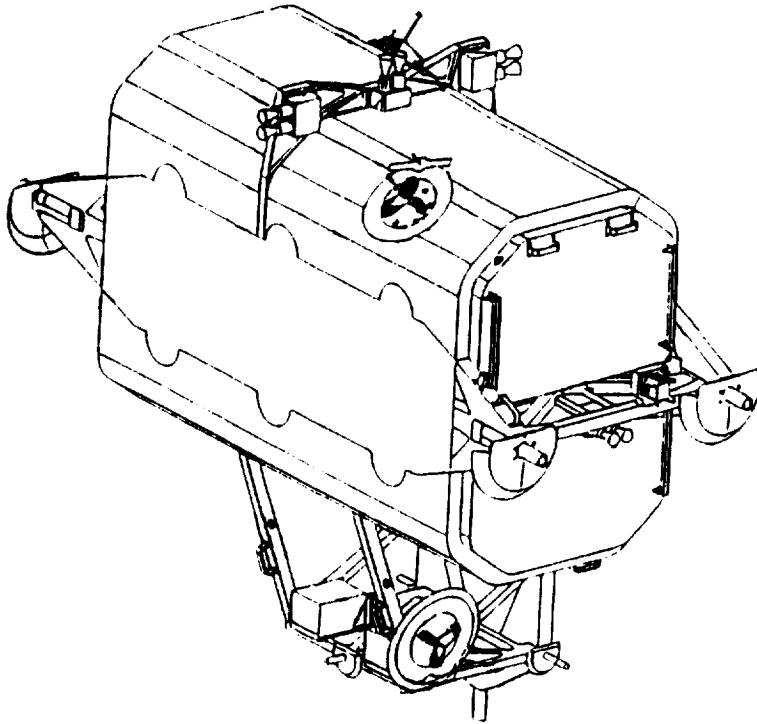
Figure 21-6 SSF Propulsion Module.

2.1.7 Attitude Control System

The MESYS will be tested on a high fidelity model of the nominal SSF attitude control system. The model was written in MatrixX and System Build software and has been compared extensively with accepted models of the attitude control system. In the simulation, the error between the commanded orientation and the actual orientation (represented by a set of Euler angles) along with the error in the commanded and actual angular velocity are the input into the

controller and a request control torque is the output. A jet select logic function selects a group of six of the ten thrusters to apply this control torque. Since the SSF ACS thrusters have a fixed output, the function also selects the firing time required for each thruster so that the proper thrust is applied. The system updates attitude data continuously and the applied thrust is updated every 33 seconds. The total torque (the sum of the control torque, gravity gradient torque and aerodynamic torque) is integrated in the dynamic and kinematic equations to calculate the new orientation and angular velocity. The errors between this output and the commanded values is then used to calculate a new control torque and the cycle repeats[12].

2.2 ACCELEROMETERS

Perhaps the most important item in a disturbance compensation system is the accelerometer. It is impossible to correct disturbances below the level at which the accelerometer can detect. Two different accelerometers were evaluated. They are the Orbital Acceleration Research Experiment (OARE) accelerometer and the proof mass concept used on the U.S. Navy's TRIAD satellite. Both accelerometers are described below.

2.2.1 OARE

The OARE accelerometer was built to continue earlier experiments to investigate the aerodynamic acceleration environment on the Shuttle. It uses an electrostatically balanced cylindrical proof mass accelerometer with tree orthogonal sensing axes outputs. The OARE accelerometer samples data at a rate of 10 hz. A trimmed-mean filter is used to process the raw data to remove high frequency noise. The filter works as follows: first data in a data window is ordered from low to high value. A "quality index", which is a measure of the scatter of the

2-9

data from noise, is then calculated. The quality index is used to calculate the value alpha which is the portion of the data to be removed from the high and low ends. Alpha can range from 0.05 to 0.40. The remaining data is then averaged. The OARE accelerometer has three scale settings that allow a resolution down to 3.2 nano-g's[13].

Perhaps the most important feature of the OARE accelerometer is the ability to be calibrated in-flight. The subsystem employed for calibration consists of an inner gimbal (azimuth) axis bearing mounted in a yoke assembly. The yoke is rotated by an outer gimbal (elevation) axis bearing mounted on the base structure. Each axis contains a separate torque motor. In-flight calibration may be accomplished by the following procedure. Moving between positions 180° apart and differencing the output readings gives twice the applied acceleration, free of bias error; summing the two readings gives twice the bias. Driving the turntable at two accurately controlled rates and then differencing the output readings gives a scale factor calibration. Recording the temperature of the sensor at the time of each calibration will allow models of bias and scale factor behavior to be developed, with the possibility of eventually reducing the frequency of calibrations[8]. The OARE has flown successfully of STS-40 and STS-50 and is planned to fly on STS-58.

2.2.2 The Proof Mass Concept

The proof mass accelerometer is a relatively simple device. A spherical proof mass is placed in an evacuated chamber, which is rigidly attached to some point on the satellite. This will isolate the proof mass from all non-gravitational forces, such as atmospheric and solar pressure drag. The proof mass is spherical to eliminate any gravitational torques. Therefore, the proof mass will be in a pure gravitational orbit about the Earth. When external forces act on the

2-10

body of the satellite, the proof mass will move relative to the cavity. This movement will be detected and thrusters on the satellite will be fired to move the satellite so that the proof mass is re-centered in the cavity.

The TRIAD satellite was launched on September 2, 1972 and operated continuously until mid-September, 1973. TRIAD's DISturbance COmpensation System (DISCOS) consisted of a 22 mm diameter proof mass placed in a 40 mm diameter spherical cavity, on the surface of which contained six plates. The six plates, when taken in pairs, form three orthogonal sensor axes. The proof mass forms a nearly perfect spherical conductor. The spherical conductor is electrostatically coupled with each of the six plates located on the surface of the housing. As the proof mass approaches one of the housing plates, the capacitance from the ball to that plate increases inversely with the distance. This change in capacitance signals the six cold gas jets to fire and recenter the proof mass in the cavity. Ground tracking of the orbit confirmed that the proof mass can be considered free of all external disturbances to below 10^{-11} g's when its' motion was averaged over 6 months[4].

2.3 THRUSTERS

2.3.1 Arcjets

Conceptually, the operation of an arcjet is very simple. Propellant is heated directly by an electric arc and expanded through a supersonic nozzle to convert the increased thermal energy to directed kinetic energy and produce thrust. The propellant can be heated to temperatures greatly exceeding material limits and provide specific impulse levels much greater than resistojets and chemical rockets, whose propellant enthalpy levels are limited by the maximum material

temperature and by energy evolved through chemical reactions, respectively[14].

Work on arcjet technology began in the late 1950's and proceeded into the late 1960's when interest dropped due to a lack of an adequate electrical power supply. Interest was reborn in the early 1980's with the introduction of new, low power arcjet thrusters available for north-south station keeping of communication satellites.

Arcjet thrusters can be throttled by two methods: adjusting the power to control the arc temperature and adjusting the fuel flow rate. Adjusting the power to the arc produces a slow thrust response due to the delay in the thermal response. Adjusting fuel flow rate, however, produces a very quick response in the force. Although it has not been demonstrated, it is estimated that current state of the art arcjets have a dynamic range of at least 3.

2.3.2 Thruster Locations

Twenty low thrust, throttle-able thrusters will be added to the propulsion modules on SSF. Table 23-1 shows the thruster positions and firing directions.

Thrusters 1 through 5 are on the top starboard propulsion module, 6 through 10 are on the bottom starboard propulsion module and are the only thrusters for MTC. PMC uses those thrusters plus thrusters 11 through 15, which are on the top port propulsion module and thrusters 16 through 20, which are on the bottom port propulsion module. Also, the location is in meters relative to the Space Station Analysis Coordinate System and the firing directions are relative to LVLH orientation.

Table 23-1 Thruster locations and firing directions.

Thruster #	Location	Firing direction
1	-3.17, 31.41, -4.40	1, 0, 0
2	1.20, 31.41, -4.16	-1, 0, 0
3	-3.17, 30.47, -5.54	0, 1, 0
4	1.20, 32.34, -5.54	0, -1, 0
5	-0.10, 31.41, -5.71	0, 0, 1
6	-3.17, 32.00, 4.40	1, 0, 0
7	1.20, 32.09, 4.16	-1, 0, 0
8	1.20, 31.08, 5.54	0, 1, 0
9	-3.17, 32.95, 5.54	0, -1, 0
10	-0.10, 32.00, 5.71	0, 0, -1
11	-3.17, -31.41, -4.40	1, 0, 0
12	1.20, -31.41, -4.16	-1, 0, 0
13	-3.17, -30.47, -5.54	0, 1, 0
14	1.20, -32.34, -5.54	0, -1, 0
15	-0.10, -31.41, -5.71	0, 0, 1
16	-3.17, -32.00, 4.40	1, 0, 0
17	1.20, -32.09, 4.16	-1, 0, 0
18	1.20, -31.08, 5.54	0, 1, 0
19	-3.17, -32.95, 5.54	0, -1, 0
20	-0.10, -32.00, 5.71	0, 0, -1

3.0 MATHEMATICAL DEVELOPMENTS

3.1 COORDINATE SYSTEMS AND FORCE MODELS

This section describes the coordinate systems and disturbing force models used in this paper.

3.1.1 Coordinate Systems

There are three coordinate systems of interest: an inertial reference frame, an orbital reference frame and a body (SSF) fixed reference frame. The inertial reference frame (X,Y,Z) has the origin at the center of the Earth (see Figure 31-1). X points in the direction of the vernal equinox, Z points toward the celestial north pole and Y completes the right handed system. In the orbital reference frame (ξ,η,ζ), η is perpendicular to the orbit plane in the direction opposite the orbital angular momentum vector, ζ points toward nadir and ξ completes the right hand system. Figure 31-2 shows the relationship between the orbital reference frame and the body reference frame. The body reference frame (x,y,z) is achieved through a 3-2-1 rotation from the orbital reference frame.

The 3-2-1 rotation matrix from the orbital to body reference frames is given by

$$L = \begin{bmatrix} \cos\theta_z\cos\theta_y & \sin\theta_z\cos\theta_y & -\sin\theta_y \\ \cos\theta_z\sin\theta_y\sin\theta_x - \sin\theta_z\cos\theta_x & \sin\theta_z\sin\theta_y\sin\theta_x + \cos\theta_z\cos\theta_x & \cos\theta_y\sin\theta_x \\ \cos\theta_z\sin\theta_y\cos\theta_x + \sin\theta_z\sin\theta_x & \sin\theta_z\sin\theta_y\cos\theta_x - \cos\theta_z\sin\theta_x & \cos\theta_y\cos\theta_x \end{bmatrix} \qquad (31\text{-}1)$$

3.1.2 Gravitational Torques
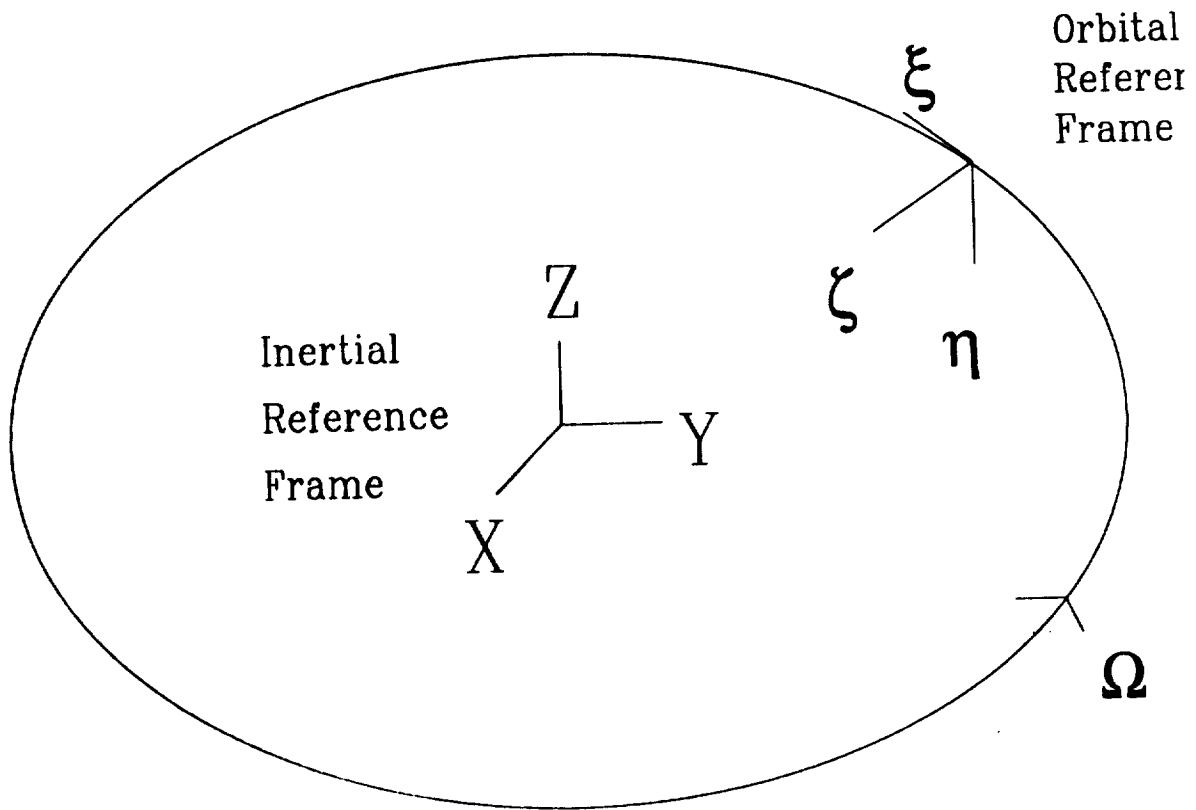
Figure 31-1 Inertial and orbital reference frames.

Gravitational torques are produced on an object in a central force gravitational field if that object does not possess spherical symmetry. Gravity gradient torques in this study were calculated using the following formulas[15]

$$
N_{gg} = \frac{3\mu}{|R_{cm}|^2}
\begin{bmatrix}
\left\{ L_{32}L_{33}(I_{zz}-I_{yy}) + L_{31}L_{33}I_{xy} - L_{31}L_{32}I_{xz} + (L_{33}^2-L_{32}^2)I_{yz} \right\} \hat{i} \\
\left\{ L_{31}L_{33}(I_{xx}-I_{zz}) + L_{31}L_{33}I_{yz} - L_{32}L_{33}I_{xy} + (L_{31}^2-L_{33}^2)I_{xz} \right\} \hat{j} \\
\left\{ L_{31}L_{32}(I_{yy}-I_{xx}) + L_{32}L_{33}I_{xz} - L_{31}L_{33}I_{yz} + (L_{32}^2-L_{31}^2)I_{xy} \right\} \hat{k}
\end{bmatrix}
\tag{31-2}
$$

where L_{ij} are the rotation matrix elements and I_{ij} are the moments of inertia.
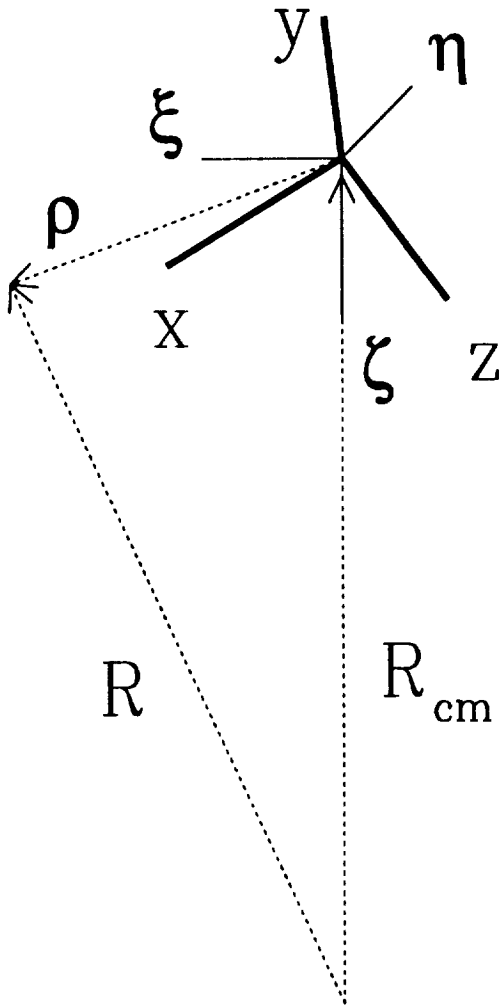
Figure 31-2 Orbital and body reference frames.

3.1.3 Atmospheric Forces and Torques

The forces the atmosphere exerts on SSF can be expressed as follows[16]

3-3

$$F_a = \begin{bmatrix} F_d \\ F_l \\ F_s \end{bmatrix} \qquad\qquad (31\text{-}3)$$

This study assumes that the lift (F_l) and side (F_s) forces are negligible and will be ignored. Atmospheric drag is computed from the formula[16]

$$F_d = \frac{1}{2}\rho C_d A v^2 \qquad\qquad (31\text{-}4)$$

where v is the orbital speed, A is the area perpendicular to the direction of motion, C_d is the drag coefficient and ρ is the atmospheric density. Dividing Eq. (31-4) by the mass of SSF results in

$$
\begin{aligned}
a_d = \frac{F_d}{m} &= \frac{1}{2}\frac{C_d A}{m}\rho v^2 \\
&= \frac{\rho v^2}{2B}
\end{aligned}
\qquad\qquad (31\text{-}5)
$$

where B is the ballistic coefficient, defined by $\dfrac{m}{C_d A}$ [16] and is listed in section 2.1.1.

The torque produced by atmospheric forces will be modeled as

$$N_a = \begin{bmatrix} 0 \\ c_z F_d \\ -c_y F_d \end{bmatrix} \qquad\qquad (31\text{-}6)$$

3-4

where c_y and c_z gives the location of the center of pressure of x direction face of SSF.

Atmospheric density is dependent on numerous effects occurring in the upper atmosphere. The region of the Earth's atmosphere from 90 to 500 km (48.6 to 270 nmi) is known as the thermosphere. As gases in the thermosphere are heated by external sources, they expand radially outward which increases the density at higher altitudes. One source of heat is the absorption of solar extreme ultraviolet (EUV) radiation. Since EUV radiation is absorbed by the atmosphere and can not be determined from ground instruments, the 10.7 cm solar radio noise flux, termed $F_{10.7}$, is used to measure solar activity. Although the correlation does not always hold, atmospheric density is assumed to vary directly with the $F_{10.7}$ index[17]. Figure 31-3 shows the estimated solar activity over the next 11 year cycle with a $\pm 2\,\sigma$ variation. The lowest $F_{10.7}$ value predicted for that cycle is 77 while the highest is 245. During average solar activity, $F_{10.7}$ is expected to be 105. The units of solar flux are 10^4 Jansky, where 1 Jansky is 10^{-26} watts m^{-2} Hz^{-1} bandwidth. The region is also subject to heating by the interaction of the Earth's magnetic field with the solar wind (a stream of high speed plasma emanating from the sun) in the region known as the magnetosphere. Energy generated from this interaction, referred to as geomagnetic activity, penetrates into the lower thermosphere and directly heats the local gases. The planetary geomagnetic activity index a_p is used as a measure of geomagnetic activity. It is based on magnetic fluctuation data taken every 3 hours at 12 stations across the globe. The daily planetary geomagnetic index, A_p, is the average of the eight 3-hourly a_p values for that particular day[17]. Figure 31-4 shows the anticipated geomagnetic activity over the next 11 geomagnetic cycle with a $\pm 2\sigma$ variation. The lowest A_p value predicted for that cycle is 7 and the highest is 25. The

average geomagnetic index is predicted to be 12.   Like the $F_{10.7}$ index, atmospheric density varies directly with A_p^{17}.
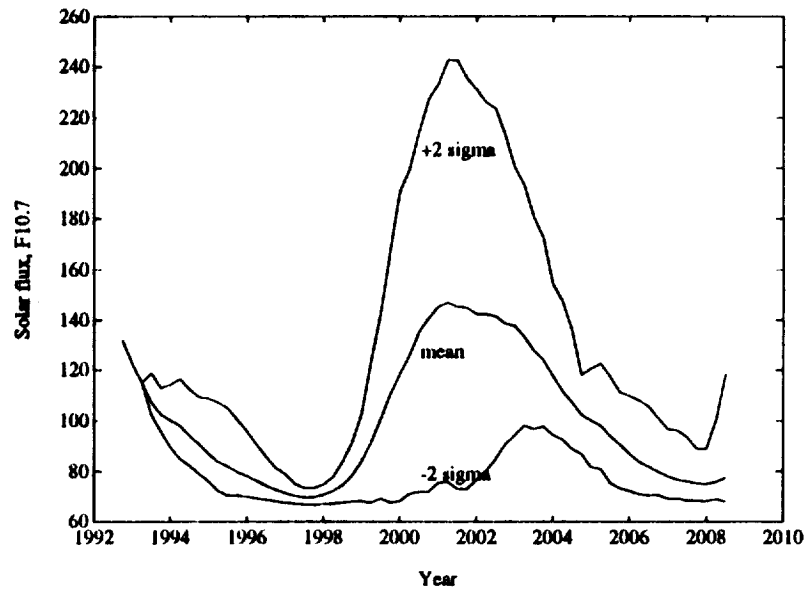
Figure 31-3 Anticipated solar flux over next solar cycle with ± 2σ variation.
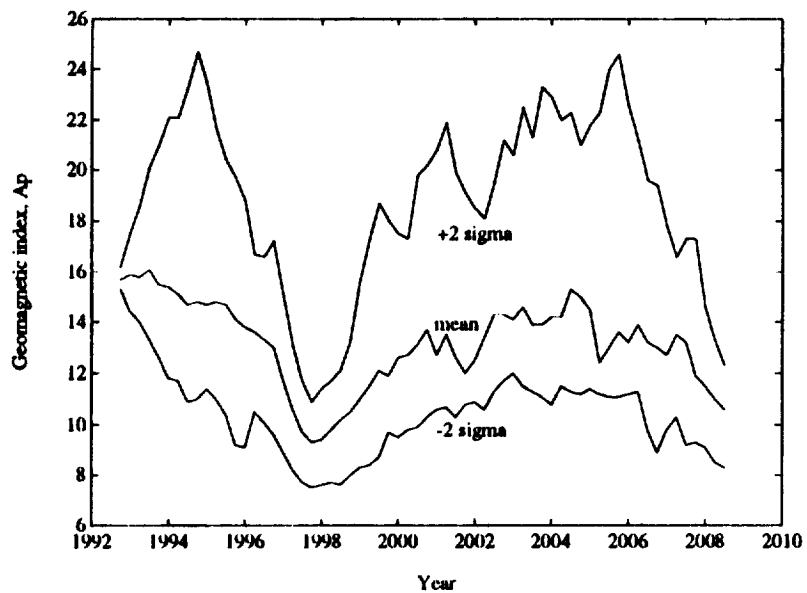
Figure 31-4 Anticipated geomagnetic activity over next cycle with ± 2σ variation.

To model atmospheric properties at orbital altitudes, the Marshall Engineering Thermosphere (MET) was created at the Marshall Spaceflight Center. It is the standard neutral atmospheric density model used for the Space Station program. The MET is capable of accounting for variations in the solar and geomagnetic activity, the diurnal (24 hr period) variation, and the semiannual variation. It is a static diffusion model and is similar to the Smithsonian's Jacchia 1970 model[17]. Figure 31-5 , Figure 31-6 and Figure 31-7 show the density variations from the MET model at 200, 220 and 240 nmi (370, 407 and 444 km, the orbital altitude range described in section 2.1.5) over two orbits for minimum ($F_{10.7}$ = 77, A_p = 7), average ($F_{10.7}$ = 105, A_p = 12) and maximum ($F_{10.7}$ = 245, A_p = 25) solar and geomagnetic activity. The Spring Equinox, 1997 is the date used in the study and the orbital data is the same as that described in section 2.1.
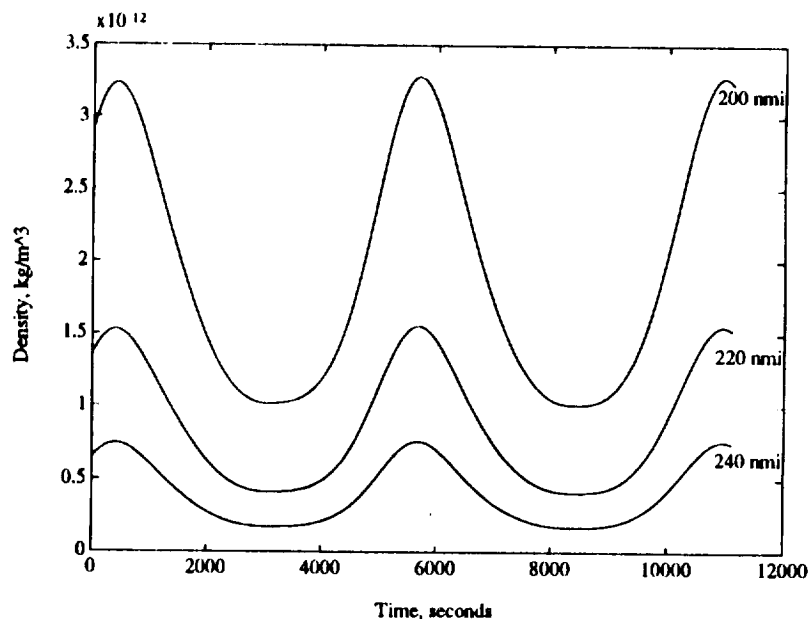
Figure 31-5 Atmospheric density, minimum solar activity.

Using data on SSF from section 2.1 and the above density data, the maximum atmospheric drag force is predicted to be 0.60 N and occurs at 200 nmi (370 km) during maximum solar and
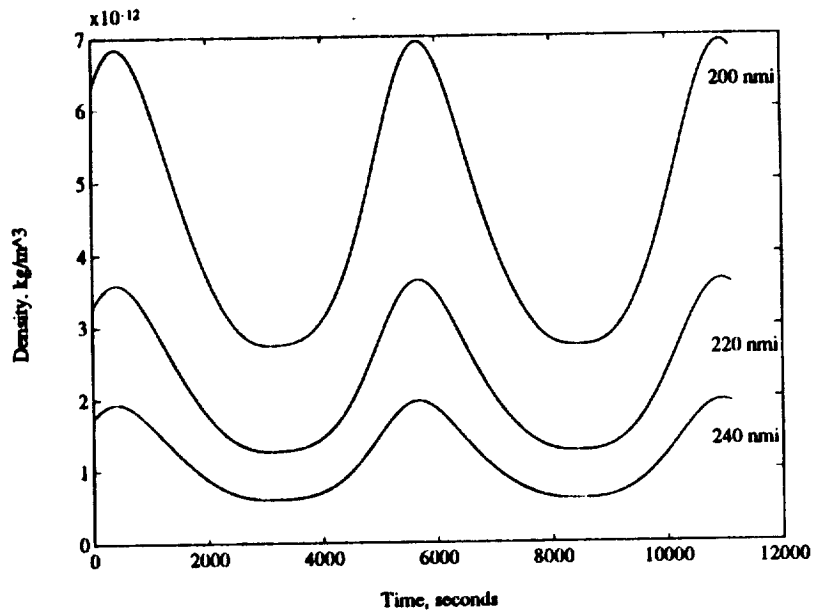
Figure 31-6 Atmospheric density, average solar activity.
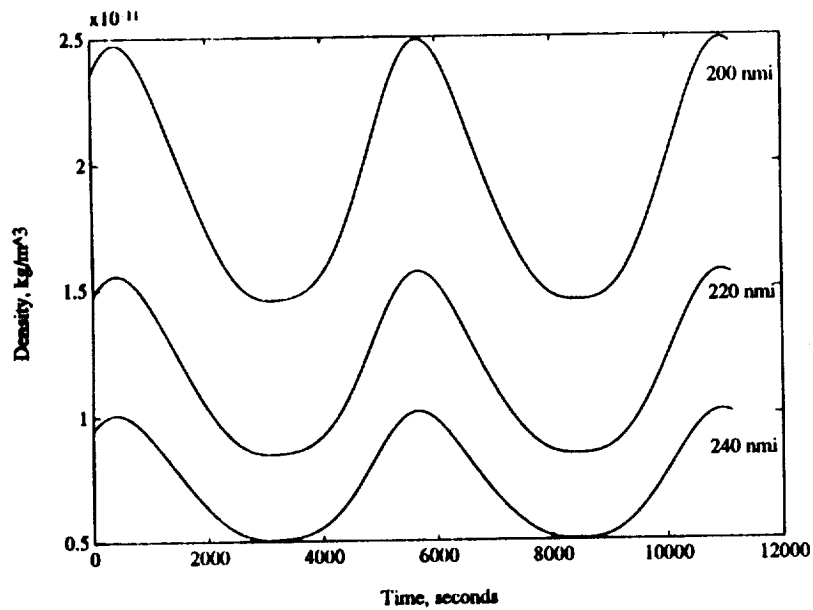
Figure 31-7 Atmospheric density, maximum solar activity.

geomagnetic activity. Similarly, the minimum atmospheric drag force is predicted to be 0.03 N and occurs at 240 nmi (444 km) during times of minimum solar and geomagnetic activity. These forces correspond to an acceleration on SSF of 0.66 μ-g's and 0.033 μ-g's, respectively.

To approximate the drag force in all calculations, a Fourier series representation to model the maximum, average and minimum drag forces was created. This series will provide a standard set of equations with which to calculate the drag force at any point in the orbit. The series has the form

$$F_{drag} = a + b\cos\left(\frac{2\pi}{p}t\right) + c\sin\left(\frac{2\pi}{p}t\right) + d\cos\left(\frac{4\pi}{p}t\right) + e\sin\left(\frac{4\pi}{p}t\right)$$
$$+ f\cos\left(\frac{6\pi}{p}t\right) + g\sin\left(\frac{6\pi}{p}t\right) + h\cos\left(\frac{8\pi}{p}t\right) + i\sin\left(\frac{8\pi}{p}t\right)$$

(31-7)

where for maximum drag force (200 nmi, maximum solar activity) the coefficients are

$$a = -9.6501 \times 10^{-01} \quad b = -2.1288 \times 10^{-01} \quad c = -1.5169 \times 10^{-01}$$
$$d = -2.4887 \times 10^{-02} \quad e = -3.5237 \times 10^{-02} \quad f = -6.6593 \times 10^{-03}$$
$$g = -3.7360 \times 10^{-03} \quad h = 1.1225 \times 10^{-03} \quad i = -1.5678 \times 10^{-03}$$

For average drag force (220 nmi, average solar activity) the coefficients are

$$a = -1.1100 \times 10^{-01} \quad b = -4.7675 \times 10^{-02} \quad c = -3.3480 \times 10^{-02}$$
$$d = -6.9723 \times 10^{-03} \quad e = -1.1445 \times 10^{-02} \quad f = -1.4390 \times 10^{-03}$$
$$g = -2.2415 \times 10^{-01} \quad h = 1.8489 \times 10^{-04} \quad i = -6.8767 \times 10^{-04}$$

And for minimum drag force (240 nmi, minimum solar activity) the coefficients are

$$a = -1.9554 \times 10^{-02} \quad b = -1.1545 \times 10^{-02} \quad c = -8.0131 \times 10^{-03}$$
$$d = -1.9573 \times 10^{-03} \quad e = -3.4337 \times 10^{-03} \quad f = -3.2916 \times 10^{-04}$$
$$g = -8.5503 \times 10^{-04} \quad h = 4.8282 \times 10^{-05} \quad i = -2.5162 \times 10^{-04}$$

p is approximately the orbital period. In all three cases, the Fourier approximation fit the drag curve to within 2% over two orbits.

3.1.4 Radiation Pressure

One of the properties of electromagnetic waves is that they carry momentum and therefore exert pressure on a surface[18]. In orbit, electromagnetic waves from the Sun and Earth impact SSF and act to change the orbit. This is known as radiation pressure and results from direct solar radiation, Earth albedo and Earth emitted radiation. Solar radiation pressure is modeled by[19]

$$P_{solar} = \frac{F}{A} = (1+\beta)\frac{S}{c} \qquad (31\text{-}8)$$

where A is the surface area normal to the direction of radiation, S is the solar constant defined as the amount of radiant energy intercepted by a normal unit area per unit time and is 1.395 kw/m^2 and c is the speed of light, 3×10^8 m/sec. β is the reflectivity of the surface and varies from a minimum of 0 for a surface that's absorbs completely to 1 for perfect reflection[19]. Using the values for S and c, Eq. (31-8) reduces to

$$P_{solar} = \frac{F}{A} = \frac{m\,a}{A} = 4.65 \times 10^{-6}(1+\beta)\ \frac{N}{m^2} \qquad (31\text{-}9)$$

where m is 91880 kg and A and β are taken as worst case values of 927 m^2 and 1, respectively. The maximum acceleration the solar pressure can apply is then 9.38×10^{-8} m/s^2 or 9.56×10^{-9} g's. This value is comparable to the resolution of the OARE accelerometer and is below the required acceleration level targeted for the MESYS. Therefore, solar radiation pressure will be assumed small and ignored in all simulations in this study. However, MESYS would compensate for solar pressure if it were observable.

Earth albedo radiation, which acts primarily in the radial direction, can be modeled under the simplest situations as[19]

$$p_{Earth} = \frac{F}{A} = \frac{1}{4}(1+\beta)\frac{S}{c}\alpha(\frac{R_e}{R})^2$$
$$= \frac{1}{4}\alpha(\frac{R_e}{R})^2 p_{solar}$$

(31-10)

where R_e is the radius of the Earth and R is the radial distance of the orbit. α is albedo, which is defined as the ratio of total reflected light to total incident light. For the Earth, α is approximately 0.37 (Ref. 20). At SSF's orbit of 220 nmi (407 km) altitude, Eq. (31-10) then reduces to $0.082 p_{solar}$. Using the same argument as above, p_{Earth} is also assumed to be small and ignored.

Earth emitted radiation is modeled exactly as direct solar radiation with the solar constant S is replaced with the proper value for the Earth. This value can be determined using Stefan's law which states that radiant intensity of a black body varies with the fourth power of the temperature, or

$$R = \sigma T^4$$

where σ is the Stefan-Boltzmann constant equal to 5.6703×10^{-8} w m^{-2} K^{-4}. Since the Earth has a black body temperature of approximately 300 K, R has a value of 460 w/m^2. Substituting this value for S into Eq. (31-8) yields an acceleration of 3.15×10^{-9} g's and will therefore be assumed small and ignored.

3.2 EQUATIONS OF MOTION

In order to design a linear control system, the equations of motion must first be derived and then linearized. All equations are referenced to the coordinate systems described in section 3.1.1.

3.2.1 Non-Linear Equations Of Motion

The rectilinear motion of an object (such as the proof mass) relative to the station center of mass are[21]

$$\ddot{R} = \ddot{R}_{cm} + \ddot{\rho} + 2(\omega \times \rho) + \dot{\omega} \times \rho + \omega \times (\omega \times \rho) \qquad (32\text{-}1)$$

where

$\ddot{R} = -\mu \dfrac{R}{|R|^3}$ = acceleration of proof mass in Earth fixed coordinate system.

$\ddot{R}_{cm} = -\mu \dfrac{R_{cm}}{|R_{cm}|^3} - \dfrac{F}{m}$ = acceleration of SSF center of mass in Earth fixed coordinate system.

$R = R_{cm} + \rho$ = position of proof mass in Earth fixed coordinate system.

$\rho = [\xi \ \eta \ \zeta]$ = acceleration of proof mass relative to SSF center of mass in orbital coordinate system.

$\omega = \omega_{body} + \omega_{orbit}$ = total angular velocity of SSF.

$$\omega_{orbit} = \left[0 \quad -\sqrt{\frac{\mu}{|R_{cm}|^3}} \quad 0 \right] = \text{orbital angular velocity of SSF.}$$

$$= [0 \quad -\Omega \quad 0]$$

Solving Eq. (32-1) for the relative acceleration gives

$$\ddot{\rho} = \mu \left(\frac{R_{cm}}{|R_{cm}|^3} - \frac{R}{|R|^3} \right) - 2(\omega \times \rho) - (\dot{\omega} \times \rho) - \omega \times (\omega \times \rho) + \frac{F}{m} \qquad (32\text{-}2)$$

Eq. (32-2) can be expressed in the body fixed coordinate system by substituting the following relations

$$\rho = \begin{bmatrix} \xi \\ \eta \\ \zeta \end{bmatrix} = L^T \begin{bmatrix} x \\ y \\ x \end{bmatrix} \qquad \dot{\rho} = \begin{bmatrix} \xi \\ \eta \\ \zeta \end{bmatrix} = L^T \begin{bmatrix} \dot{x} \\ \dot{y} \\ \dot{z} \end{bmatrix} \qquad \ddot{\rho} = \begin{bmatrix} \xi \\ \eta \\ \zeta \end{bmatrix} = L^T \begin{bmatrix} \ddot{x} \\ \ddot{y} \\ \ddot{z} \end{bmatrix} \qquad (32\text{-}3)$$

and

$$\omega_{orbit} = L \begin{bmatrix} 0 \\ -\Omega \\ 0 \end{bmatrix} \qquad (32\text{-}4)$$

The rotation equations of motion can be derived from two sets of equations: first the dynamic relation[15]

3-13

$$\omega_{body} = I^{-1}(N - \omega \times I\omega_{body}) \qquad (32\text{-}5)$$

and second, the kinematic equations relating ω_{body} and θ for a 3-2-1 rotation

$$\dot{\theta}_x = \omega_{body\ x} + \dot{\theta}_z \sin\theta_y$$

$$\dot{\theta}_y = \omega_{body\ y}\cos\theta_x - \omega_{body\ z}\sin\theta_x \qquad (32\text{-}6)$$

$$\dot{\theta}_z = \frac{\omega_{body\ y}\sin\theta_x + \omega_{body\ z}\cos\theta_x}{\cos\theta_y}$$

3.2.2 Linear Equations Of Motion

The equations of motion are linearized about the point $x_0 + x$, $y_0 + y$ and $z_0 + z$ and the rotation angles $\theta_{x0} + \theta_x$, $\theta_{y0} + \theta_y$ and $\theta_{z0} + \theta_z$. Note that x_0, y_0 and z_0 is the location of the point were the microgravity ellipse is to be centered, x, y and z are small deviations from this point, θ_{x0}, θ_{y0} and θ_{z0} is the rotation from orbit to body coordinate systems and θ_x, θ_y and θ_z are small angle deviations about the body coordinate system. Linearizing such complex equations as those here is easiest done in steps. First, sine and cosine relations are linearized as follows:

$$\sin(\theta_{x0} + \theta_x) = \sin\theta_{x0}\cos\theta_x + \cos\theta_{x0}\sin\theta_x$$
$$\approx \sin\theta_{x0} + \theta_x\cos\theta_{x0} \qquad (32\text{-}7)$$

and

$$\cos(\theta_{x0} + \theta_x) = \cos\theta_{x0}\cos\theta_x - \sin\theta_{x0}\sin\theta_x$$
$$\approx \cos\theta_{x0} - \theta_x\sin\theta_{x0} \qquad (32\text{-}8)$$

Angles about y and z linearize similarly to become

$$\sin(\theta_{y0} + \theta_y) \approx \sin\theta_{y0} + \theta_y\cos\theta_{y0} \qquad \cos(\theta_{y0} + \theta_y) \approx \cos\theta_{y0} - \theta_y\sin\theta_{y0}$$

$$\sin(\theta_{z0} + \theta_z) \approx \sin\theta_{z0} + \theta_z\cos\theta_{z0} \qquad \cos(\theta_{z0} + \theta_z) \approx \cos\theta_{z0} - \theta_z\sin\theta_{z0}$$

$$(32-9)$$

These relations are then substituted into Eq. (31-1) from section 3.1 to give the linearized rotation matrix between the body reference system and the orbital reference system and are seen in Eq. (32-10) shown on page 3-16.

The next step is to linearize Eq. (32-6). The equations can be solved in terms of ω_{body} to give

$$\omega_{body\ x} = \theta_x - \theta_z\sin\theta_y$$

$$\omega_{body\ y} = \theta_y\cos\theta_x + \theta_z\cos\theta_y\sin\theta_x \qquad (32-11)$$

$$\omega_{body\ z} = -\theta_y\sin\theta_x + \theta_z\cos\theta_y\cos\theta_x$$

Eq. (32-11) can then be linearized to give

$$\omega_{body\ x} = \theta_x - \theta_z\sin\theta_{y0}$$

$$\omega_{body\ y} = \theta_y\cos\theta_{x0} + \theta_z\cos\theta_{y0}\sin\theta_{x0} \qquad (32-12)$$

$$\omega_{body\ z} = -\theta_y\sin\theta_{x0} + \theta_z\cos\theta_{y0}\cos\theta_{x0}$$

Note that all terms with both θ and $\dot\theta$ are ignored since both are considered small and their product is a higher ordered term.

$$L_{11} = \cos\theta_{z0}\cos\theta_{y0} - \theta_z\sin\theta_{z0}\cos\theta_{y0} - \theta_y\cos\theta_{z0}\sin\theta_{y0}$$

$$L_{12} = \sin\theta_{z0}\cos\theta_{y0} + \theta_z\cos\theta_{z0}\cos\theta_{y0} - \theta_y\sin\theta_{z0}\sin\theta_{y0}$$

$$L_{13} = -\sin\theta_{y0} - \theta_y\cos\theta_{y0}$$

$$L_{21} = \cos\theta_{z0}\sin\theta_{y0}\sin\theta_{x0} - \sin\theta_{z0}\cos\theta_{x0} - \theta_z\sin\theta_{z0}\sin\theta_{y0}\sin\theta_{x0} +$$
$$\theta_y\cos\theta_{z0}\cos\theta_{y0}\sin\theta_{x0} + \theta_x\cos\theta_{z0}\sin\theta_{y0}\cos\theta_{x0} -$$
$$\theta_z\cos\theta_{z0}\cos\theta_{x0} + \theta_x\sin\theta_{z0}\sin\theta_{x0}$$

$$L_{22} = \sin\theta_{z0}\sin\theta_{y0}\sin\theta_{x0} + \cos\theta_{z0}\cos\theta_{x0} + \theta_z\cos\theta_{z0}\sin\theta_{y0}\sin\theta_{x0} +$$
$$\theta_y\sin\theta_{z0}\cos\theta_{y0}\sin\theta_{x0} + \theta_x\sin\theta_{z0}\sin\theta_{y0}\cos\theta_{x0} -$$
$$\theta_z\sin\theta_{z0}\cos\theta_{x0} - \theta_x\cos\theta_{z0}\sin\theta_{x0} \qquad \text{(32-10)}$$

$$L_{23} = \cos\theta_{y0}\sin\theta_{x0} - \theta_y\sin\theta_{y0}\sin\theta_{x0} + \theta_x\cos\theta_{y0}\cos\theta_{x0}$$

$$L_{31} = \cos\theta_{z0}\sin\theta_{y0}\cos\theta_{x0} + \sin\theta_{z0}\sin\theta_{x0} - \theta_z\sin\theta_{z0}\sin\theta_{y0}\cos\theta_{x0} +$$
$$\theta_y\cos\theta_{z0}\cos\theta_{y0}\cos\theta_{x0} - \theta_x\cos\theta_{z0}\sin\theta_{y0}\sin\theta_{x0} +$$
$$\theta_z\cos\theta_{z0}\sin\theta_{x0} + \theta_x\sin\theta_{z0}\cos\theta_{x0}$$

$$L_{32} = \sin\theta_{z0}\sin\theta_{y0}\cos\theta_{x0} - \cos\theta_{z0}\sin\theta_{x0} + \theta_z\cos\theta_{z0}\sin\theta_{y0}\cos\theta_{x0} +$$
$$\theta_y\sin\theta_{z0}\cos\theta_{y0}\cos\theta_{x0} - \theta_x\sin\theta_{z0}\sin\theta_{y0}\sin\theta_{x0} +$$
$$\theta_z\sin\theta_{z0}\sin\theta_{x0} - \theta_x\cos\theta_{z0}\cos\theta_{x0}$$

$$L_{33} = \cos\theta_{y0}\cos\theta_{x0} - \theta_y\sin\theta_{y0}\cos\theta_{x0} - \theta_x\cos\theta_{y0}\sin\theta_{x0}$$

And similarly, the linearized relations between the ω's and θ's are given as

$$\omega_{body\,x} = \dot\theta_x - \dot\theta_z\sin\theta_{y0}$$

$$\omega_{body\,y} = \dot\theta_y\cos\theta_{x0} + \dot\theta_z\cos\theta_{y0}\sin\theta_{x0} \qquad \text{(32-13)}$$

$$\omega_{body\,z} = -\dot\theta_y\sin\theta_{x0} + \dot\theta_z\cos\theta_{y0}\cos\theta_{x0}$$

Equation (32-3) is linearized in the body fixed coordinate system to become

$$\rho = L \begin{bmatrix} x_0 + x \\ y_0 + y \\ z_0 + z \end{bmatrix} \qquad \dot{\rho} = L \begin{bmatrix} \dot{x} \\ \dot{y} \\ \dot{z} \end{bmatrix} \qquad \ddot{\rho} = L \begin{bmatrix} \ddot{x} \\ \ddot{y} \\ \ddot{z} \end{bmatrix} \tag{32-14}$$

The linearized equations of translational motion can then be derived by substituting Eqs. (32-10), (32-12), (32-13) and (32-14) into Eqs. (32-2), (32-3) and (32-4). The results are Eqs. (32-15), (32-16) and (32-17)

$$\ddot{x} = -\frac{\mu}{R_{cm}^3}\{[y_0(c\theta_{z0}s\theta_{y0}c\theta_{x0}+s\theta_{z0}s\theta_{x0})+z_0(s\theta_{z0}c\theta_{x0}-c\theta_{z0}s\theta_{y0}s\theta_{x0})]\theta_x +$$

$$[-x_0s\theta_{y0}c\theta_{x0}+y_0c\theta_{z0}c\theta_{y0}s\theta_{x0}+z_0c\theta_{z0}c\theta_{y0}c\theta_{x0}]\theta_y +$$

$$[-x_0c\theta_{y0}s\theta_z-y_0(s\theta_{z0}s\theta_{y0}s\theta_{x0}+c\theta_{z0}c\theta_{x0})+z_0(c\theta_{z0}s\theta_{x0}-s\theta_{z0}s\theta_{y0}c\theta_{x0})]\theta_z\} +$$

$$(\omega_{orbit\,y}^2+\omega_{orbit\,z}^2-\frac{\mu}{R_{cm}^3}L_{11})x - (\omega_{orbit\,x}\omega_{orbit\,y}+\frac{\mu}{R_{cm}^3}L_{12})y - (\omega_{orbit\,x}\omega_{orbit\,z}+\frac{\mu}{R_{cm}^3}L_{13})z -$$

$$(y_0\omega_{orbit\,z}-x_0\omega_{orbit\,y})\theta_x +$$

$$[2x_0(c\theta_{x0}\omega_{orbit\,y}-s\theta_{x0}\omega_{orbit\,z}) + y_0(s\theta_{x0}\omega_{orbit\,x}-c\theta_{x0}\omega_{orbit\,z})]\theta_y + \tag{32-15}$$

$$[x_0(s\theta_{y0}\omega_{orbit\,y}+2c\theta_{y0}s\theta_{x0}\omega_{orbit\,x}-c\theta_{y0}c\theta_{x0}\omega_{orbit\,z}) +$$

$$2y_0(s\theta_{y0}\omega_{orbit\,z}-c\theta_{y0}c\theta_{x0}\omega_{orbit\,x}-c\theta_{y0}s\theta_{x0}\omega_{orbit\,x})]\theta_z +$$

$$2\omega_{orbit\,z}\dot{y} - 2\omega_{orbit\,y}\dot{z} - z_0\ddot{\theta}_y + y_0\ddot{\theta}_z - \mu(\frac{R_x}{R^3} - \frac{R_{cm\,x}}{R_{cm}^3}) +$$

$$(\omega_{orbit\,y}^2+\omega_{orbit\,z}^2)x_0 - \omega_{orbit\,x}\omega_{orbit\,y}y_0 - \omega_{orbit\,x}\omega_{orbit\,z}z_0 + \frac{F_x}{m}$$

3-17

$$\ddot{y} = -\frac{\mu}{R_{cm}^3}\{[y_0(s\theta_{z0}s\theta_{y0}c\theta_{x0}-c\theta_{z0}s\theta_{x0}) - z_0(s\theta_{z0}s\theta_{y0}s\theta_{x0}+c\theta_{z0}c\theta_{x0})]\theta_x +$$

$$[-x_0s\theta_{z0}s\theta_{y0}+y_0s\theta_{z0}c\theta_{y0}s\theta_{x0}+z_0s\theta_{z0}c\theta_{y0}c\theta_{x0}]\theta_y +$$

$$[x_0c\theta_{z0}c\theta_{y0}+y_0(c\theta_{z0}s\theta_{y0}s\theta_{x0}-s\theta_{z0}c\theta_{x0}) + z_0(s\theta_{z0}s\theta_{x0}+c\theta_{z0}s\theta_{y0}c\theta_{x0})]\theta_z) -$$

$$(\omega_{orbit\ y}\omega_{orbit\ x}+\frac{\mu}{R_{cm}^3}L_{21})x + (\omega_{orbit\ x}^2 + \omega_{orbit\ z}^2-\frac{\mu}{R_{cm}^3}L_{22})y - (\omega_{orbit\ y}\omega_{orbit\ z}+\frac{\mu}{R_{cm}^3}L_{23})z +$$

$$(2y_0\omega_{orbit\ x} - x_0\omega_{orbit\ y})\theta_x + \tag{32-16}$$

$$[-x_0c\theta_{x0}\omega_{orbit\ x} + 2y_0c\theta_{x0}\omega_{orbit\ z} + z_0(s\theta_{x0}\omega_{orbit\ y}-c\theta_{x0}\omega_{orbit\ z})]\theta_y +$$

$$[x_0(s\theta_{y0}\omega_{orbit\ z}-c\theta_{y0}s\theta_{x0}\omega_{orbit\ x} + 2y_0(c\theta_{y0}c\theta_{x0}\omega_{orbit\ z}-s\theta_{y0}\omega_{orbit\ x}) -$$

$$z_0(c\theta_{y0}s\theta_{x0}\omega_{orbit\ x}-c\theta_{y0}s\theta_{x0}\omega_{orbit\ y}]\theta_z$$

$$\omega_{orbit\ z}\dot{x} + 2\omega_{orbit\ x}\dot{z} + z_0\dot{\theta}_x + x_0\dot{\theta}_z - \mu(\frac{R_y}{R^3} - \frac{R_{cm\ y}}{R_{cm}^3}) -$$

$$\omega_{orbit\ y}\omega_{orbit\ x}x_0 + (\omega_{orbit\ x}^2+\omega_{orbit\ z}^2)y_0 - \omega_{orbit\ y}\omega_{orbit\ z}z_0 + \frac{F_y}{m}$$

$$\ddot{z} = -\frac{\mu}{R_{cm}^3}\{[y_0 c\theta_{y0} c\theta_{x0} - z_0 c\theta_{y0} s\theta_{x0}]\theta_x - [x_0 c\theta_{y0} - y_0 s\theta_{y0} s\theta_{x0} - z_0 c\theta_{y0} c\theta_{x0}]\theta_y\} -$$

$$(\omega_{orbit\,z}\omega_{orbit\,x}+\frac{2\mu}{R_{cm}^3}L_{31})x - (\omega_{orbit\,z}\omega_{orbit\,y}+\frac{2\mu}{R_{cm}^3}L_{32})y + (\omega_{orbit\,x}^2+\omega_{orbit\,y}^2+\frac{2\mu}{R_{cm}^3}L_{33})z +$$

$$(2z_0\omega_{orbit\,x} - x_0\omega_{orbit\,z})\dot{\theta}_x +$$

$$[x_0 s\theta_{x0}\omega_{o.bit\,x} + y_0(s\theta_{x0}\omega_{orbit\,y}-c\theta_{y0}\omega_{orbit\,z}) + z_0 c\theta_{x0}\omega_{orbit\,y}]\dot{\theta}_y -$$

$$[x_0(s\theta_{x0}\omega_{orbit\,z}-c\theta_{x0} c\theta_{y0}\omega_{orbit\,x} - y_0(c\theta_{y0} s\theta_{x0}\omega_{orbit\,y}+c\theta_{y0} s\theta_{x0}\omega_{orbit\,z}) +$$

$$2z_0(c\theta_{y0} s\theta_{x0}\omega_{orbit\,y}-s\theta_{y0}\omega_{orbit\,z})]\dot{\theta}_3 + \qquad (32\text{-}17)$$

$$2\omega_{orbit\,y}\dot{x} - 2\omega_{orbit\,x}\dot{y} - y_0\ddot{\theta}_x + x_0\ddot{\theta}_y - \mu(\frac{R_z}{R^3} - \frac{R_{cm\,z}}{R_{cm}^3}) -$$

$$\omega_{orbit\,z}\omega_{orbit\,x}x_0 - \omega_{orbit\,z}\omega_{orbit\,y}y_0 + (\omega_{orbit\,x}^2+\omega_{orbit\,y}^2)z_0 + \frac{F_z}{m}$$

The equations of rotational motion are linearized by first linearizing the equations for gravity gradient torques by substituting Eq. (32-10) into Eq. (31-2). The results are shown in eqtns (32-18),

$$N_{gg\,x} = \frac{3\mu}{R_{cm}^3}\{[(I_{yy}-I_{zz})(L_{33}(-c\theta_{x0} c\theta_{x0}-s\theta_{x0} s\theta_{y0} s\theta_{x0})) + I_{xy}(L_{33}(-c\theta_{x0} s\theta_{y0} s\theta_{x0}+s\theta_{x0} c\theta_{x0})$$

$$-L_{31}c\theta_{y0} s\theta_{10})) - I_{13}(L_{32}(s\theta_{y0} c\theta_{x0}-c\theta_{x0} s\theta_{y0} s\theta_{x0})-L_{31}(c\theta_{x0} c\theta_{x0}-s\theta_{x0} s\theta_{y0} s\theta_{x0})) +$$

$$I_{yz}(-2L_{33}c\theta_{y0} s\theta_{x0}+2L_{32}(c\theta_{x0} c\theta_{x0}-s\theta_{x0} s\theta_{y0} s\theta_{x0}))]\theta_x +$$

$$[(I_{yy}-I_{zz})(-L_{32}s\theta_{y0} c\theta_{x0}+L_{33}s\theta_{x0} c\theta_{y0} c\theta_{x0}) + I_{xy}(-L_{31}s\theta_{y0} c\theta_{x0}+L_{33}c\theta_{x0} c\theta_{y0} c\theta_{x0}) -$$

$$I_{xz}(L_{31}s\theta_{x0} c\theta_{y0} c\theta_{x0}+L_{32}c\theta_{x0} c\theta_{y0} c\theta_{x0}) - 2I_{yz}(L_{33}s\theta_{y0} c\theta_{x0}-L_{32}s\theta_{x0} c\theta_{y0} c\theta_{x0})]\theta_y + \qquad (32\text{-}18)$$

$$[(I_{yy}-I_{zz})(L_{33}(c\theta_{x0} s\theta_{y0} c\theta_{x0}+s\theta_{x0} s\theta_{x0}) + I_{xy}(L_{33}(c\theta_{x0} s\theta_{x0}-s\theta_{x0} s\theta_{y0} c\theta_{x0}) -$$

$$I_{xz}(L_{31}(c\theta_{x0} s\theta_{y0} c\theta_{x0}+s\theta_{x0} s\theta_{x0})+L_{32}(c\theta_{x0} s\theta_{x0}-s\theta_{x0} s\theta_{y0} c\theta_{x0})) -$$

$$I_{yz}L_{32}(c\theta)z0s\theta_{y0} c\theta_{x0}-s\theta_{x0} s\theta_{x0})]\theta_z +$$

$$L_{32}L_{33}(I_{yy}-I_{zz}) + L_{31}L_{33}I_{xy} - L_{31}L_{32}I_{xz} + (L_{33}^2-L_{32}^2)I_{yz}\}$$

(32-19) and (32-20).

3-19

$$N_{gg\,y} = \frac{3\mu}{R_{cm}^3} \{[(I_{zz}-I_{xx})(L_{33}(s\theta_{z0}c\theta_{x0}-c\theta_{z0}s\theta_{y0}s\theta_{x0})-L_{31}c\theta_{y0}s\theta_{x0})) +$$

$$I_{yz}(L_{32}(-c\theta_{z0}s\theta_{y0}s\theta_{x0}+s\theta_{z0}c\theta_{x0})-L_{31}(c\theta_{z0}c\theta_{x0}-s\theta_{z0}s\theta_{y0}s\theta_{x0})) +$$

$$I_{xy}(L_{33}(c\theta_{z0}c\theta_{x0}-s\theta_{z0}s\theta_{y0}s\theta_{x0})-L_{32}(c\theta_{y0}s\theta_{x0})) +$$

$$I_{xz}(2L_{31}(s\theta_{z0}c\theta_{x0}-c\theta_{z0}s\theta_{y0}s\theta_{x0})-2L_{33}(-c\theta_{y0}s\theta_{x0}))]\theta_x +$$

$$[(I_{zz}-I_{xx})(-L_{31}s\theta_{y0}c\theta_{x0}+L_{33}c\theta_{z0}c\theta_{y0}c\theta_{x0}) + I_{yz}(L_{31}s\theta_{z0}c\theta_{y0}c\theta_{x0}+L_{32}c\theta_{z0}c\theta_{y0}c\theta_{x0}) -$$

$$\text{(32-19)}$$

$$I_{xy}(-L_{33}s\theta_{y0}c\theta_{x0}+L_{33}s\theta_{z0}c\theta_{y0}c\theta_{x0}) + 2I_{yz}(L_{31}c\theta_{z0}c\theta_{y0}c\theta_{x0}+L_{33}s\theta_{z0}c\theta_{x0})]\theta_y +$$

$$[(I_{zz}-I_{xx})(L_{33}(c\theta_{z0}s\theta_{x0}-s\theta_{z0}s\theta_{y0}c\theta_{x0})) +$$

$$I_{yz}(L_{31}(c\theta_{z0}s\theta_{y0}c\theta_{x0}-s\theta_{z0}s\theta_{x0})+L_{32}(c\theta_{z0}s\theta_{x0}-s\theta_{z0}s\theta_{y0}c\theta_{x0})) -$$

$$I_{xy}(L_{33}(c\theta_{z0}s\theta_{y0}c\theta_{x0}+s\theta_{z0}s\theta_{x0}) + 2I_{xz}L_{31}(c\theta_{z0}s\theta_{x0}-s\theta_{z0}s\theta_{y0}c\theta_{x0}))]\theta_z +$$

$$L_{31}L_{33}(I_{zz}-I_{xx}) + L_{31}L_{32}I_{yz} - L_{32}L_{33}I_{xy} + (L_{31}^2-L_{33}^2)I_{xz}\}$$

$$N_{gg\,z} = \frac{3\mu}{R_{cm}^3} \{[(I_{xx}-I_{yy})(L_{32}(s\theta_{z0}c\theta_{x0}-c\theta_{z0}s\theta_{y0}s\theta_{x0})-L_{31}(s\theta_{z0}s\theta_{y0}s\theta_{x0}+c\theta_{z0}c\theta_{x0})) -$$

$$I_{xz}(L_{33}(c\theta_{z0}c\theta_{x0}+s\theta_{z0}s\theta_{y0}s\theta_{x0})+L_{32}(c\theta_{z0}s\theta_{x0})) +$$

$$I_{yz}(L_{33}(s\theta_{z0}c\theta_{x0}-c\theta_{z0}s\theta_{y0}s\theta_{x0})-L_{31}c\theta_{y0}s\theta_{x0}) +$$

$$2I_{xy}(-L_{33}(c\theta_{z0}c\theta_{x0}+s\theta_{z0}s\theta_{y0}s\theta_{x0})-L_{31}(s\theta_{z0}c\theta_{x0}-c\theta_{z0}s\theta_{y0}s\theta_{x0}))]\theta_x +$$

$$[(I_{xx}-I_{yy})(L_{31}s\theta_{z0}c\theta_{y0}c\theta_{x0}+L_{32}c\theta_{z0}c\theta_{y0}c\theta_{x0}) + I_{xz}(-L_{32}s\theta_{y0}c\theta_{x0}+L_{33}s\theta_{z0}c\theta_{y0}c\theta_{x0}) -$$

$$\text{(32-20)}$$

$$I_{yz}(-L_{31}s\theta_{y0}c\theta_{x0}+L_{33}c\theta_{z0}c\theta_{y0}c\theta_{x0}) + 2I_{xy}(L_{32}s\theta_{z0}c\theta_{y0}c\theta_{x0}-L_{31}c\theta_{z0}c\theta_{y0}c\theta_{x0}))]\theta_y +$$

$$[(I_{xx}-I_{yy})(L_{31}(c\theta_{z0}s\theta_{z0}c\theta_{x0}+s\theta_{z0}s\theta_{x0})+L_{32}(c\theta_{z0}s\theta_{x0}-s\theta_{z0}s\theta_{y0}c\theta_{x0})) +$$

$$I_{xz}(L_{33}(c\theta_{z0}s\theta_{y0}c\theta_{x0}+s\theta_{z0}s\theta_{x0})) + I_{yz}(L_{33}(c\theta_{z0}s\theta_{x0}-s\theta_{z0}s\theta_{y0}c\theta_{x0})) +$$

$$2I_{xy}(L_{33}(c\theta_{z0}s\theta_{y0}c\theta_{x0}+s\theta_{z0}s\theta_{x0})-L_{31}(c\theta_{z0}s\theta_{x0}-s\theta_{z0}s\theta_{y0}c\theta_{x0}))]\theta_z +$$

$$L_{31}L_{32}(I_{xx}-I_{yy}) + L_{32}L_{33}I_{xz} - L_{31}L_{33}I_{yz} + (L_{32}^2-L_{31}^2)I_{xy}\}$$

Note that in Eqs. (32-15) through (32-20), L_{ij} refers Eq. (31-2) evaluated at $|\theta_{x0}\ \theta_{y0}\ \theta_{z0}|$

The term $\omega \times I\omega_{body}$ in Eq. (32-5) can be linearized to become

$$\omega \times I\omega_{body} = \{(\omega_{orbit\,y}I_{zx}+\omega_{orbit\,z}I_{yx})\theta_x +$$

$$[-\omega_{orbit\,y}(I_{zy}c\theta_{x0}-I_{zz}s\theta_{x0})+\omega_{orbit\,z}(I_{yy}c\theta_{x0}-I_{yz}s\theta_{x0})]\theta_y +$$

$$[-\omega_{orbit\,y}(I_{zz}c\theta_{y0}c\theta_{x0}+I_{zy}c\theta_{y0}s\theta_{x0}-I_{zx}s\theta_{y0})+\omega_{orbit\,z}(I_{yz}c\theta_{y0}c\theta_{x0}+I_{yy}c\theta_{y0}s\theta_{x0}-I_{yx}s\theta_{y0})]\theta_z\}\hat{i}$$

$$+ \{(\omega_{orbit\,z}I_{xx}+\omega_{orbit\,z}I_{zx})\theta_x +$$

$$[-\omega_{orbit\,z}(I_{xy}c\theta_{x0}-I_{xy}s\theta_{x0})+\omega_{orbit\,x}(I_{zy}c\theta_{x0}-I_{zz}s\theta_{x0})]\theta_y + \qquad (32\text{-}21)$$

$$[-\omega_{orbit\,z}(I_{xz}c\theta_{y0}c\theta_{x0}+I_{xy}c\theta_{y0}s\theta_{x0}-I_{xx}s\theta_{y0})+\omega_{orbit\,x}(I_{zz}c\theta_{y0}c\theta_{x0}+I_{zy}c\theta_{y0}s\theta_{x0}-I_{zx}s\theta_{y0})]\theta_z\}\hat{j}$$

$$+ \{(\omega_{orbit\,y}I_{yx}+\omega_{orbit\,z}I_{xx})\theta_x +$$

$$[-\omega_{orbit\,x}(I_{yy}c\theta_{x0}-I_{yz}s\theta_{x0})+\omega_{orbit\,y}(I_{xy}c\theta_{x0}-I_{xz}s\theta_{x0})]\theta_y +$$

$$[-\omega_{orbit\,x}(I_{yz}c\theta_{y0}c\theta_{x0}+I_{yy}c\theta_{y0}s\theta_{x0}-I_{yx}s\theta_{y0})+\omega_{orbit\,y}(I_{xz}c\theta_{y0}c\theta_{x0}+I_{xy}c\theta_{y0}s\theta_{x0}-I_{xx}s\theta_{y0})]\theta_z\}\hat{k}$$

The rotational equations of motion are then achieved by substituting Eqs. (32-18) through (32-21) into Eq. (32-5).

3.3 NOMINAL MICROGRAVITY ENVIRONMENT

The equations of motion can be used to examine the nominal gravity gradient contours and the microgravity environment in the laboratory module of SSF. It is necessary to examine the nominal conditions in the laboratory module to properly judge any improvement the MESYS may provide.

3.3.1 Gravity Gradient Contours

Gravity gradient forces arise from the fact that each individual part of a satellite is in a different orbit and therefore feels a different force from gravity. A contour plot of these forces can be created using the following formula in the orbital reference coordinate system

$$\ddot{\rho} = -\mu\left(\frac{R}{|R|^3} - \frac{R_{cm}}{|R_{cm}|^3}\right) - \omega \times (\omega \times \rho) \tag{33-1}$$

where in this case ω is reduced to $[0 \ -\Omega \ 0 \ ]$ since ω_{body} is assumed to be zero along with $\dot{\omega}$ and $\dot{\rho}$. This formula is the exact version of the equations used in section 1.4.

The gravity gradient contours created by Eq. (33-1) are shown in Figure 33-1, Figure 33-2 and Figure 33-3. Figure 33-1 shows the contours in the η-ζ plane. Note that the center of the ellipse is the center of mass of SSF and that the microgravity level in the ζ (radial) direction is 3 time that in the η (across track) direction. Recall in section 1.4, the acceleration in the radial direction was twice the value in the crosstrack direction. The acceleration is higher here because this study has not ignored the rotational terms as was done in section 1.4. Figure 33-2 and Figure 33-3 show the microgravity level in the ξ-ζ plane and the ξ-η plane. Note again that the microgravity level is constant in the ξ (down track) direction and is 3 times as great in the radial direction as it is in the across track direction. The net effect is that a microgravity tube centered on the ξ axis is created. A displacement of 1 unit distance along the ξ direction will feel no net acceleration, to a first order approximation, while a displacement in the η direction will feel 1 unit of acceleration and a displacement in the ζ direction will feel 3 units of acceleration. Therefore, it is best to align the long axis of the laboratory module parallel with the ξ axis so that the experiment racks are aligned with the microgravity tube.
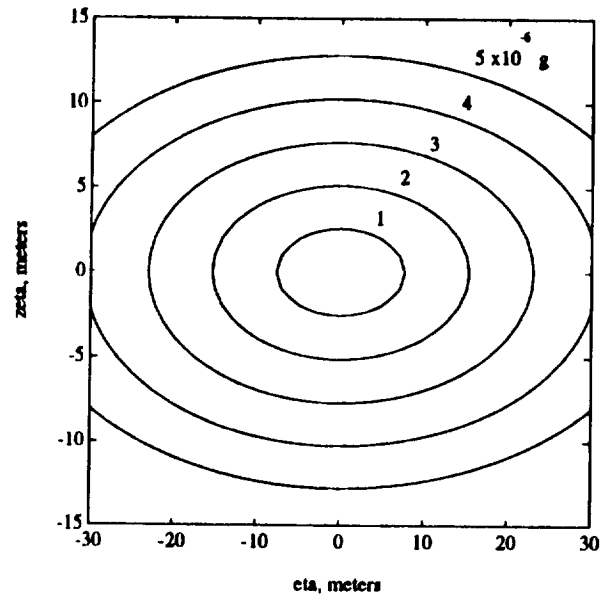
Figure 33-1 Microgravity contours in the η-ζ plane.
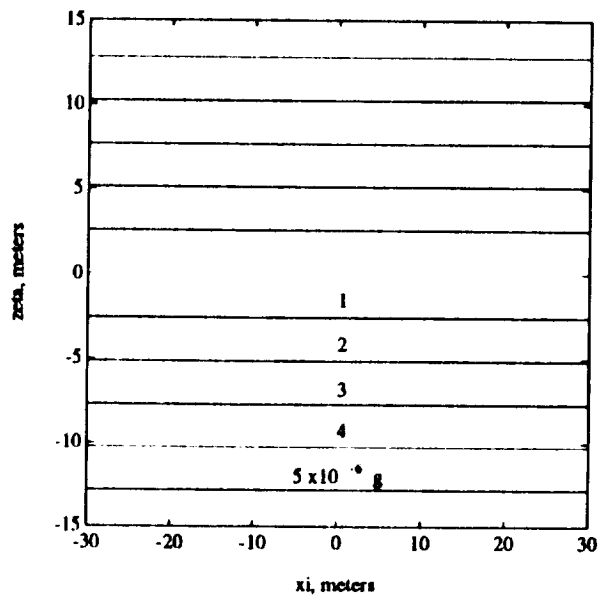
Figure 33-2 Microgravity contours in the ξ-ζ plane.
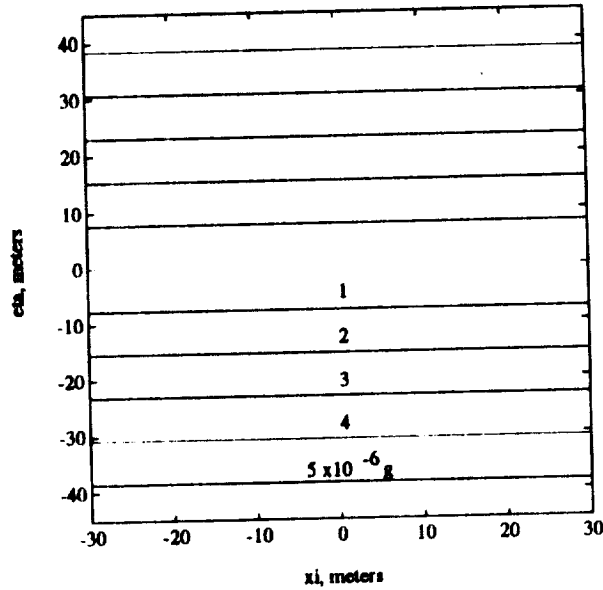
Figure 33-3 Microgravity contours in the ξ-η plane.

3.3.2 Acceleration Level In The Laboratory Module

The standard equations of motion can be used to compute the microgravity level at any point in the laboratory module. Recall from section 3.2 the equations of motion are

$$\ddot{\rho} = -\mu\left(\frac{R}{|R|^3} - \frac{R_{cm}}{|R_{cm}|^3}\right) - 2(\omega \times \dot{\rho}) - \dot{\omega} \times \rho - \omega \times (\omega \times \rho) + \frac{F}{m} \qquad (33\text{-}2)$$

and

$$\dot{\omega}_{body} = I^{-1}(N - \omega \times I\omega_{body}) \qquad (33\text{-}3)$$

The object of this section is to map the microgravity environment in the individual experiment racks contained in the laboratory module. Refer to section 2.1.3 for experiment rack

3-24

locations and nomenclature. For this study, SSF is in the nominal LVLH orientation and it is assumed that $\omega_{body}=$ | 0.002 0.002 0.002 | deg/sec. This is the value generally accepted as the maximum drift rate of SSF[10]. Table 33-1 shows the absolute acceleration level in each experiment rack.

Table 33-1 Microgravity level in each experiment rack, μg.

	Rack 1	Rack 2	Rack 3	Rack 4	Rack 5
Ceiling	1.81	1.81	1.81	1.82	1.82
Starboard	1.95	1.955	1.96	1.96	1.96
Floor	2.56	2.57	2.57	2.57	2.57
Port	2.30	2.30	2.30	2.31	2.31

3.4 STATIC EQUILIBRIUM CASE

As an idealized assessment of the acceleration feedback system, a study was performed to calculate the forces required to keep SSF in static equilibrium with respect to the orbital reference frame. Such a study will provide an estimate of the fuel cost of the MESYS.

3.4.1 Derivation

Static equilibrium is achieved when the applied control forces and torques balance the measured disturbing forces and torques observed in the laboratory module. The acceleration level in the laboratory module is given by Eqs. (32-2) and (32-5) from section 3.2

$$\ddot{\rho} = -\mu(\frac{R}{|R|^3} - \frac{R_{cm}}{|R_{cm}|^3}) - 2(\omega \times \dot{\rho}) - \dot{\omega} \times \rho - \omega \times \omega \times \rho + \frac{F}{m} \qquad (34\text{-}1)$$

$$\dot{\omega}_{body} = I^{-1}(N - \omega \times I\omega_{body}) \qquad (34\text{-}2)$$

and

$$F = F_c + F_a$$

$$N = N_c + N_a + N_{gg}$$

where ω_{body} is determined from the Euler equations for a 3-2-1 rotation, Eq. (32-6) in section 3.2.

To study static equilibrium, it is assumed that the control system will maintain SSF at the commanded attitude. Therefore, the $\dot{\omega}_{body}$, ω_{body}, $\dot{\rho}$ and $\ddot{\rho}$ terms will be zero. Also recall that $\omega = \omega_{body} + L\Omega$ where L is the orbit frame to body frame rotation matrix given in section 3.1.1 and Ω is the orbital angular velocity vector. Eq. (34-1) then reduces to

$$\ddot{\rho} = -\mu(\frac{R}{|R|^3} - \frac{R_{cm}}{|R_{cm}|^3}) - L\Omega \times L\Omega \times \rho + \frac{F}{m} = 0 \qquad (34\text{-}3)$$

The static control force required to null the acceleration in the lab module is then

$$F_c = m\left[\mu(\frac{R}{|R|^3} - \frac{R_{cm}}{|R_{cm}|^3}) + L\Omega \times L\Omega \times \rho\right] - F_a \qquad (34\text{-}4)$$

For SSF to hold a fixed attitude, the control force must also cancel any gravity gradient and aerodynamic torques. Using the same assumptions as above, Eq. (34-2) reduces to

$$N = N_{gg} + N_a + N_c = 0 \qquad (34\text{-}5)$$

In terms of the individual thruster positions and forces, Eqs. (34-4) and (34-5) can be rewritten as

$$\sum_{i=1}^{10} f_i d_i = F_c = m\left[\mu\left(\frac{R}{|R|^3} - \frac{R_{cm}}{|R_{cm}|^3}\right) + L\Omega \times L\Omega \times \rho\right] - F_a \qquad (34\text{-}6)$$

and

$$\sum_{i=1}^{10} r_i \times f_i d_i = N_c = -N_{gg} - N_a \qquad (34\text{-}7)$$

where r_i is the position vector from the center of mass to the i-th thruster, d_i is the unit direction vector of the thrust and f_i is the magnitude of the thruster force. r_i and d_i for the 10 thrusters are given in section 2.3. Eqs. (34-6) and (34-7) can be solved using linear programming techniques to minimize the thruster force. Assuming that fuel flow rate is directly proportional to thruster force, this will also minimize the total fuel required for operation. Linear programming problems are written in the following form[22]: Find the $X \equiv (x_1,...,x_n)$ that minimizes

$$F(X) = \sum_{j=1}^{n} c_j x_j \qquad (34\text{-}8)$$

subject to

$$\sum_{j=1}^{n} a_{ij}x_j = b_i, \qquad i = 1,...,m \qquad\qquad (34\text{-}9)$$

$$x_j \geq 0, \qquad\qquad j = 1,...,n$$

Or in matrix form: Find the **X** that minimizes

$$F(X) = C^T X \qquad\qquad (34\text{-}10)$$

subject to

$$AX = B$$
$$X \geq 0 \qquad\qquad (34\text{-}11)$$

For the case here, the idea is to minimize the sum of all thruster forces f_i (thereby minimizing fuel flow), subject to the constraints of Eqs. (34-6) and (34-7). In the matrix form, $X = F = |f_1,...,f_{10}|^T$,

$$A = \begin{bmatrix} d_1\hat{i} & .... & d_{10}\hat{i} \\ d_1\hat{j} & .... & d_{10}\hat{j} \\ d_1\hat{k} & .... & d_{10}\hat{k} \\ r_1{\times}d_1\hat{i} & .... & r_{10}{\times}d_{10}\hat{i} \\ r_1{\times}d_1\hat{j} & .... & r_{10}{\times}d_{10}\hat{j} \\ r_1{\times}d_1\hat{k} & .... & r_{10}{\times}d_{10}\hat{k} \end{bmatrix} \qquad B = \begin{bmatrix} F_c\hat{i} \\ F_c\hat{j} \\ F_c\hat{k} \\ N_c\hat{i} \\ N_c\hat{j} \\ N_c\hat{k} \end{bmatrix}$$

and **C** is a weighting function for the components of **X**. For this case it is assumed that all values of **F** are weighted equally (i.e. that all thrusters have the same I_{sp}), $C^T = |1\ 1\ 1\ 1\ 1\ 1\ 1\ 1\ 1\ 1|$. Variations among thruster characteristics can be

3-28

accommodated in the C vector to still minimize fuel usage.

3.4.2 Thruster Forces

Using the linear programming techniques described above, it is possible to solve for individual thruster forces to cancel both disturbing forces and torques. This study was performed with SSF in the nominal LVLH orientation to maximize the number of laboratory racks in the microgravity tube (see section 3.3.1) for minimum, average and maximum atmospheric drag forces and torques (see section 3.1.3). Figure 34-1, Figure 34-2 and Figure 34-3 show the individual thruster forces for the range of atmospheric forces. Recall from section 2.3.2 that thrusters 1, 2, 6 and 7 act in the $\pm \xi$ direction, thrusters 3, 4, 8 and 9 act in the $\pm \eta$ direction and thrusters 5 and 10 act in the $\pm \zeta$ direction (in the LVLH orientation, the body and orbital reference coordinate systems are aligned). Notice how thrusters 5 and 10 are constant across an orbit. These thrusters act to translate SSF in the ζ (radial) direction and rotate SSF about the ξ and η axes. Also, either thrusters 3 and 4 or 8 and 9 are not constant over an orbit. These thrusters act to translate SSF in the η (cross track) direction and rotate SSF about the ξ and ζ directions. Since drag torques vary over an orbit and act only about the η and ζ axes, thrusters 1, 2, 6 and 7 must be controlling drag torques about the η direction while thrusters 3, 4, 8 and 9 are controlling drag torques about the ζ direction.

Note that the average atmospheric drag force case uses less total thruster force than the minimum atmospheric drag force case. This is due to the atmospheric torque partially canceling the gravity gradient torques. In the minimum atmospheric drag case, the drag force and resulting torque is not as large and therefore is not as beneficial. The maximum atmospheric drag forces applies too much torque, which must be negated by the thruster and is the most expensive.
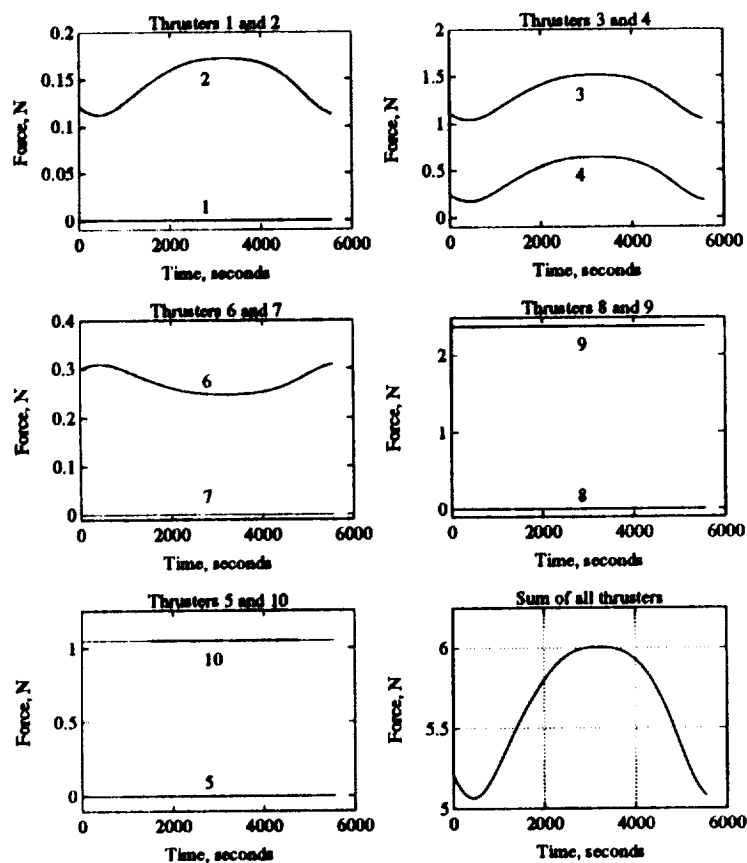
Figure 34-1 Thruster forces for average atmospheric drag.

These conclusions can also be seen when the total thruster force plots are compared with the corresponding atmospheric density plots from section 3.1.3. For the minimum and average atmospheres, the total thruster forces goes to a minimum when the density, and therefore the drag force, goes to a maximum, whereas for the maximum atmosphere, the total thruster force is maximum when the density is maximum and minimum when the density is minimum.

The fuel use for an orbit varies ranges from 10.62 kg for the average atmosphere to 11.89 for the minimum atmosphere to 20.75 kg for the maximum atmosphere.

3.4.3 Conclusions

This section presented the steady state thruster requirements for the MESYS. The study
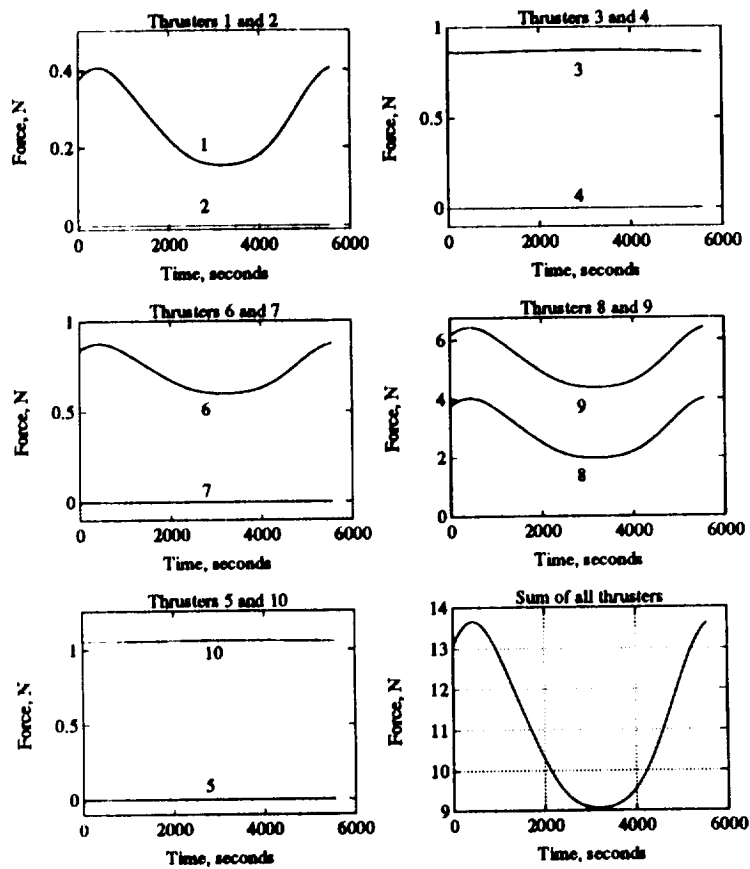
Figure 34-2 Thruster forces for maximum atmospheric drag.

includes assumptions that the body rotations are held to zero and does not include errors such as variations in the center of pressure, motion of the solar power and thermal control system arrays, etc. Therefore it can be expected that the MESYS will require a minimum of 10.62 kg to 20.75 kg per orbit of operation.
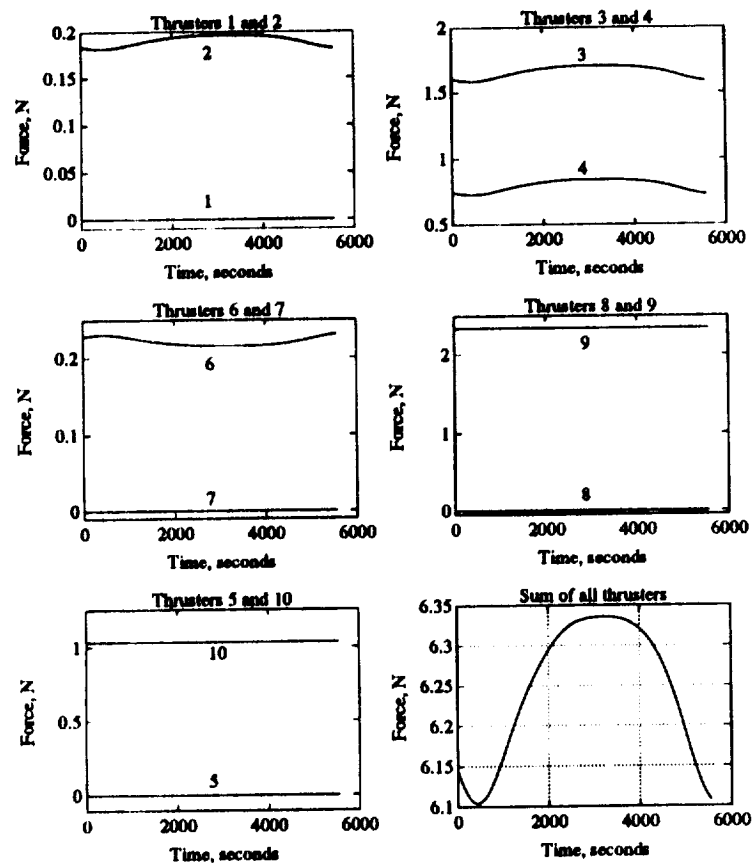
Figure 34-3 Thruster forces for minimum atmospheric drag.

3.5 OARE RESPONSIVENESS TEST

Questions arose during the initial study of the OARE accelerometer as to how closely the accelerometer could follow the variations in the atmospheric drag force. Also of concern was the effect of thruster bias on the control system. Thruster bias is a measurement of the error between the control system commanded force and the actual force that the thruster applies. This study was undertaken in an attempt to answer these questions.

3.5.1 Derivation

As described in section 2.2.1, the OARE accelerometer averages data over the past 50

3-32

seconds to determine the acceleration. The SSF attitude control system, described in section 2.1.8, uses a control force firing period of 33 seconds. To make these two systems compatible, it was decided to change the OARE software so that it would collect data over 66 seconds, or two attitude control system firing periods. It was felt that averaging 33 seconds of OARE data might compromise the accuracy of the measurement since it is less than the 50 second period used in the OARE and shown to be accurate to less than 10^{-8} g's. Therefore the acceleration feedback system version of the MESYS uses the following algorithm:

1) 66 seconds of OARE data (10 data points per second) are averaged and the result is taken as the prediction for the difference in the disturbing force acceleration and the applied control force acceleration for the next 33 second firing period.

2) The thrust level is incremented by the prediction from step 1.

3) Steps 1 and 2 are repeated.

To evaluate this algorithm, the Fourier series representation derived from the Marshall Engineering Thermosphere program (see section 3.1) was used to calculate atmospheric drag 10 times every second over an orbit, the same sample rate as the OARE accelerometer. Since there is no gravity gradient acceleration in the x direction, the atmospheric drag force is the only external disturbance on SSF in that direction. Sixty six seconds of the disturbance force data are averaged to simulate an OARE measurement. Calling this value a_m, at any time τ, the control

3-33

force is given by

$$F_c(\tau) = F_c(\tau - 33) - (F_c(\tau - 33) - m\,a_m)\beta \qquad (35\text{-}1)$$

where β is the system bias. For example, a bias of 1.2 indicates that when a thrust of 1.0 units is commanded, the bias results in 1.2 units being produced. The bias affects the control force much like damping affects a second order harmonic oscillator. A bias less than 1.0 is like an overdamped oscillator in that the control force starts out less than the actual disturbing force and slowly approaches a steady state value. Similarly, a bias between 1.0 and 2.0 is like an underdamped oscillator in that the control force initial oscillates about the disturbing force, but will eventually settle to a steady state value. A bias equal to or greater than 2.0 will create an uncontrollable situation. This can be seen in the following examples: Let the bias be 2.0. When the control system commands a force of 1 unit, 2 units are produced, 1 too many. The system then commands -1 units to correct and -2 units are produced, giving a net of -1. The system oscillates continuously and never achieves the commanded value. Now suppose the bias is 3.0. The control system commands 1 unit of force and 3 units are produced. The system then commands -2 units to correct and -6 are produced. The system oscillates out of control.

3.5.2 Results

Eq. (35-1) was used to see how closely the control force could follow the disturbing drag force while varying the bias. Even if the bias was 1 (i.e. no errors in system), there would still be some lag due to the fact that the current control force is based on 66 seconds of preceding data. Figure 35-1 shows the maximum steady state error between the actual disturbing acceleration and the thruster acceleration in g's for a bias ranging from 0.5 to 1.9.
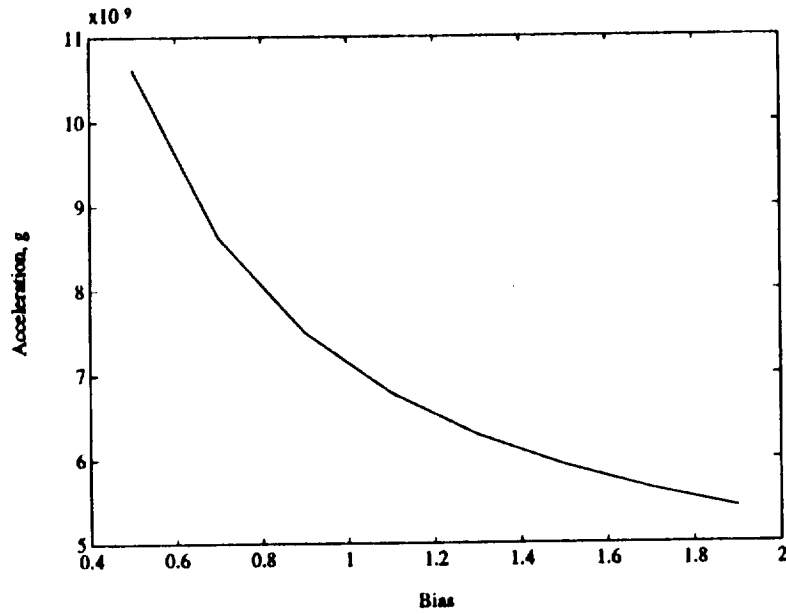
Figure 35-1 Control force acceleration error vs system bias.

Note that the error continues to decline as the bias increases. This is because the bias is helping to compensate for the error between the predicted disturbance and the actual disturbance.
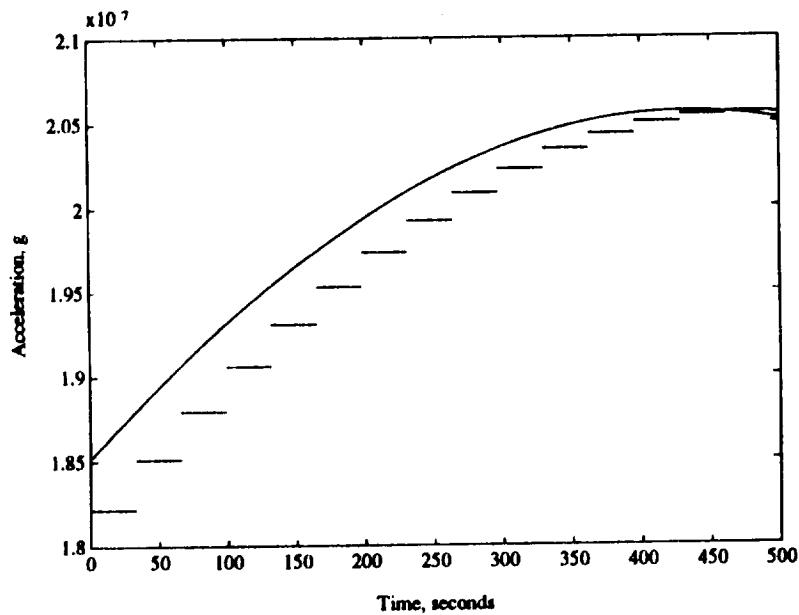
Figure 35-2 Disturbance and control force acceleration , bias = 1.

Figure 35-2 and Figure 35-3 show the magnitude of the drag and control accelerations
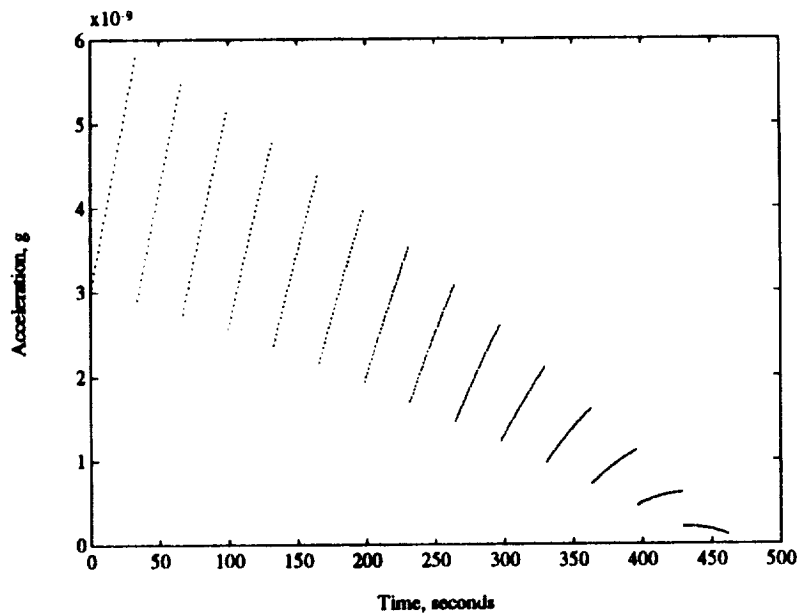
Figure 35-3 Acceleration error, bias = 1.
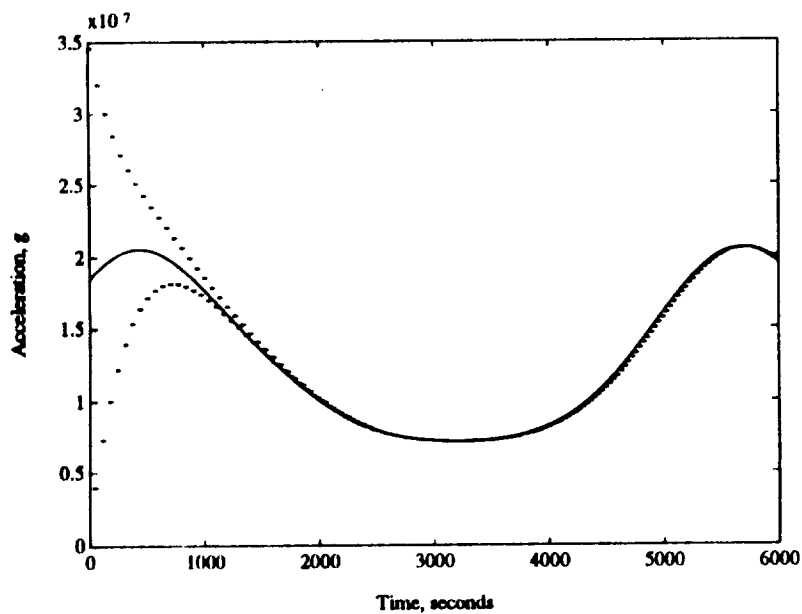
Figure 35-4 Disturbance and control force acceleration , bias = 1.9.

over the first 500 seconds and the error between the drag and control force over the first 500 seconds for a bias of 1.0.   Figure 35-4 through Figure 35-7 show the magnitude of the drag and control accelerations over the first orbit of operation and the error between the two over the first orbit of operation for a bias of 1.9 and 0.5. Note the changes in the scale of each graph.

3-36
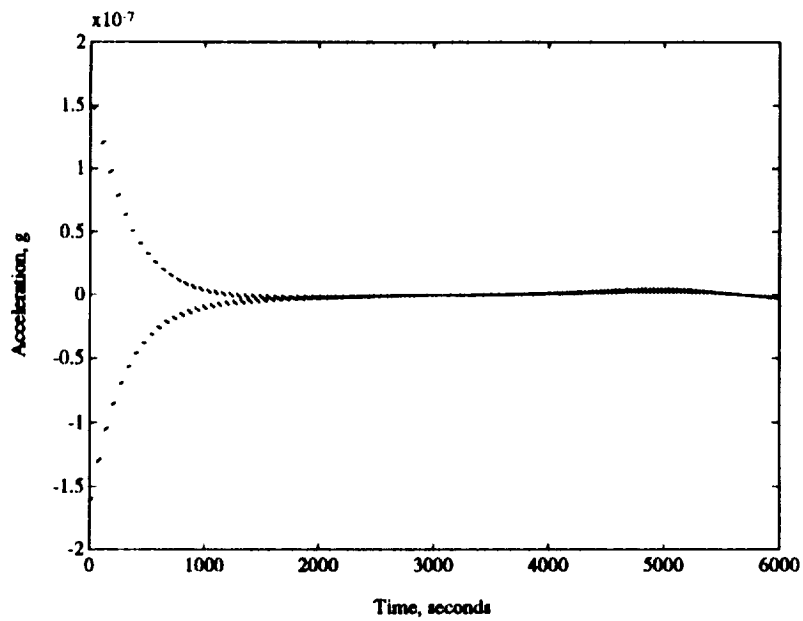
Figure 35-5 Acceleration error, bias = 1.9.
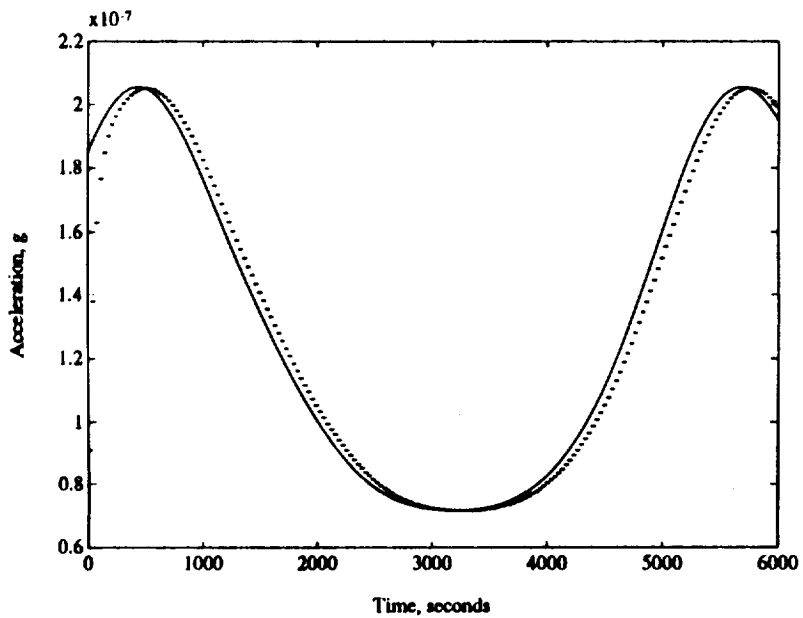
Figure 35-6 Disturbance and control force acceleration , bias = 0.5.

A study was also performed to examine the effect noise in the OARE data would have on the control force. A simple gaussian noise signal with standard deviations of 10^{-6}g's was added to the OARE data. The data was then averaged and processed as above. Figure 35-8 shows the error between the control force with noise and the disturbing drag force. The level
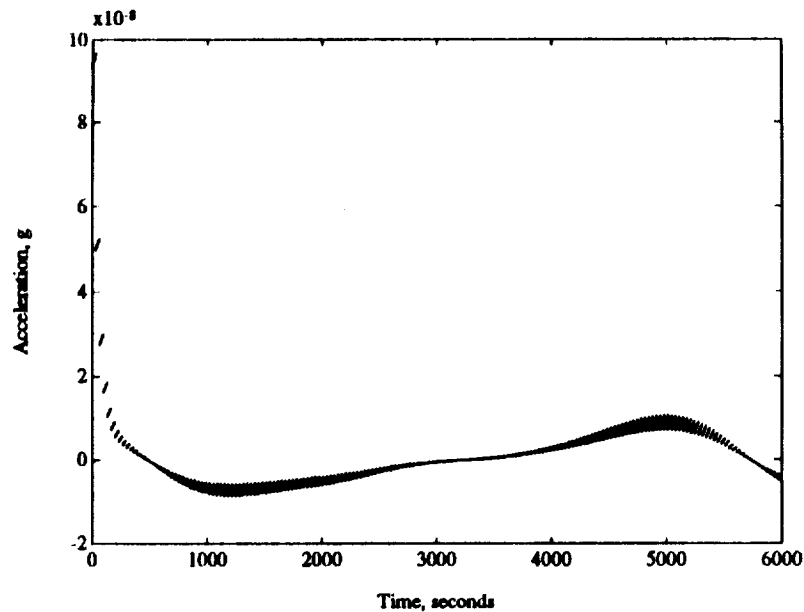
Figure 35-7 Acceleration error, bias = 0.5.

is consistent with the quoted OARE accuracy and is below 10^{-8} g's, the resolution of the MESYS. Therefore, noise will be ignored in the remainder of this study.

3.5.3 Conclusions

Even with a bias of 1.9, the system will settle to a steady state error less than 0.01 μ-g within 1 orbit. The system will go unsteady as the bias approaches 2.0, but it is not reasonable to expect a bias this high. Therefore, two main conclusions can be reached from this study: 1) that averaging OARE data from the previous 66 seconds as the prediction for the next time step will allow the control force to follow the disturbance force to within the tolerance required of the MESYS, and 2) that the system can compensate for a bias less than 1.0 and will benefit from a bias greater than 1.0. It was also concluded that the anticipated noise produced by the OARE (on the order of 10^{-6} g's) will produce an error of less than 10^{-8} g's on the control force. Therefore, noise will be ignored in the rest of this study.
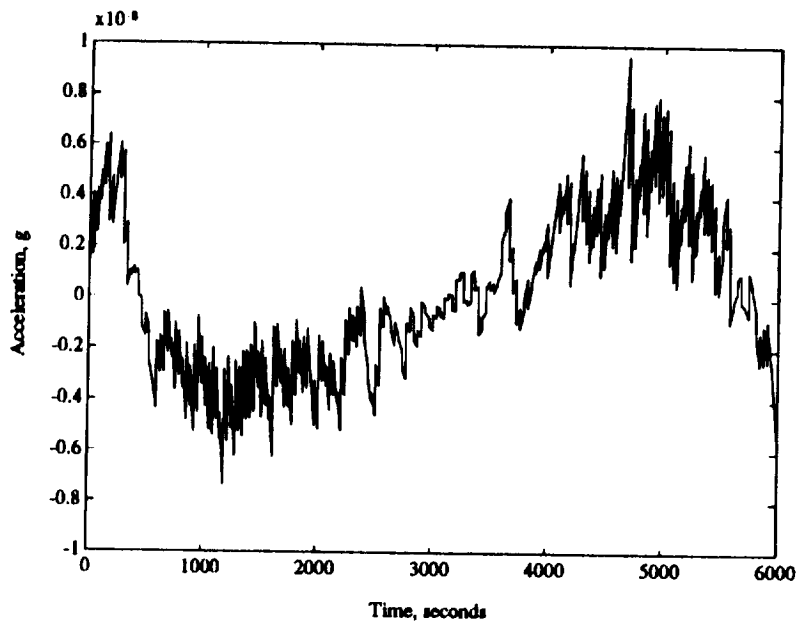
Figure 35-8 Acceleration error with noise.

3.6 ACCELERATION FEEDBACK CONTROL SYSTEM

Now that the linear equations of motion have been derived the acceleration feedback control system can be designed. Simply put, the control system will take the OARE measured value of the acceleration and command the thrusters to cancel that acceleration while the attitude control system maintains attitude control. The performance of the acceleration feedback control system is described in section 4.1.

The linear equations of motion for an objects motion relative to another can be used with only slight modifications to derive the acceleration level the OARE accelerometer will measure. Recall from section 3.2 that the equations of motion are

$$\ddot{\rho} = -\mu \left(\frac{R}{|R|^3} - \frac{R_{cm}}{|R_{cm}|^3} \right) - 2(\omega \times \dot{\rho}) - \dot{\omega} \times \rho - \omega \times (\omega \times \rho) + \frac{F}{m} \qquad (36\text{-}1)$$

and

3-39

$$\dot{\omega}_{body} = I^{-1}(N - \omega \times I\omega_{body}) \qquad (36\text{-}2)$$

with Eqs. (32-10), (32-12), (32-13) and (32-14) from that section substituted to achieve the linearized form.

The equations of motion were derived to describe the motion of one object moving relative to another object. The OARE accelerometer uses an electrostatically balanced proof mass to sense disturbances. Since it is balanced as such, the proof mass will have no relative motion with respect to the center of mass of SSF (i.e. no motion in the body fixed coordinate system) so therefore there is no small deviation of the proof mass. Equation (32-13) from section 3.2 will reduce to

$$\rho = L^T \begin{bmatrix} x_0 \\ y_0 \\ z_0 \end{bmatrix} \qquad \dot{\rho} = \begin{bmatrix} 0 \\ 0 \\ 0 \end{bmatrix} \qquad \ddot{\rho} = L^T \begin{bmatrix} \ddot{x} \\ \ddot{y} \\ \ddot{z} \end{bmatrix} \qquad (36\text{-}3)$$

These equations can now be integrated over time to simulate the motion of SSF. To conform with the 33 second firing period the SSF attitude control system uses, the equations will be integrated over 33 second periods. After each 33 second integration period, the control force will be updated with disturbance data measured by OARE. The disturbance data is simulated in two parts: a) the atmospheric drag accelerations and b) the rotational and gravity gradient accelerations. The atmospheric drag accelerations are computed using the algorithms described in section 3.5. The rotational and gravity gradient are calculated from the output of the numerical integration. Note that while this control system is controlling the translational motion, the standard SSF rotational control system will be maintaining attitude hold.

Since the equations of motion have been linearized about a defined state, the control system created from these equations will act based on deviations from this point. A steady state control force must be added to this variable control force to account for the fact that the OARE is not at the center of mass. These steady state control forces for MTC in the LVLH orientation at 220 nmi are

$$F_{c\ ss} = |\ 0\ -1.5164\ -1.0460|\quad N$$

3.7 PROOF MASS CONTROL SYSTEM

Like the acceleration feedback control system, the proof mass control system requires the linearized equations of motion. The proof mass control system will feedback the position, velocity and integral of the position of the proof mass to the control thrusters to keep the proof mass centered in the cavity. This is commonly referred to as a PID (Proportional Integral Derivative) control system.

The equations of motion of the proof mass relative to SSF center of mass are given by the equations in section 3.2

$$\ddot{\rho} = -\mu\left(\frac{R}{|R|^3} - \frac{R_{cm}}{|R_{cm}|^3}\right) - 2\omega \times \dot{\rho} - \dot{\omega} \times \rho - \omega \times (\omega \times \rho) + \frac{F}{m} \qquad (37\text{-}1)$$

and

$$\dot{\omega}_{body} = I^{-1}(N - \omega \times I\omega_{body}) \qquad (37\text{-}2)$$

with Eqs. (32-10), (32-12), (32-13) and (32-14) from section 3.2 substituted to achieve linearization. Note that F in Eq. (37-1) includes both control and atmospheric forces and similarly N in Eq. (37-2) includes control, gravity gradient and atmospheric torques.

3-41

A PID control system was chosen to control the motion of the proof mass relative to SSF's center of mass. The PID has an advantage over a PD control system in that the integral feedback term will insure that the proof mass will return to the center of the cavity. In a PD system, the proof mass will tend to remain offset from the center of the cavity. The control gains were calculated using a Linear Quadratic Regulator (LQR) algorithm. The LQR determines the gain matrix to minimize a user defined cost function. For this case here, the cost function was the sum of the squares of the components of the acceleration of the proof mass. The gain matrices were calculated to be

$$
\mathbf{K_I} = \begin{vmatrix} 2.2018 \times 10^{-06} & 7.6084 \times 10^{-11} & -9.3627 \times 10^{-10} \\ -1.8369 \times 10^{-10} & 2.1871 \times 10^{-06} & -2.5426 \times 10^{-07} \\ 9.2122 \times 10^{-10} & 2.5426 \times 10^{-07} & 2.1871 \times 10^{-06} \end{vmatrix}
$$

$$
\mathbf{K_p} = \begin{vmatrix} 3.3851 \times 10^{-04} & -1.1809 \times 10^{-06} & -6.2841 \times 10^{-07} \\ 1.2689 \times 10^{-06} & 3.3879 \times 10^{-04} & -3.9476 \times 10^{-05} \\ 7.5436 \times 10^{-08} & 3.8261 \times 10^{-05} & 3.4199 \times 10^{-04} \end{vmatrix}
$$

$$
\mathbf{K_D} = \begin{vmatrix} 2.6020 \times 10^{-02} & 2.1346 \times 10^{-06} & -1.0486 \times 10^{-05} \\ 2.1346 \times 10^{-06} & 2.6131 \times 10^{-02} & -2.8248 \times 10^{-05} \\ -1.0486 \times 10^{-05} & -2.8248 \times 10^{-05} & 2.6248 \times 10^{-02} \end{vmatrix}
$$

The control force can then be calculated using

$$F_c = -mK_I \begin{bmatrix} \int x\, dt \\ \int y\, dt \\ \int z\, dt \end{bmatrix} - mK_P \begin{bmatrix} x \\ y \\ z \end{bmatrix} - mK_D \begin{bmatrix} \dot{x} \\ \dot{y} \\ \dot{z} \end{bmatrix} \tag{37-3}$$

An electrostatic device similar to the one described in section 2.2.2 will be used to measure the position of the proof mass. The position data can be summed and then multiplied by the time interval between measurements to compute the integral of the position. Similarly, by subtracting the n-1 data point from the n-th data point and then dividing by the time interval between measurements, the velocity of the proof mass can be determined.

Since these equations have been linearized about a defined state, the control system created from these equations will act based on deviations from this point. Note that if the proof mass is fixed at the center of the cavity, i.e. all deviations are zero, the control force will become zero. As in the acceleration feedback control system, a steady state control force must be added to this variable control force to account for the fact that the cavity is not at the center of mass. These steady state control forces for MTC in the LVLH orientation at 220 nmi are

$$F_{css} = |\, 0 \quad -1.5164 \quad -1.0460\,| \quad N$$

3-43
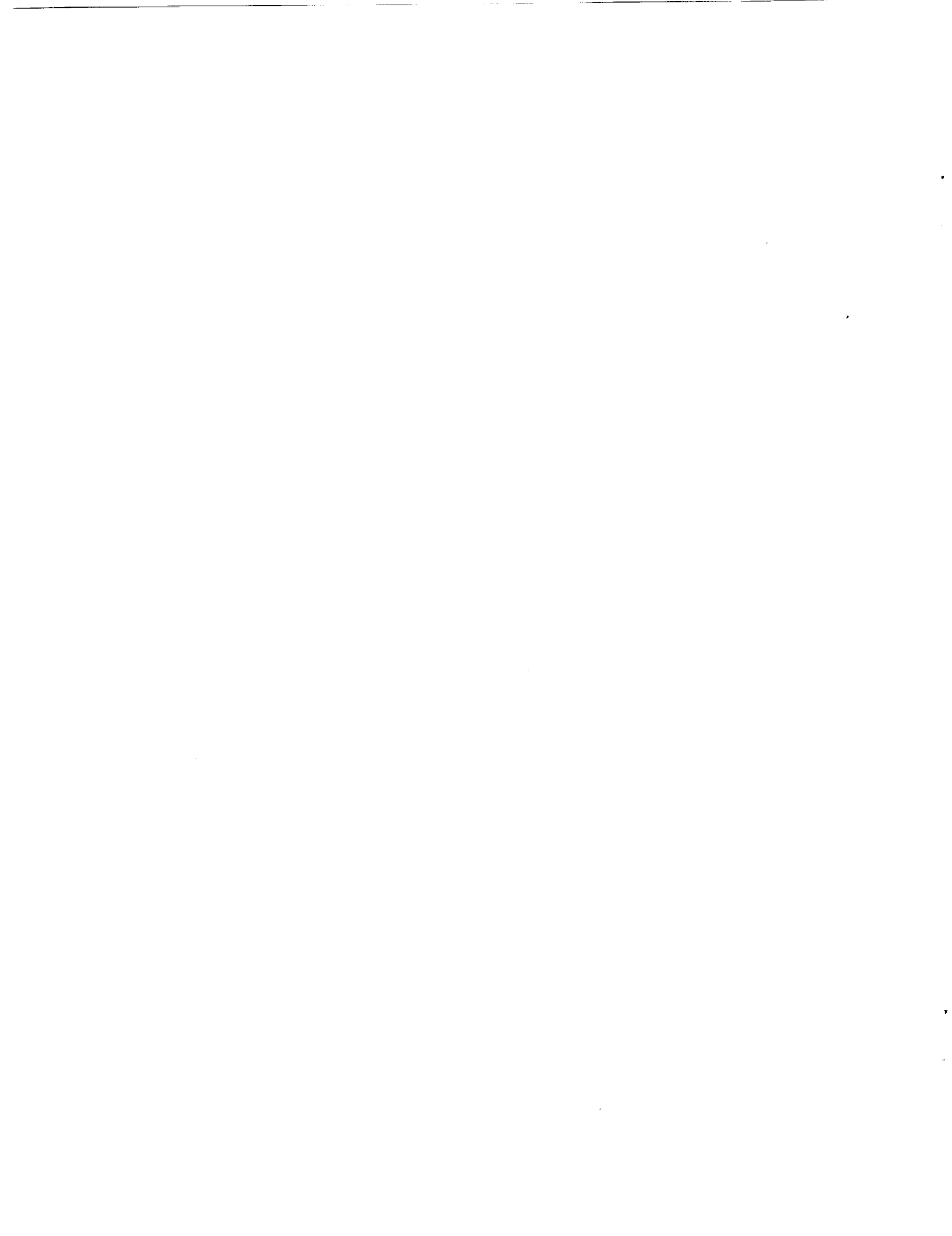
4.0 MESYS PERFORMANCE AT MTC

This chapter describes the performance of both the acceleration and proof mass control systems and assesses the impact on SSF for MTC.

4.1 ACCELERATION FEEDBACK SYSTEM PERFORMANCE

The acceleration feedback control system described in section 3.6 was tested under conditions of minimum, average and maximum atmospheric drag conditions. Figure 41-1 shows the acceleration recorded by the OARE during MESYS operation with average atmospheric conditions at 220 nmi.
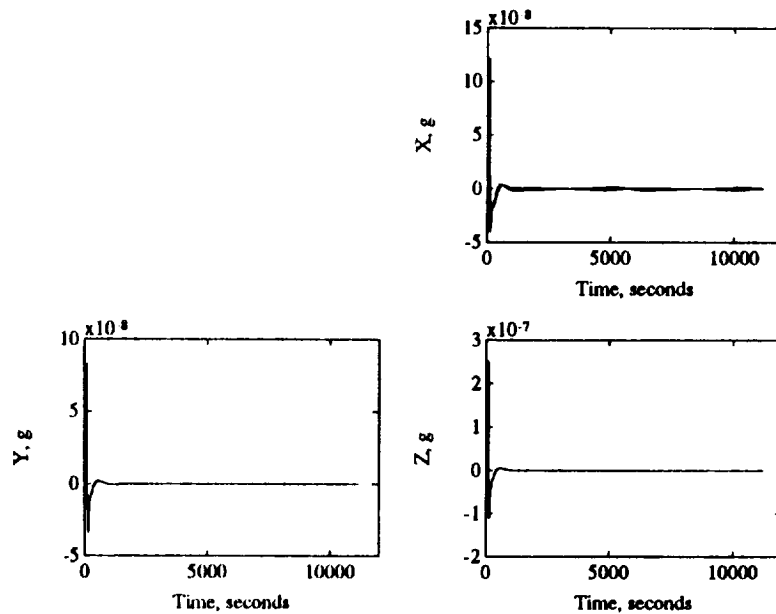
Figure 41-1 Acceleration in the laboratory module, MTC.

After the initial transients decay, the acceleration level reaches a steady state condition on the order of 10^{-8} g's. Here it can be seen that the acceleration level in the x direction does not reach a steady value as does the acceleration in the y or z directions. This is due to the fact that the control force is not able to follow precisely the variations in the drag force, which is

acting in the x direction. This error between the drag force and control force leads to the higher

acceleration level. In the y and z directions, the primary disturbing force is gravity gradient. Since this force is essentially constant, the error between it and the control force is much less.

While the translational control system is commanding a control force to minimize the acceleration level in the laboratory module, the nominal attitude control system will be commanding a control torque to maintain SSF in the LVLH orientation. Both these commanded values are input to the linear programming algorithms described in section 3.4 to determine the required thruster forces to satisfy both control requests. Figure 41-2 shows the requested control force from the translational control system. Variations in the atmospheric drag force can be seen in the x direction. The gravity gradient disturbance forces are constant (at this altitude) and this is reflected in the constant control forces in the y and z directions.
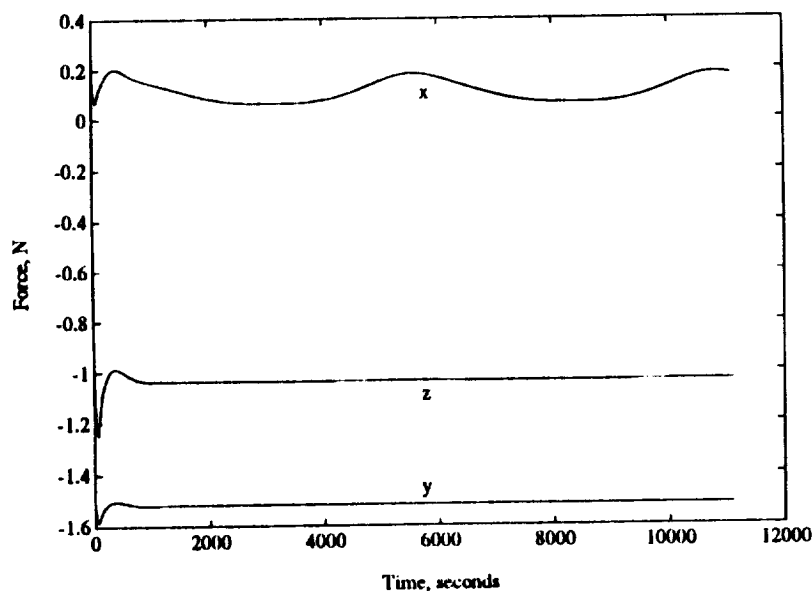
Figure 41-2 Requested control force, MTC.

Figure 41-3 shows the individual thruster forces required to satisfy both control systems. Refer to section 2.3.2 for thruster numbering conventions and firing directions. Thrusters 5 and

4-2
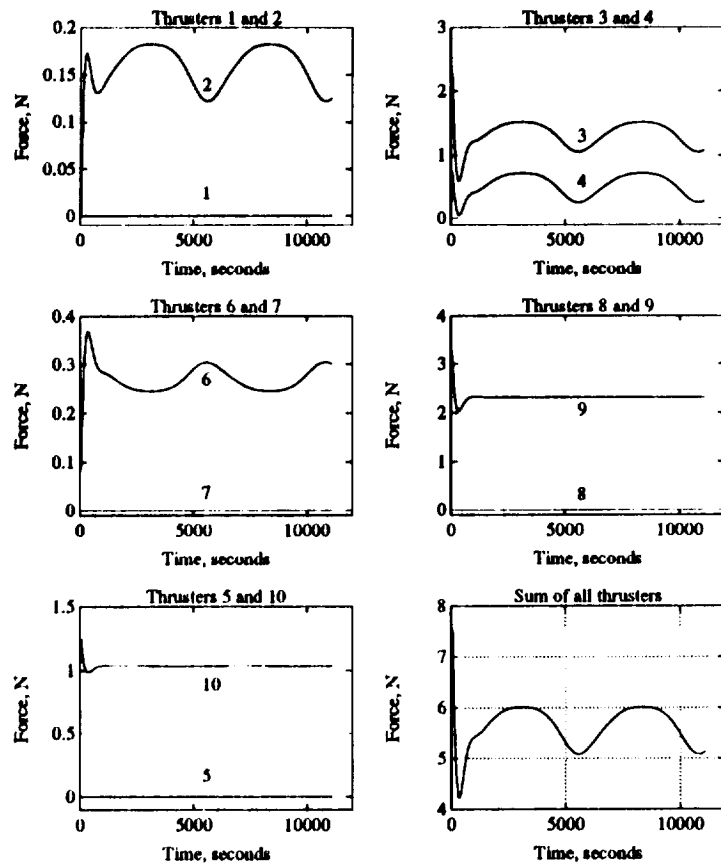
Figure 41-3 Applied thruster forces, MTC.

10 control translation in the z direction and control torques about the x and y directions. Recall that when SSF is in the LVLH orientation, the orbital and body reference coordinate systems are aligned and can be used interchangeably. Since thruster 10's output exactly matches the requested force in the z direction, it must not be controlling any torque about the x and y directions. Therefore, thrusters 1,2,6 and 7, which control translation in the x direction and torques about the y and z directions must be controlling all the torques about the y direction. Similarly, thrusters 3,4,8 and 9, which control translation in the y direction and torques about the x and z directions must be controlling all the torques about the x direction. It is unclear from

4-3

this analysis how much of the torque about the z direction is being controlled by thrusters 1,2,6 and 7 and how much is being controlled by thrusters 3,4,8 and 9. Also, these results match the results observed in section 3.4. Once the initial transients decay, the system reaches a quasi-static steady state observed in section 3.4.

Figure 41-4 shows during an average period the steady state acceleration under conditions of maximum atmospheric drag at 200 nmi. Note that the acceleration is on the order of a magnitude greater than that observed during average atmospheric conditions.
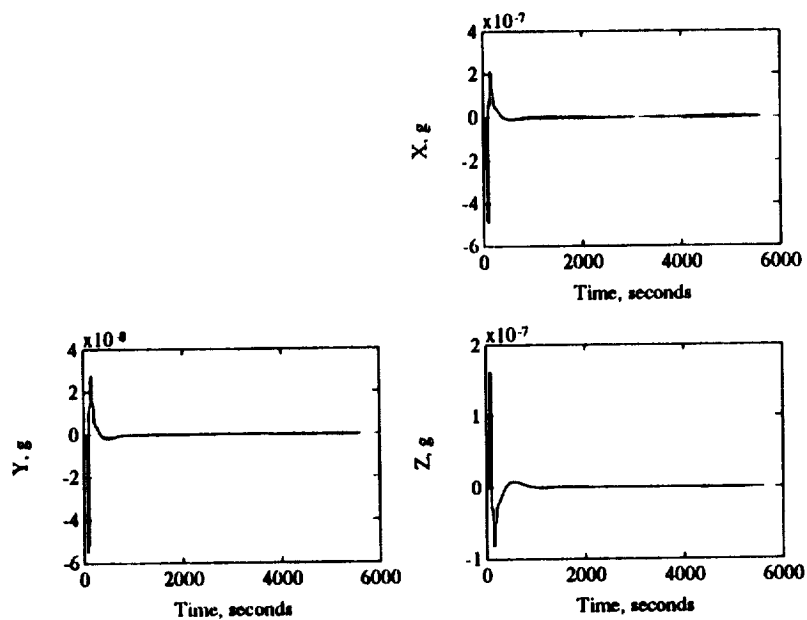
Figure 41-4 Acceleration in the laboratory module, maximum atmospheric conditions, MTC.

Figure 41-5 shows the requested control force over the first orbit of operations under conditions of maximum atmospheric drag. The control force in the x direction reflects the greater atmospheric drag (close to 1 newton greater than average atmospheric conditions) and the forces in the y and z are nearly equal to the values observed in the case of average atmospheric conditions. Again, this is because gravity gradient forces in the y and z directions are nearly constant from 200 nmi to 220 nmi. These results also match the quasi-static steady state results

observed in section 3.4.
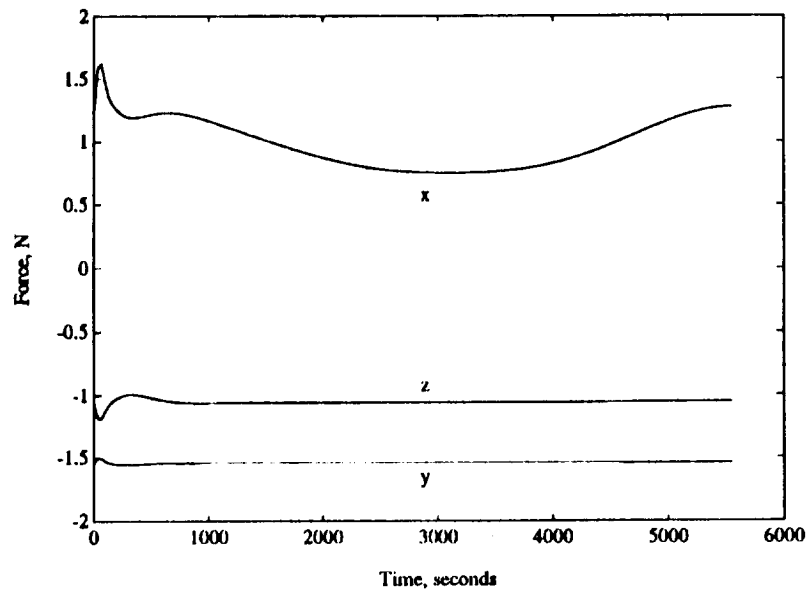
Figure 41-5 Requested control force, maximum atmospheric conditions, MTC.

Figure 41-6 shows the applied thruster forces required to control SSF during conditions of maximum atmospheric drag. Even though the requested force has increased only about 1 newton from the average atmospheric case, the total applied force has increased about 6 newtons. This shows that the majority of the applied force is acting to cancel the gravity gradient and drag torques.

The acceleration feedback control system was also tested under conditions of minimum atmospheric drag at 240 nmi. Figure 41-7 shows the acceleration during the first orbit of operation. Now the acceleration level in the y and z directions are on the order of a magnitude less than those observed in case of average atmospheric conditions.

Figure 41-8 and Figure 41-9 show the requested control force and the applied thruster forces for minimum atmospheric conditions. The figure shows that the total applied force is greater than that observed in the case of average atmospheric conditions. As was observed and

4-5
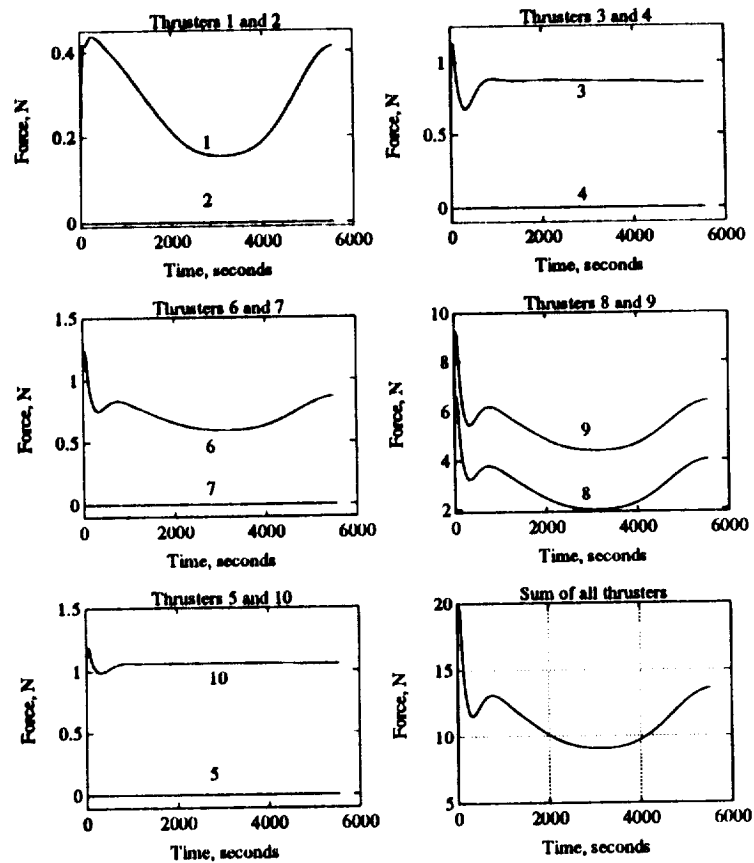
Figure 41-6 Applied thruster forces, maximum atmospheric conditions, MTC.

described in section 3.4, this is due to the drag torques partially cancelling the gravity gradient torques. The minimum drag force does not apply as much cancelling torque which must be made up by the thrusters. The maximum drag force applies too much torque, which has to be cancelled by the thrusters. Again, these results match the quasi-static steady state results observed in section 3.4.
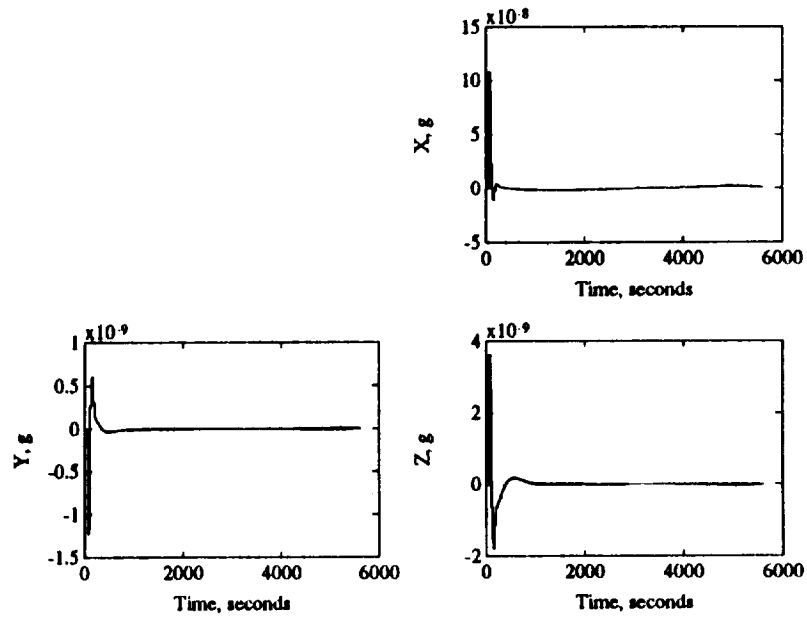
Figure 41-7 Acceleration in the laboratory module, minimum atmospheric conditions, MTC.
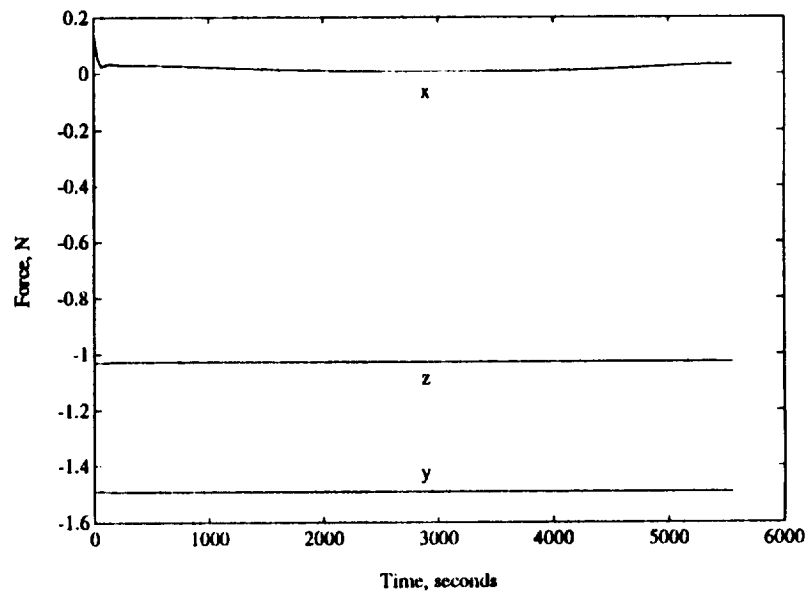
Figure 41-8 Requested control force, minimum atmospheric conditions, MTC.
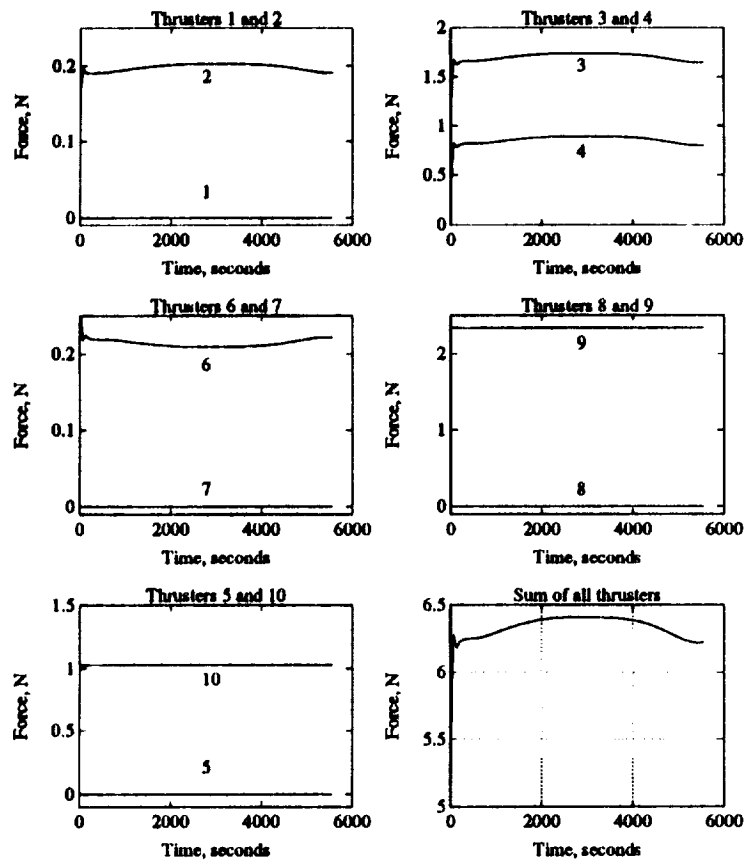
Figure 41-9 Applied thruster forces, minimum drag conditions, MTC.

4.2 PROOF MASS CONTROL SYSTEM PERFORMANCE

Like the acceleration feedback control system, the control force is updated every 33 seconds. While this system is controlling the translational motion, the standard SSF attitude control system will be maintaining attitude hold. Figure 42-1 and shows the position of the proof mass in the cavity for average atmospheric conditions with SSF in the nominal LVLH orientation.

It can be seen that in the y and z directions, the proof mass returns to and remains at the center of the cavity. As was stated in section 3.7, this is due to the PID control system. The
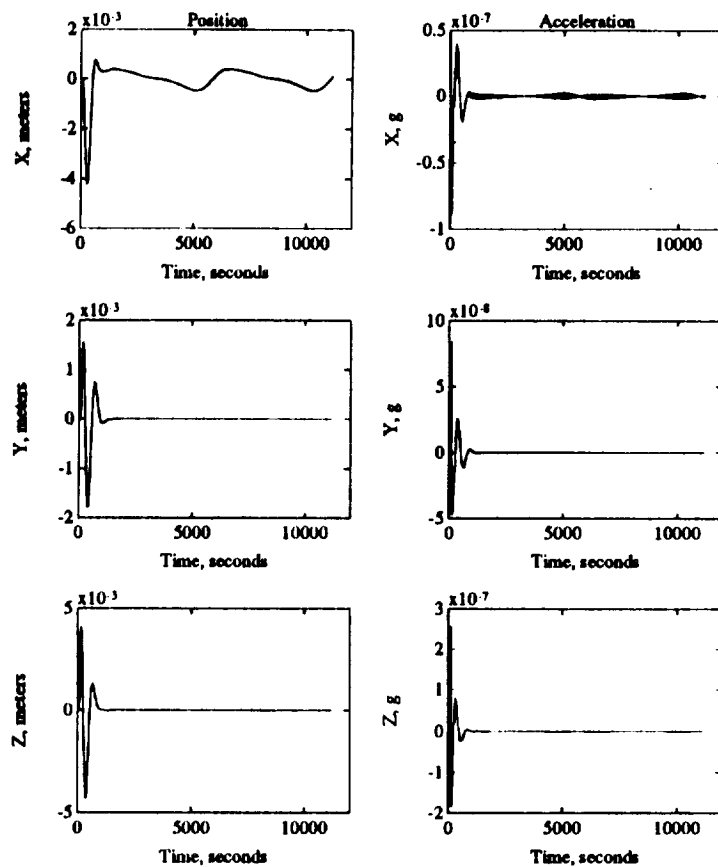
Figure 42-1 Relative position and acceleration of the proof mass, MTC.

integral feedback term in the control law drives the position to zero. Since the disturbance forces in the x direction (namely atmospheric drag) are varying over time, the proof mass does not remain centered in the x direction but oscillates about the center.

Figure 42-1 also shows the acceleration of the proof mass relative to SSF. Once the initial transients subside, the acceleration settles to a level below 10^{-8} g's, maximum acceleration allowed by the MESYS.

Both the translational and attitude control systems will independently command a required control force and torque, respectively and using the linear programming techniques discussed in
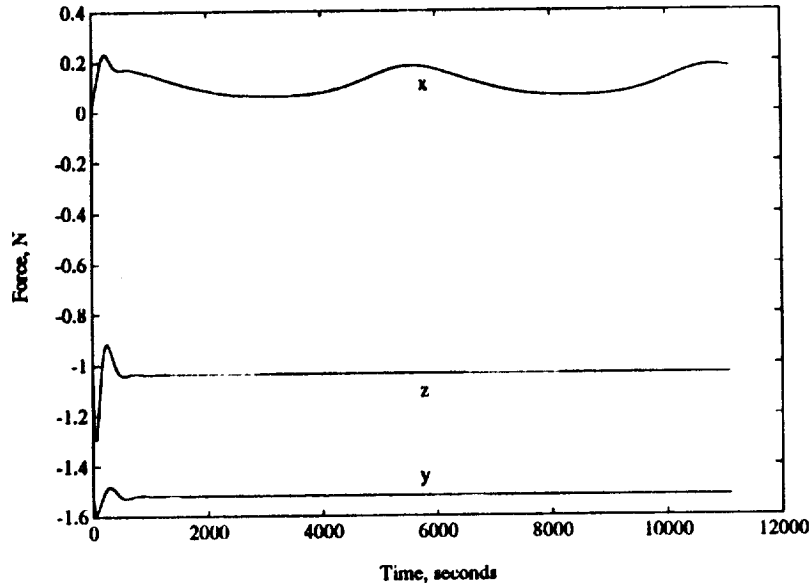
Figure 42-2 Requested thruster control forces, MTC.

section 3.4, the required thruster forces can be determined. Figure 42-2 shows the requested

force from the control system. The force in the y and z direction are constant over the two orbits

since the disturbing forces in these directions are due primarily to gravity gradient forces which

do remain constant at a fixed altitude. For eccentric orbits, the gravity gradient forces will vary

with the cube of the eccentricity. In the x direction, however, the principle disturbing force is

the atmospheric drag which varies over an orbit. This variation shows in the x direction

commanded force. Figure 42-3 shows the output of the linear programming algorithm. These

are the required thruster forces to both control the acceleration in the laboratory module and hold

SSF in the LVLH orientation. Refer to section 2.3.2 for thruster numbering and firing direction

conventions.

Figure 42-4 shows the displacement and acceleration of the proof mass relative to SSF

over the first orbit of operation assuming maximum atmospheric conditions. Now the

maximum displacement is on the order of 40 millimeters. Unless this initial transient can be

4-10
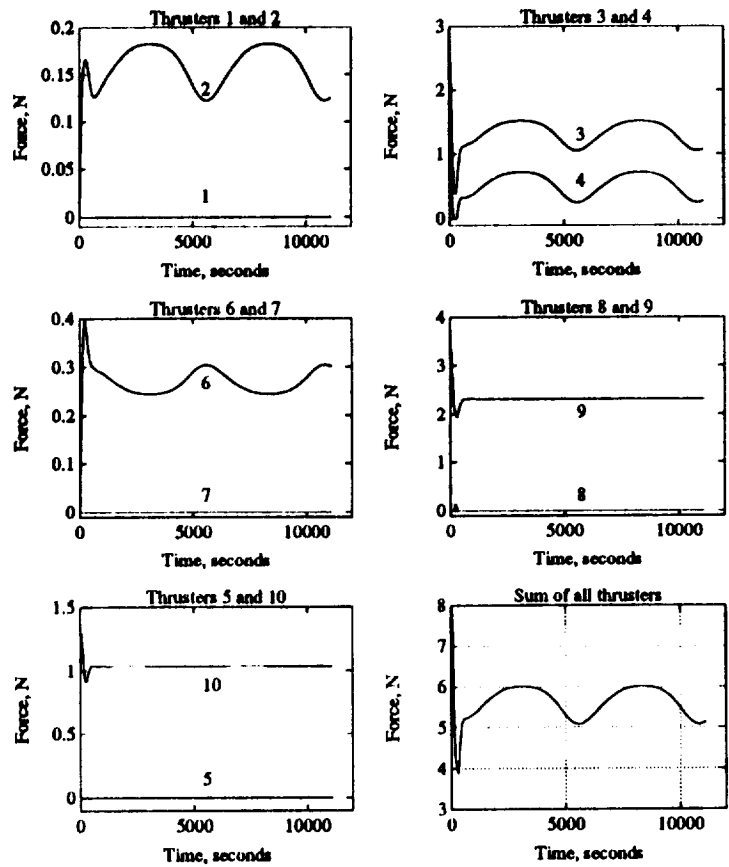
Figure 42-3 Applied thruster forces, MTC.

minimized, the proof mass cavity will be required to have a radius of at least this amount to be able to handle all atmospheric conditions. And, the acceleration level is greater than that observed in the case of average atmospheric conditions, but is still below the design limits of the MESYS.

Figure 42-5 and Figure 42-6 show the requested control force and the applied thruster forces for maximum atmospheric conditions. The only major difference between Figure 42-5 and Figure 42-2 is the force in the x direction, which is compensating for atmospheric drag. Even though the maximum atmospheric conditions produce only about 1 extra newton of drag

4-11
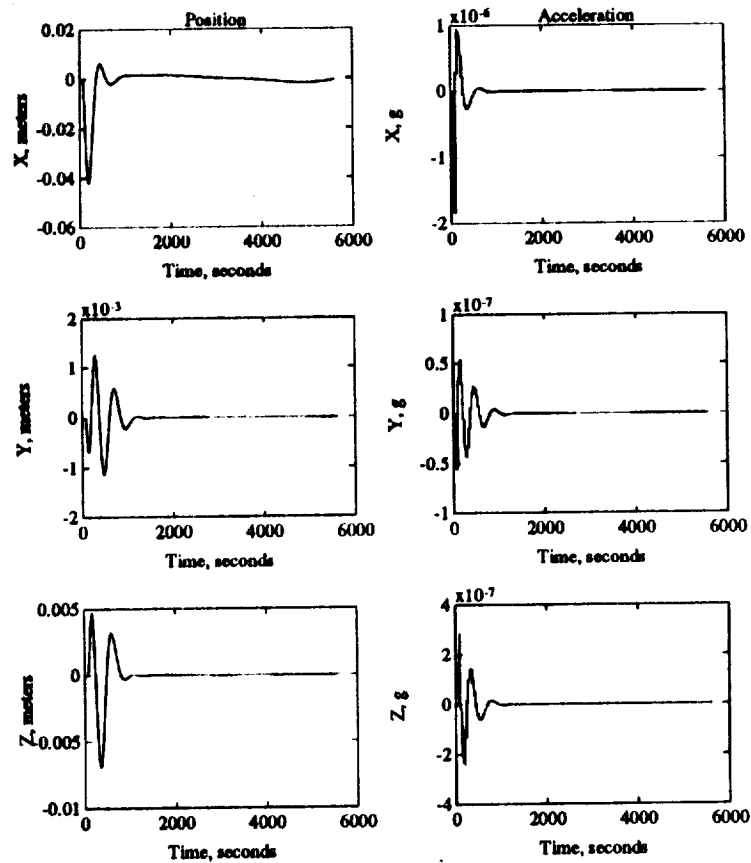
Figure 42-4 Relative displacement and acceleration of the proof mass, maximum atmospheric conditions, MTC.

force, the linear programming algorithm requires more than 6 extra newtons of force to properly control SSF. The majority of this extra control force is needed to compensate for the large drag torques.

Figure 42-7 shows the position and acceleration of the proof mass relative to SSF for minimum atmospheric conditions and now the maximum displacement is measured in tenths of millimeters. Also, the steady state acceleration levels show at least an order of magnitude improvement over the maximum atmospheric conditions.

4-12
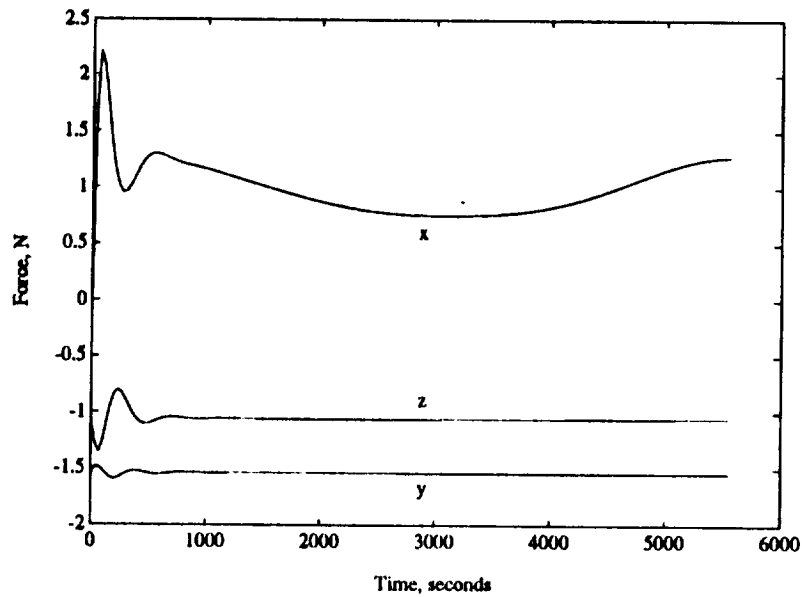
Figure 42-5 Requested control force, maximum atmospheric conditions, MTC.

Figure 42-8 and Figure 42-9 show the requested control force and the applied thruster forces for minimum atmospheric conditions. Again, the only major difference in the requested force here and in the previous cases is in the drag compensating x direction. Even though the drag force here is much less than in the average atmospheric conditions, the total applied thruster forces are approximately the same. Once again, this shows that the majority of the applied force acts to control disturbing torques.
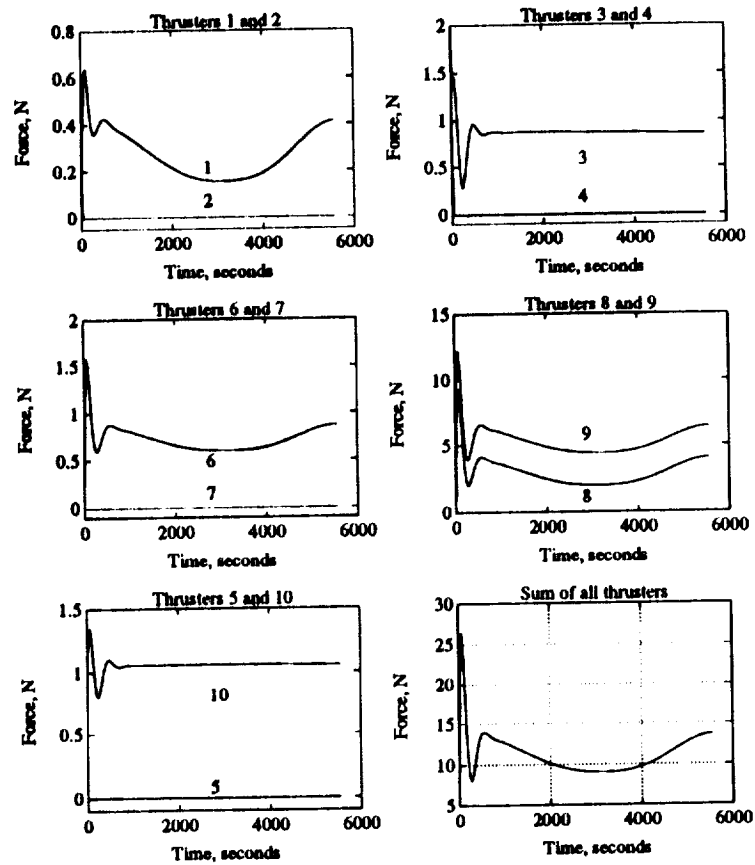
Figure 42-6 Applied thruster forces, maximum atmospheric conditions, MTC.
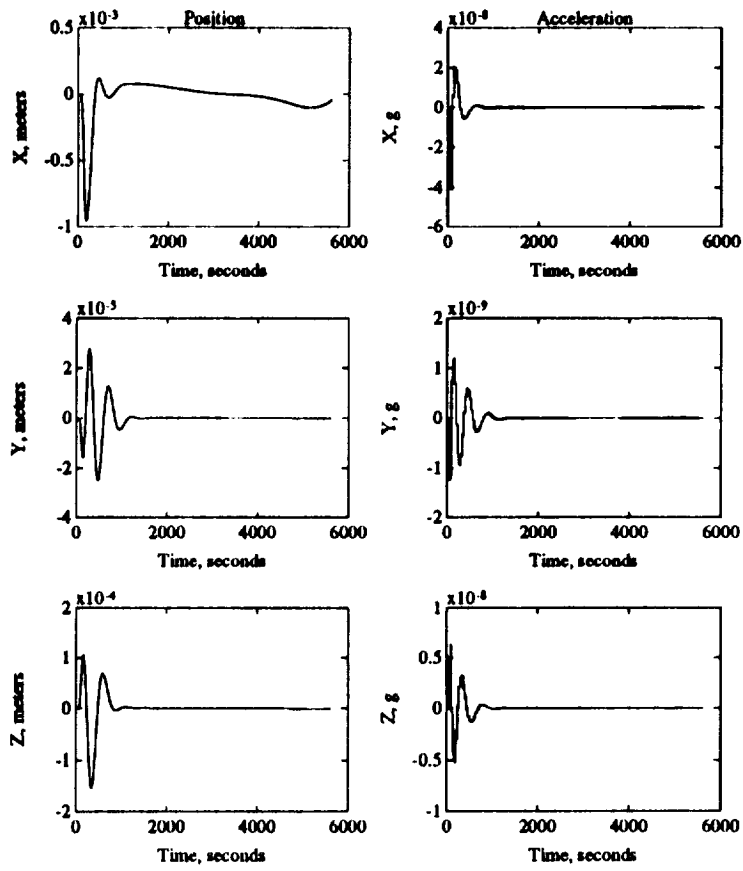
Figure 42-7 Relative displacement and acceleration of the proof mass, minimum atmospheric conditions, MTC.
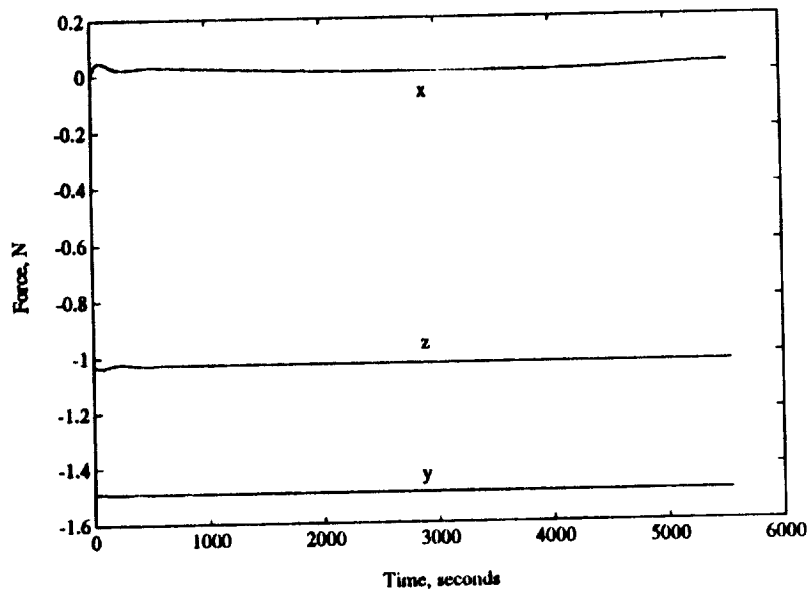
Figure 42-8 Requested control force, minimum atmospheric conditions, MTC.
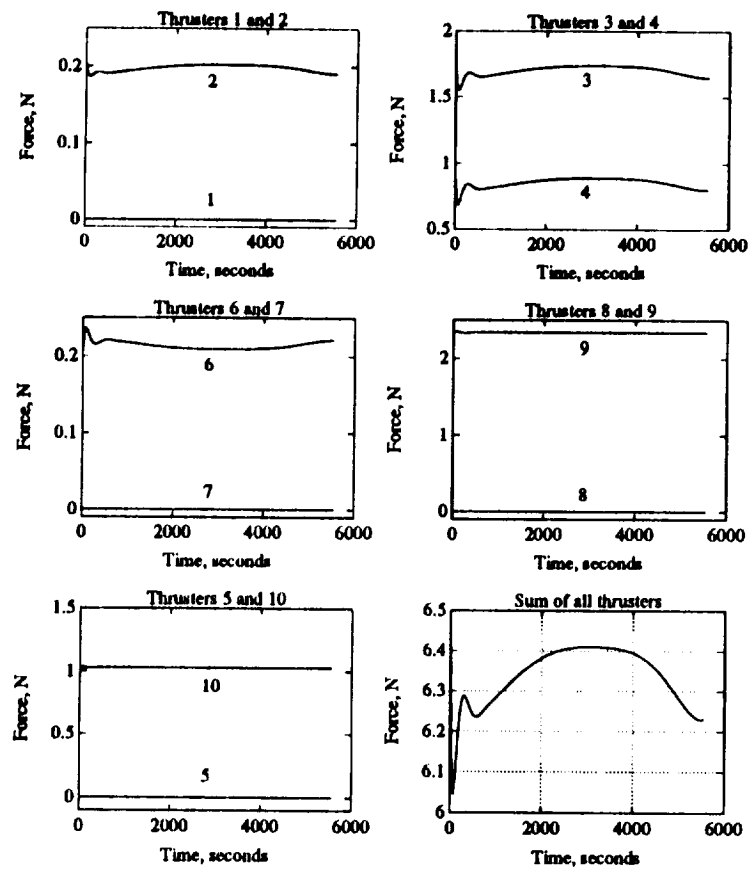
Figure 42-9 Applied thruster forces, minimum atmospheric conditions, MTC.

4.3 THRUSTER REQUIREMENTS

With the exception of the initial transient phase, the acceleration feedback system and the proof mass system will require the same thruster forces to control the acceleration level in the laboratory module. This is not an unexpected result. In quasi-steady state condition, the required force is purely a function of the disturbing acceleration and not a function of the measurement device or feedback system. This fact is shown when comparing the required thruster forces from sections 4.1 and 4.2.

The primary source of variations in the required thruster forces is atmospheric drag. The MESYS thrusters must have the dynamic range to cover all reasonable atmospheric conditions. Table 43-1 shows the steady state thrust range for each thruster under minimum, average and maximum atmospheric conditions.

Table 43-1 Steady state thruster requirements, N.

Thruster Number	Minimum Atmosphere	Average Atmosphere	Maximum Atmosphere
1	0.0	0.0	0.15 - 0.44
2	0.19 - 0.20	0.12 - 0.18	0.0
3	1.62 - 1.74	1.05 - 1.51	0.88
4	0.78 - 0.89	0.25 - 0.71	0.0
5	0.0	0.0	0.0
6	0.21 - 0.22	0.24 - 0.30	0.59 - 0.87
7	0.0	0.0	0.0
8	0.0	0.0	1.99 - 4.02
9	2.33	2.32	4.39 - 6.41
10	1.03	1.04	1.06

Refer to section 2.3.2 for thruster numbering conventions and firing directions. The greatest required dynamic range for a single atmosphere is approximately 3. This is for thruster 1 during maximum atmospheric conditions and for thruster 4 during average atmospheric conditions. As stated in section 2.3.1, this is currently within the state of the art for throttle-able arcjet thrusters. Remember that a given thruster will not be required to have the dynamic range for all atmospheres. Since the atmospheric conditions can be predicted to some degree of precision, the

proper thrusters with the necessary dynamic range can be chosen and installed on SSF to match the predicted atmospheric conditions expected during MESYS operation.

4.4 PERFORMANCE WITH HIGH FIDELITY ATTITUDE CONTROL SYSTEM MODEL

The full non-linear set of translational equations of motion were evaluated with a high fidelity model of the SSF attitude control system. See section 2.1.8 for a description of this model. One of the goals of MESYS is to use as much of the SSF hardware and software as is possible. It is necessary to see how the assumptions made in MESYS (such as linearizing the equations of motion, using the LQR function to derive the control laws, using the 10 jet linear programming, etc) will affect the operation of the MESYS with the actual SSF it simulates. An analysis of the MESYS using a high fidelity model of the SSF reaction control system will help to confirm the validity of these assumptions.

Figure 44-1 shows the acceleration recorded in the laboratory module by the acceleration feedback control system under average atmospheric conditions. The results are very similar to those discussed in section 4.1. The acceleration has been held to below 10^{-8} g's.

Figure 44-2 shows the position and acceleration of the proof mass relative to SSF using the high fidelity model of the SSF control system and under average atmospheric conditions. Again, these results are very similar to those observed in section 4.2.

Figure 44-3 shows the control force requested from the acceleration feedback system. This force is almost identical to the results shown in section 4.1. The non-linear proof mass control system also produced nearly similar results and need not be presented here.
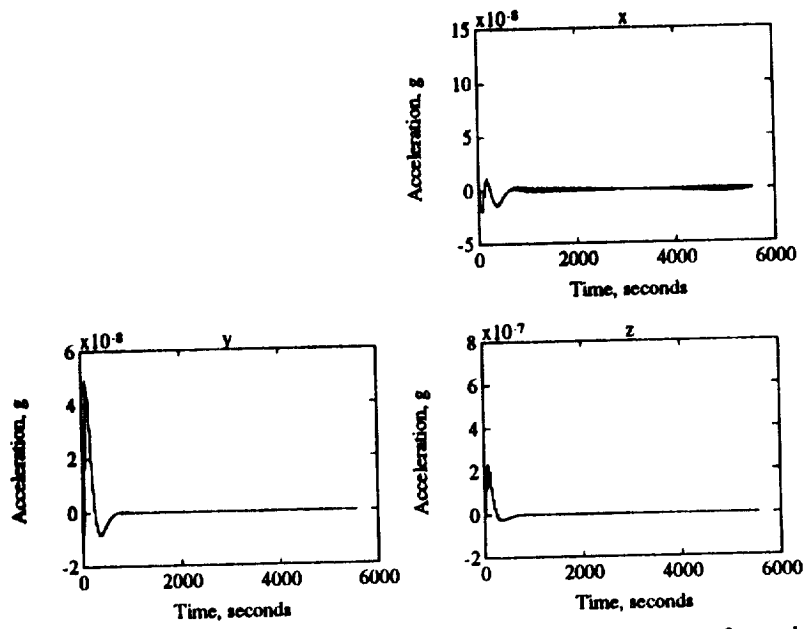
Figure 44-1 Acceleration in laboratory module, non-linear equations of motion.
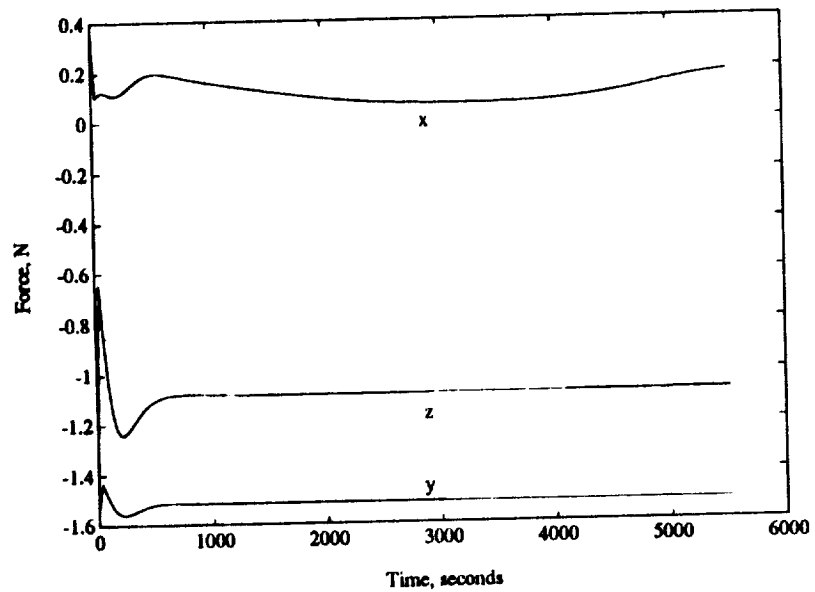
Figure 44-3 Requested control force, non-linear equations of motion.

Figure 44-4 shows the output of the SSF jet select logic. These forces are not the same as the results from sections 4.1.and 4.2 that used the linear programming techniques. The jet select logic used by this control system only considers firing six thrusters during each firing

4-20
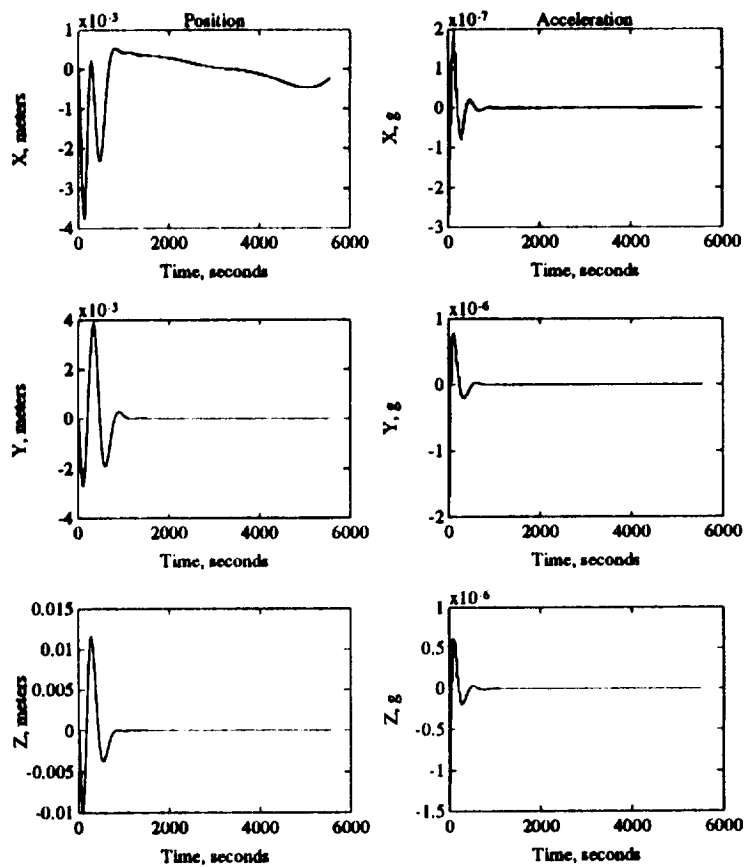
Figure 44-2 Relative position and acceleration of the proof mass, non-linear equations of motion.

period. The linear programming techniques, discussed in section 3.4, can fire all ten thrusters, if necessary, during a 33 second firing period. Both systems apply the same amount of force and torques to SSF, but just do it in different ways.

With the exception of the applied thruster forces, the results from the non-linear equations of motion match very closely those obtained from the linear equations and presented in sections 4.1 and 4.2. This correlations lends credence to the linearization process performed on the equations of motion and the control laws developed from these equations. While the current SSF jet select logic with the maximum 6 jet selection requires higher thrust values, modifying it to

4-21
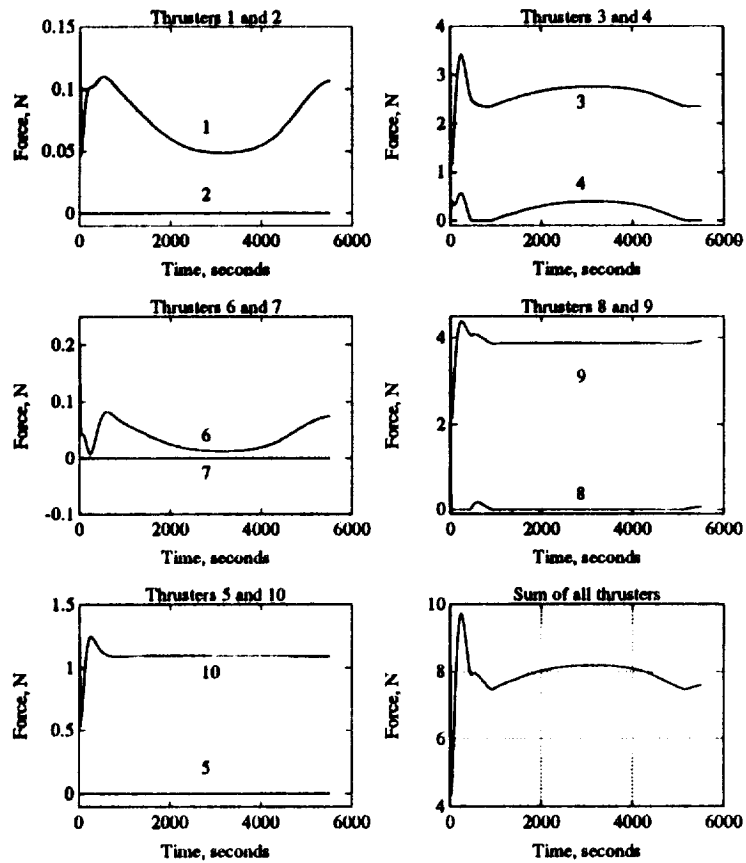
Figure 44-4 Applied thruster forces, non-linear equations of motion.

use all ten thrusters would require extensive changes to the software.

4.5 IMPACT ON SPACE STATION FREEDOM

This section will describe the impact of the MESYS on the operation of SSF. This will include an assessment of the extra fuel and electrical power required by the MESYS.

4.5.1 Propellant Requirements

As stated in section 2.1.7, each propulsion module is capable of holding up to 10,032 lbm or 4,560 kg of hydrazine fuel. In the current assembly schedule, the propulsion modules will

C - 2

be delivered on the second assembly flight and will fulfill all operational requirements until the ninth assembly flight when the next propellant supply is delivered. Each propulsion module is currently planned to be launched with only 2,850 lbm of fuel[11].

Using the applied thruster forces from sections 4.1 and 4.2, the MESYS will require 23.36, 22.16 and 45.82 lbm (10.62, 11.89 and 20.83 kg) of fuel for one orbit of operation at minimum, average and maximum atmospheric conditions, respectively, assuming each thrusters has an I_{sp} of 300 seconds. This translates to 12,545, 11,161 and 21,996 lbm, (5702, 5073 and 9,998 kg) respectively, for 30 days of MESYS operation. Therefore, 5,457 lbm (2,480 kg) of fuel will be required from the upper propulsion module and 7,096 lbm (3,225 kg) from the lower propulsion module if minimum atmospheric conditions are anticipated. If average atmospheric conditions are anticipated, 3,790 lbm (1,804 kg) of fuel will be required from the upper propulsion module and 7,192 lbm (3,269 kg) from the lower propulsion module. And, if maximum atmospheric conditions are anticipated, 2,239 lbm (1,018 kg) of fuel will be required from the upper propulsion module and 19,756 lbm (8,980 kg) from the lower propulsion module.

4.5.2 Electrical Requirements

MTC has the ability to generate a minimum of 18.75 kw of electrical power from the solar arrays and batteries. Current housekeeping power requirements are estimated to be 9.2 kw[9]. This leaves 9.55 kw to power user loads (i.e. experiments) and recharge the batteries. An augmented catalytic thruster created by F.X. Mckevitt and C.I. Miyake at Rocket Research Corporation was used as a reference thruster. It has demonstrated specific power of 5.5 watts/millipound. Based on this, it is estimated that the MESYS will require a maximum of 7.66 kw, 7.41 kw and 16.06 kw of power during minimum, average and maximum atmospheric

4-23

conditions, respectively. This requirement would leave little, if any, power for laboratory experiments.

5.0 MESYS PERFORMANCE AT PMC

This section describes the results obtained when the MESYS was evaluated on SSF PMC. The section includes the results of the proof mass and acceleration feedback control systems, a description of the thruster force ranges required and an assessment of the impact on SSF.

5.1 ANTICIPATED PERFORMANCE AT PMC

A study was performed to examine the performance of the MESYS at the PMC configuration. The proof mass control system was evaluated over an orbit using the mass properties for PMC. Figure 51-1 shows the position and acceleration of the proof mass relative to SSF during the first orbit of operation with average atmospheric conditions. The results are very similar to those observed at MTC. Also, the same control gains are used at PMC as were used at MTC even though the mass properties have changed. This can be done because the gains calculate the acceleration required to control SSF and that acceleration is multiplied by the mass to get the required control force. If the gains directly calculated the control force, then a change in mass properties would require a change in the control gains.

The acceleration feedback control system was also evaluated over an orbit with the PMC mass properties. Figure 51-2 shows the acceleration level in the U.S. laboratory module during the first orbit of operation with average atmospheric conditions. Again, the results are very similar to those observed at MTC.

Figure 51-3 shows the requested control force from the proof mass control system. The acceleration feedback control system requires almost exactly the same control forces. Figure 51-4 shows the output of the linear programming algorithm which was modified to include the 10
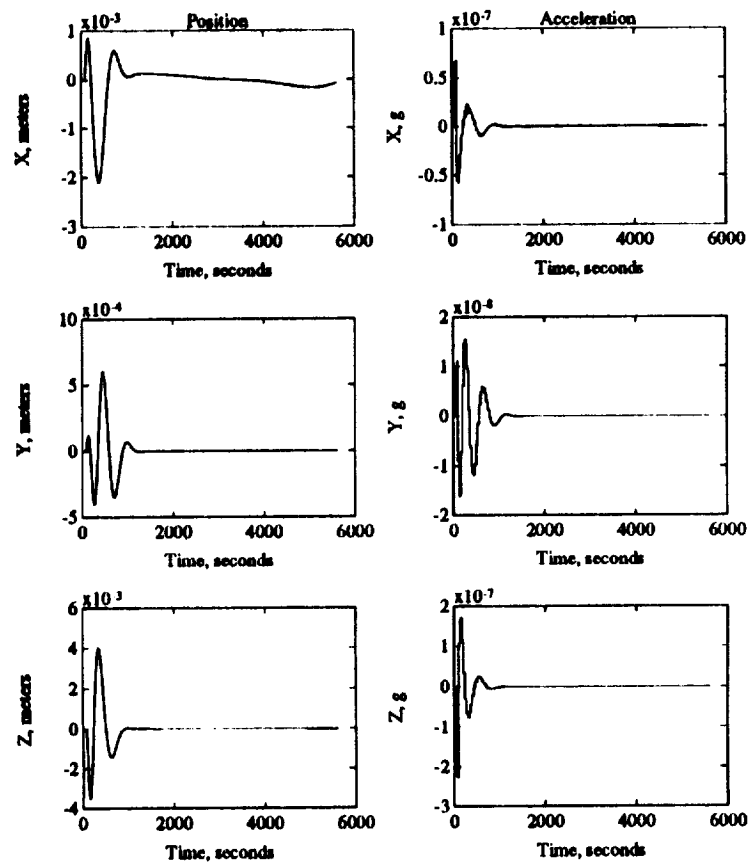
Figure 51-1 Relative position and acceleration of the proof mass, PMC.

extra jets. Notice how the total required force is less than that observed at MTC. There are a number of reasons why this is so. At PMC the center of mass is much closer to the center of the laboratory module. At MTC the position vector of the laboratory module from the center of mass is | 2.72 -12.93 3.10 | meters while at PMC the position vector is | 4.72 -4.94 2.52 |. Even though the biggest change is in the y direction, the change in the z direction, while much smaller, is also significant since gravity gradient forces in the z direction increase 3 times as fast as forces in the y direction. Another advantage of PMC is the additional propulsion modules and the symmetry they bring to the applied thruster forces. This symmetry makes the thrusters much
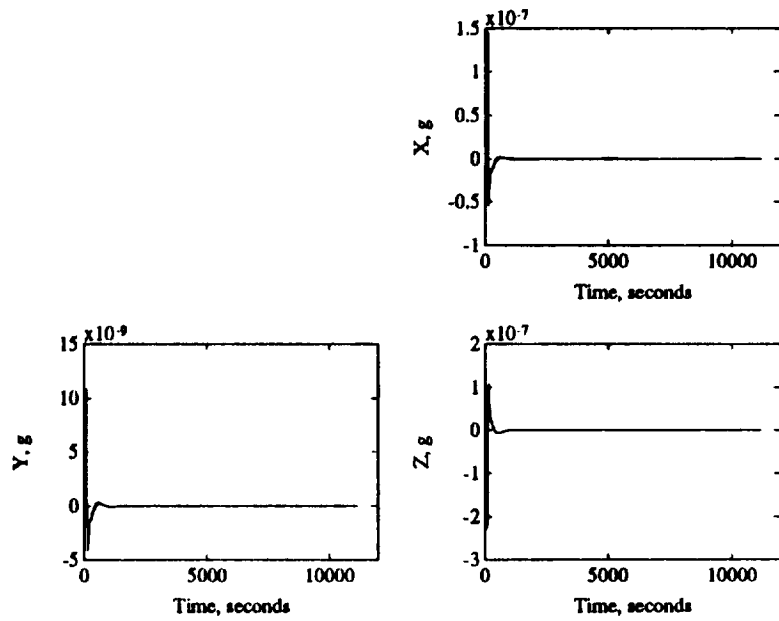
Figure 51-2 Acceleration in U.S. laboratory module, PMC.
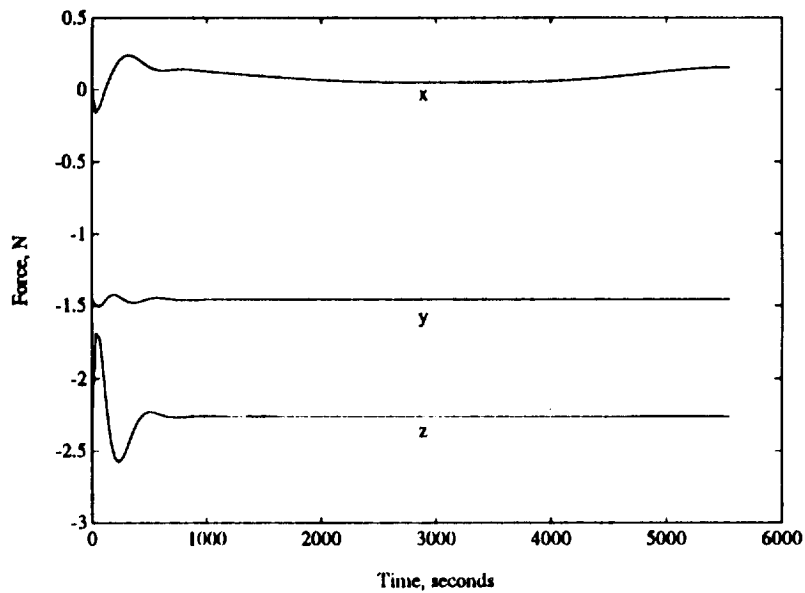
Figure 51-3 Requested control force, PMC.

more efficient at apply the required control torques. And finally, the center of pressure of the

x face for PMC is also much closer to the center of mass than for MTC. Therefore the drag

force will have a smaller moment arm and apply a smaller torque.
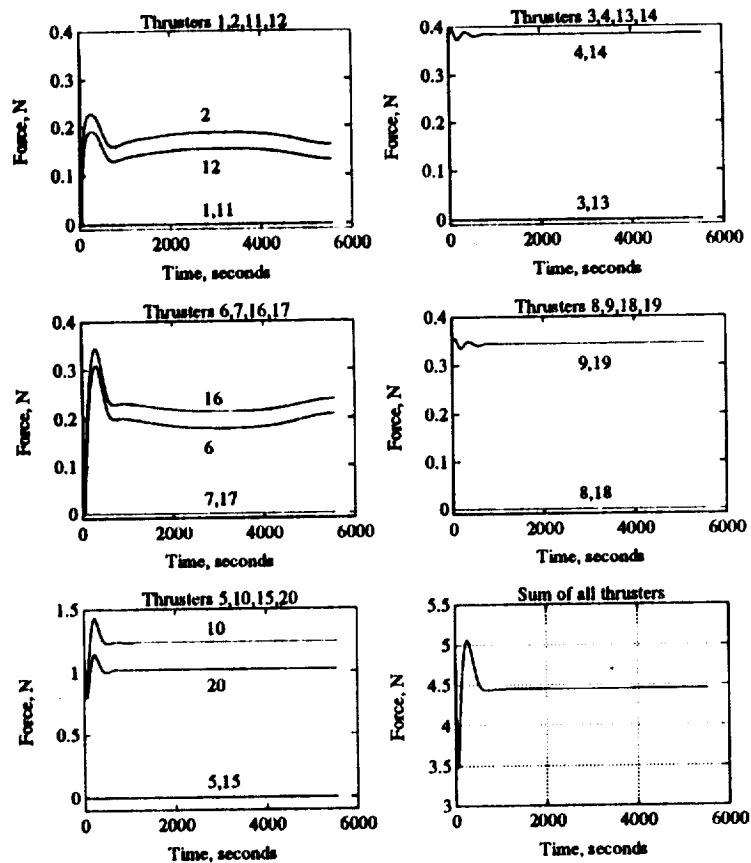
Figure 51-4 Applied thruster forces, PMC.

The MESYS was also tested on PMC during periods of maximum atmospheric conditions. Figure 51-5 shows the position and acceleration of the proof mass relative to SSF during these conditions. Figure 51-6 shows the acceleration level in the laboratory module from the acceleration feedback system. Again these results are very similar to those observed in section 4.1 and 4.2. The maximum displacement of the proof mass is on the order of 40 mm, as observed in section 4.2. Figure 51-5 and Figure 51-6 show that both the proof mass and acceleration feedback systems are capable of reducing the acceleration level in the laboratory module to below 10^{-8} g's.

Position

0.01

0

-0.01

-0.02

-0.03

-0.04

X, meters

0   2000   4000   6000

Time, seconds

x10^{-6} Acceleration

1

0.5

0

-0.5

-1

-1.5

X, g

0   2000   4000   6000

Time, seconds

0.5 x10^{-3}

0

-0.5

-1

Y, meters

0   2000   4000   6000

Time, seconds

2 x10^{-6}

1

0

-1

-2

Y, g

0   2000   4000   6000

Time, seconds

2 x10^{-3}

1

0

-1

-2

-3

Z, meters

0   2000   4000   6000

Time, seconds

1 x10^{-7}

0.5

0

-0.5

-1

-1.5

Z, g

0   2000   4000   6000

Time, seconds
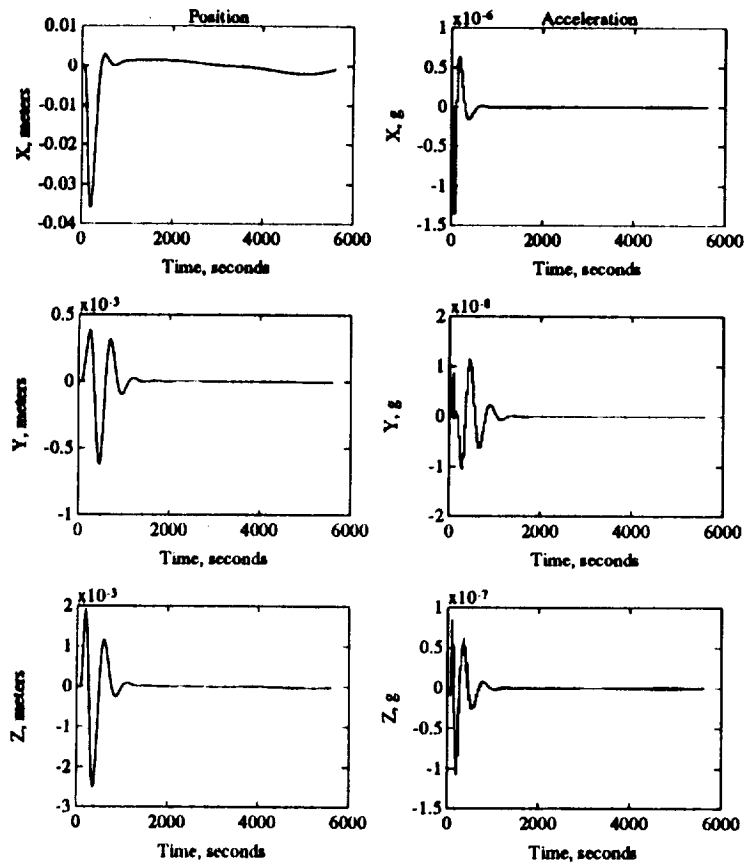
Figure 51-5 Relative displacement and acceleration of the proof mass, maximum atmospheric conditions, PMC.

Figure 51-7 shows the requested control force during maximum atmospheric conditions. As was observed in sections 4.1 and 4.2, the primary difference between this control force and the control force from the average atmospheric conditions is the force in the x direction which is control atmospheric drag. Figure 51-8 shows the applied thruster forces for maximum atmospheric drag. As was discussed previously, these results are much better than the results observed in sections 4.1 and 4.2 due to the better characteristics of PMC.

Figure 51-9 shows the position and acceleration of the proof mass relative to SSF during periods of minimum atmospheric conditions. Figure 51-10 shows the acceleration in the
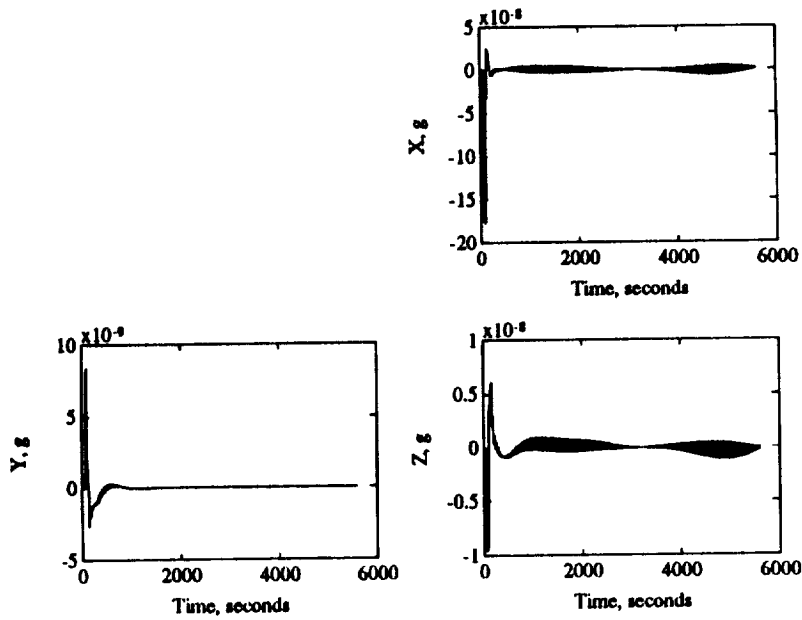
Figure 51-6 Acceleration in the lab module, maximum atmospheric conditions, PMC.
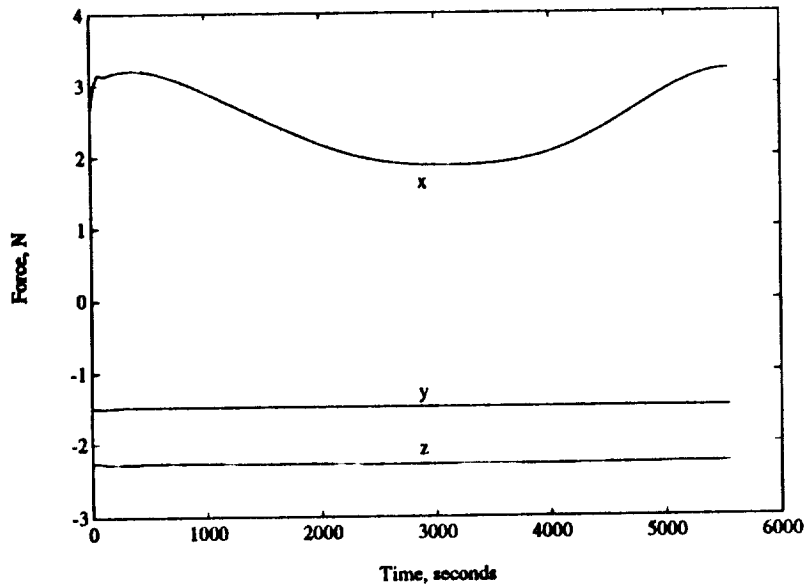
Figure 51-7 Requested control force, maximum atmospheric conditions, PMC.

laboratory module from the acceleration feedback system under conditions of minimum atmospheric drag. These results again show that the MESYS is capable of removing external accelerations to a level below 10^{-8} g's.

5-6
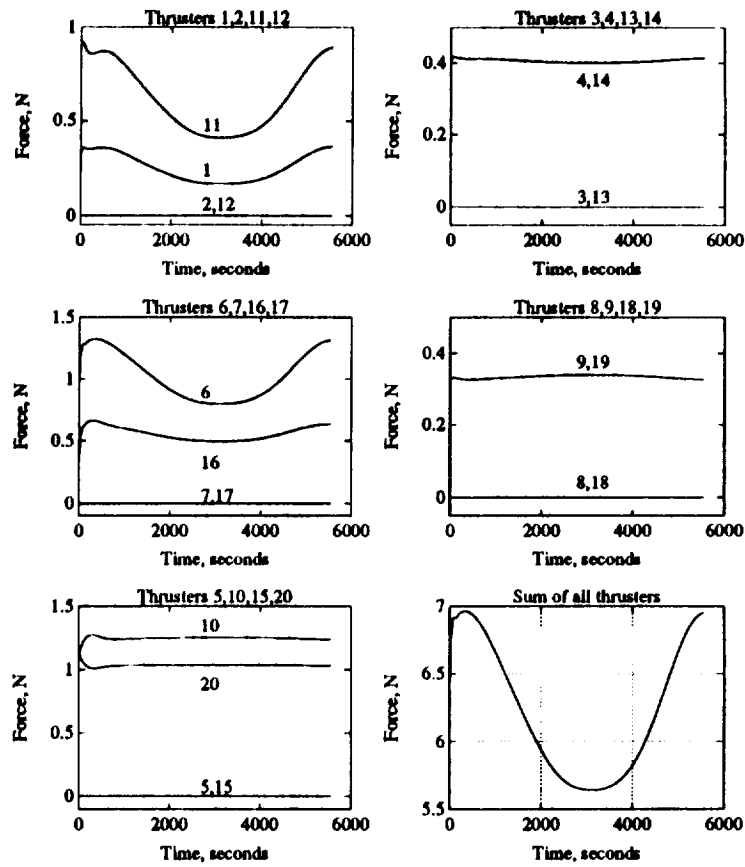
Figure 51-8 Applied thruster forces, maximum atmospheric conditions, PMC.

Figure 51-11 shows the requested control force for minimum atmospheric conditions. Again, the principle difference between this force and the previous forces is the force in the drag compensating x direction. Figure 51-12 shows the output of the linear programming algorithm in the form of the applied thruster forces.

5-7
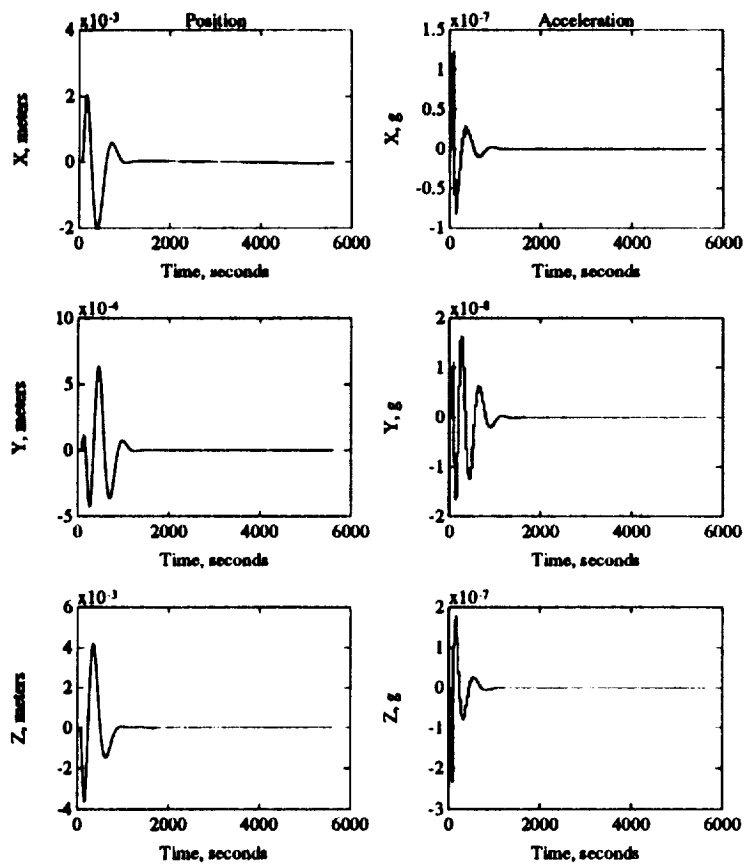
Figure 51-9 Relative position and acceleration of the proof mass, minimum atmospheric conditions, PMC.
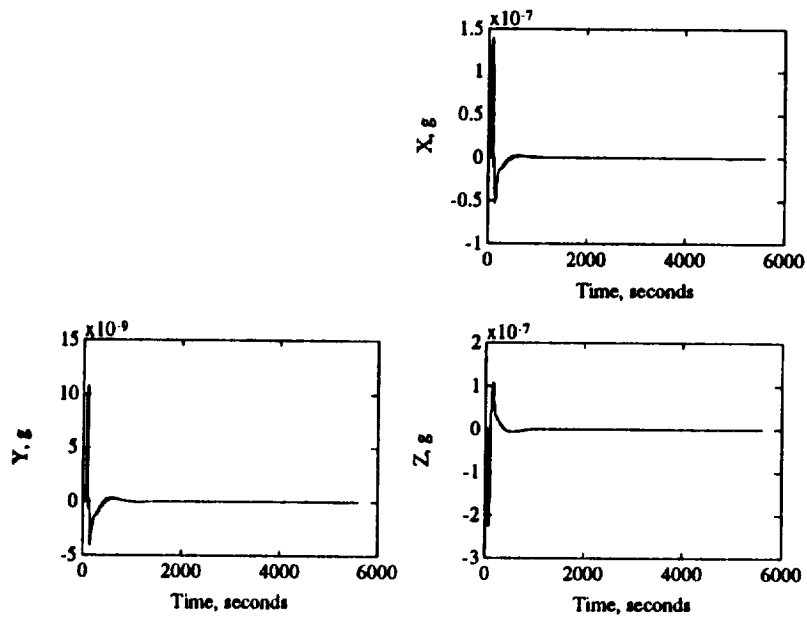
Figure 51-10 Acceleration in the lab module, minimum atmospheric conditions, PMC.
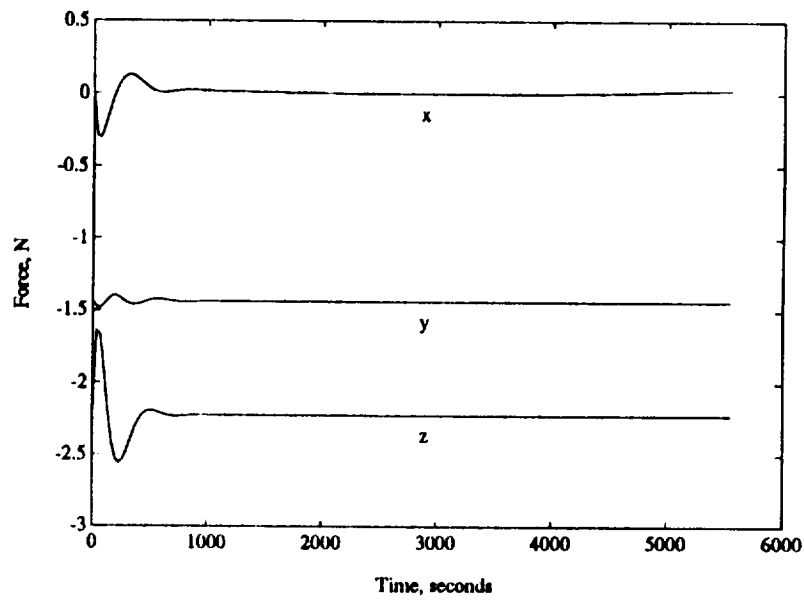
Figure 51-11 Requested control force, minimum atmospheric conditions, PMC.
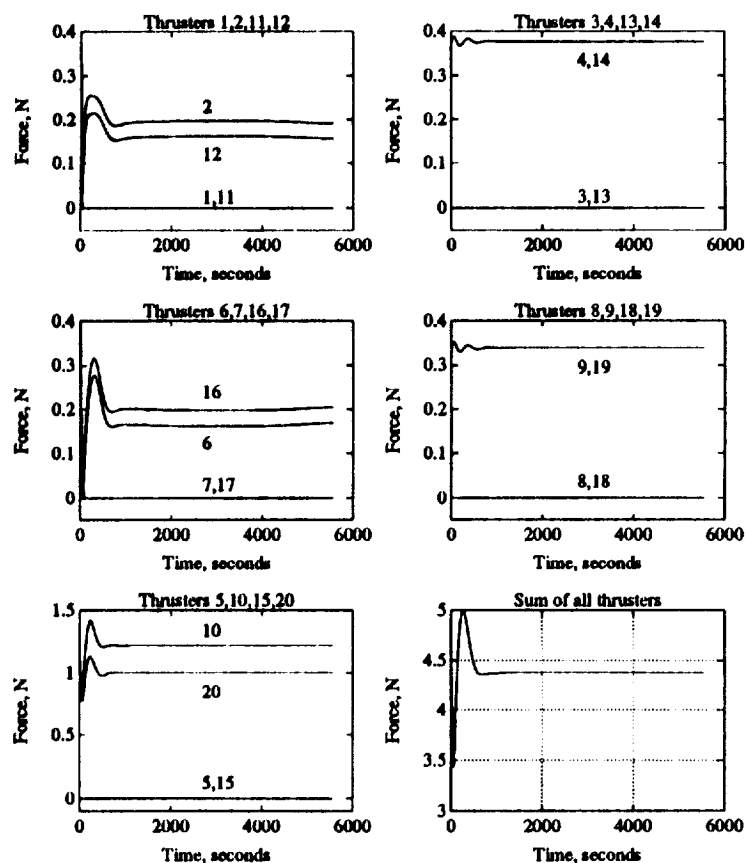
Figure 51-12 Applied thruster forces, minimum atmospheric conditions, PMC.

5.2 THRUSTER REQUIREMENTS

As was the case at MTC, the primary cause for the variation in the applied thruster force is atmospheric drag. Table 52-1 shows the steady state thruster requirements for PMC. When compared with the results from section 4.3, the thrusters at PMC require a much smaller dynamic range. The maximum dynamic range for any single atmosphere is approximately 2, for thrusters 1, 6 and 11 during maximum atmospheric conditions. As stated in section 2.3.1, this is within the current state of the art for throttle-able arcjet thrusters. All other thrusters require a maximum dynamic range of no more than 1.25.

Table 52-1 PMC steady state thruster requirements, N.

Thruster Number	Minimum Atmosphere	Average Atmosphere	Maximum Atmosphere
1	0.0	0.0	0.409-0.890
2	0.172-0.193	0.161-0.188	0.0
4	0.377-0.378	0.383-0.384	0.401-0.413
6	0.165-0.208	0.178-0.230	0.798-1.314
9	0.339-0.340	0.344-0.345	0.327-0.338
10	1.21-1.24	1.23-1.26	1.23-1.25
11	0.0	0.0	0.167-0.3627
12	0.140-0.158	0.131-0.154	0.0
14	0.377-0.378	0.383-0.384	0.401-0.413
16	0.201-0.240	0.213-0.261	0.496-0.632
19	0.339-0.340	0.344-0.345	0.327-0.338
20	0.999-1.01	1.01-1.02	1.02-1.03
3,5,7,8,13,15,17,18	0.0	0.0	0.0

5.3 IMPACT ON PMC

This section will describe the fuel and electrical requirements required to implement the MESYS on PMC.

5.3.1 Propellant Requirements

PMC will have 6 propulsion modules to supply any thrust requirements. This study assumes that only 4 will be modified with arcjet thrusters. Recall from section 2.1.7 that each propulsion module can contain a maximum of 4,560 kg (10,032 lbm) of hydrazide propellant. Using the data from section 5.1 on the applied thruster forces, the MESYS will require 8.21 kg,

8.35 kg and 11.67 kg (18.06 lbm, 18.37 lbm and 25.67 lbm) for one orbit of operation under minimum, average and maximum atmospheric activity, respectively. For 30 days of operation, this translates to 3,940 kg, 4,008 kg and 5,601 kg (8,668 lbm, 8,817 lbm and 12,322 lbm) for minimum, average and maximum atmospheric activity, respectively. 509 kgs (1,119 lbm) of fuel is required from the upper starboard PM, 1,564 kgs (3,440 lbm) from the lower starboard PM, 480 kgs (1,056 lbm) from the upper port PM and 1,398 kgs (3,075 lbm) from the lower PM if minimum atmospheric activity exists. If average atmospheric activity, exists, 508 kgs (1,117 lbm) of fuel is required from the upper starboard PM, 1604 kgs (3,528 lbm) from the lower starboard PM, 479 kgs (1,053 lbm) from the upper port PM and 1,434 kgs (3,154 lbm) from the lower PM. And if maximum solar activity exists, 594 kgs (1,306 lbm) of fuel is required from the upper starboard PM, 2,350 kgs (5,170 lbm) from the lower starboard PM, 925 kgs (2,035 lbm) from the upper port PM and 1,734 kgs (3,814 lbm) from the lower PM.

5.3.2 Electrical Requirements

PMC contains 3 pairs of solar arrays as the primary electrical power source generating 56.25 kw of power. Using the same thruster described in section 4.5.3, it is estimated that the MESYS will require a maximum of 5.54 kw, 5.64 kw and 8.06 kw of electrical power during minimum, average and maximum atmospheric activity, respectively.

6.0 CONCLUSIONS

This section will compare and contrast the acceleration and proof mass control systems, make recommendations regarding the two systems and remark on the future work required.

6.1 SUMMATION OF RESULTS

It is feasible to operate SSF in a 'drag free' mode to improve the microgravity environment in the laboratory module. The MESYS on MTC will require thrusters ranging in thrust from 0.12 to 6.41 N, between 5,073 kg and 9,998 kg (11,161 lbm and 21,996 lbm) of hydrazine propellant and between 7.41 kw and 16.06 kw of electrical power to operate for 30 continuous days. Because of these results, it is probably only feasible during minimum and average atmospheric conditions. During maximum atmospheric conditions, MTC can not supply the propellant or electrical requirements. The MESYS on PMC will require thrusters ranging in thrust from 0.13 to 1.3 N, between 3,940 kg and 5,601 kg (8,668 lbm and 12,332 lbm) of hydrazine propellant and between 5.54 kw and 8.06 kw of electrical power for 30 days of operation. These results are much more within the capability of PMC.

6.2 MICROGRAVITY LEVEL IN THE U.S. LABORATORY MODULE

As seen in sections 4.1, 4.2 and 5.1 both the acceleration and proof mass control systems have shown the ability to control the acceleration at the center of the laboratory module to below 10^{-8} g's. With the MESYS in operation, a study similar to the one performed in section 3.3.2 was performed to examine the microgravity environment in the laboratory experiment racks. The center of the third ceiling experiment rack was chosen as the point at which to minimize the

microgravity environment. Table 62-1 shows the resulting acceleration in each experiment rack.

Refer to section 2.1.3 for experiment rack locations and nomenclature.

Table 62-1 Microgravity level in each experiment rack with MESYS, μg.

	Rack 1	Rack 2	Rack 3	Rack 4	Rack 5
Ceiling	0.0176	0.0176	0.0176	0.0176	0.0176
Starboard	0.672	0.672	0.672	0.672	0.672
Floor	1.274	1.274	1.274	1.274	1.274
Port	0.679	0.679	0.679	0.679	0.679

Even with the center of the third ceiling rack set at 10^{-8} g's (it is the acceleration in each direction that is set to below 10^{-8} g's), the starboard, floor and port experiment racks show an order of magnitude increase in acceleration even though the racks are only approximately 1.6 meters to 3.2 meters from the ceiling rack in the y and z directions. This is due to the nominal gravity gradient forces that are always present. Remember that the MESYS just shifts the gravity gradient contours to a new location. Once at that new position, the contours form as they did at the center of mass. However, the results in the starboard and port experiment racks are still close to an order of magnitude better than those observed without the MESYS in operation and there is a noticeable improvement in the floor experiment racks (see Table 33-1). And these results can be obtained over virtually any atmospheric conditions. These results are identical for both MTC and PMC, the only difference between the two being the propellant and electrical costs.

6.3 COMPARISON OF SYSTEMS

Once the initial transient response passed, the acceleration feedback system and proof mass control system performed nearly identically. Since there is no performance difference between the two, the systems can only be evaluated on their individual strengths and weaknesses.

The major advantage of the acceleration feedback system is that, by making some software changes, any point on SSF can be selected to become 'drag free'. This would be particularly usefully at PMC. During one period of MESYS operation, a point in the U.S. laboratory module could be selected to be 'drag free', while during another period, a point in the European module could be selected. A major disadvantage of the acceleration feedback system is its' calibration. Even though the OARE can be calibrated in flight, it is unclear if this will have to be done during MESYS operation, and if so, what affect it would have on the performance of the MESYS during the calibration process.

The major advantage of the proof mass control system is its' simplicity. It is proven technology that has flown before. It requires no inflight calibration and is extremely accurate. However, unlike the acceleration feedback system, the proof mass system does not have the option of changing the point of 'zero g' from place to place. Once the proof mass system is installed on SSF, only that point can be made 'drag free'. If any point other than the proof mass is made 'drag free', the proof mass would remain at some point on the cavity wall and would never be recentered. This would render the proof mass useless as an accelerometer.

6.4 RECOMMENDATIONS

The following recommendations are made regarding the design and operation of the MESYS.

Due to its' ability to change the point of 'zero-g' application, the acceleration feedback control system is chosen over the proof mass control system.

The MESYS should not be operated on MTC. The high propellant and electrical requirements make it either impractical or impossible. The more efficient design of PMC (as shown in section 4.7) along with the better atmospheric conditions (the next period of minimum solar activity should begin around 2005 according to Figure 31-3) will make the MESYS more economical. In addition, the extra time will allow more development work to be done on the MESYS concept and hardware.

REFERENCES

1. National Aeronautics and Space Administration, "Space Station Freedom Program Requirements Document," SSP 3000 Rev. D, June, 1991.

2. G.L. Martin, "The Conceptual Design of a Low-Acceleration Research Facility," Masters Thesis, The George Washington University Joint Institute for the Advancement of Flight Sciences, July 1986.

3. B.O. Lange, "The Drag Free Satellite," *AIAA Journal,* Vol. 2, No. 9, pp 1590-1606, Sept. 1964.

4. K. Moe, D.B. Debra, R.A. Van Patten, M.M. Moe, G. Oelker, M.B. Ruggera, Jr., "Exospheric density measurements from the drag-free satellite TRIAD," *Journal of Geophysical Research,* Vol. 81, No. 22, pp 3753-3761, August 1, 1976.

5. B.W. Parkinson, C.W.F. Everitt, J.P. Turneaure and R.T. Parmley, "The prototype design of the Stanford relativity gyro experiment," *38th Congress of the International Astronautical Federation,* October 10-17, 1987.

6. P.G. Antreasian, J.B. Lundberg and B.E. Schutz, "Simulation of the GRM drag compensation system," *Journal of the Astronautical Sciences,* Vol. 39, No. 4, pp 487-518, October-December, 1991.

7. R.C. Blanchard, K.T. Larmen, C.D. Moats, "Flight calibration assessment of HiRAP accelerometer data," 31st Aerospace Sciences Meeting & Exhibit, January 11-14, 1993.

8. R.C. Blanchard, M.K. Hendrix, J.C. Fox, D.J. Thomas, J.Y. Nicholson, "Orbital Acceleration Research Experiment," *Journal of Spacecraft,* Vol. 24, No. 6, pp 504-511, June, 1987.

9. Grumman Space Station Division, "Stage Data Book, Stage 6, Design and Performance," SSC 18010, September 18, 1991.

10. Space Station Engineering Integration Contractor, "Space Station Freedom Microgravity Environment Definition," SSC 18270, May 15, 1992.

11. Grumman Space Station Division, "Propulsion Element performance Assessment," SSC 18410, September 12, 1991.

12. C. Tran, "The Reaction Control System for Space Station Freedom", Masters Thesis, The George Washington University Joint Institute for the Advancement of Flight Sciences, July, 1993.

13. R.C. Blanchard, J.Y. Nicholson, J.R. Ritter, "STS-40 Orbital Acceleration Research Experiment Flight Results During A Typical Sleep Period," NASA TM-104209, January ,1992.

A-1

14. J.M. Sankovic, J.A. Hamley, T.W. Haag, C.J. Sarmiento, F.M. Curran, "Hydrogen Arcjet Technology," NASA TM-105340, 1991.

15. L. Meirovitch, *Methods of Analytical Dynamics*, McGraw-Hill, 1971.

16. McDonnell Douglas Space Systems Company, "SSF Propulsion Evolution (Phase II Supplement)," MDC H0326, August 1992.

17. National Aeronautics and Space Administration, "Space Station Program Natural Environment Definition for Design," Space Station Freedom Program Office, SSP 30425 revision A, June, 1991.

18. R.A. Serway, *Physics for Scientists and Engineers I with Modern Physics*, Saunders College Publishing, 1983.

19. H. Jin, D. Debra, "Spectral Analysis of the Data From Drag-Free Satellite Triad," Stanford University, January, 1990.

20. D. Morrison, T. Owen, *The Planetary System*, Addison Wesley, 1987.

21. V.A. Chobotov, Ed., *Orbital Mechanics*, American Institute of Aeronautics and Astronautics, 1991.

22. R.L. Fox, *Optimization Methods for Engineering Design*, Addison Wesley, 1971.

REPORT DOCUMENTATION PAGE

Public reporting burden for this collection of information is estimated to average 1 hour per response, including the time for reviewing instructions, searching existing data sources, gathering and maintaining the data needed, and completing and reviewing the collection of information. Send comments regarding this burden estimate or any other aspect of this collection of information, including suggestions for reducing this burden, to Washington Headquarters Services, Directorate for Information Operations and Reports, 1215 Jefferson Davis Highway, Suite 1204, Arlington, VA 22202-4302, and to the Office of Management and Budget, Paperwork Reduction Project (0704-0188), Washington, DC 20503.

1. AGENCY USE ONLY (Leave blank)	2. REPORT DATE	3. REPORT TYPE AND DATES COVERED
	October 1993	Contractor Report

4. TITLE AND SUBTITLE	5. FUNDING NUMBERS
A Feasibility Study of a Microgravity Enhancement System for Space Station Freedom	WU 476-14-06-01 NCC1-104

6. AUTHOR(S)

Preston S. Diamond and Robert H. Tolson

7. PERFORMING ORGANIZATION NAME(S) AND ADDRESS(ES)	8. PERFORMING ORGANIZATION REPORT NUMBER
Joint Institute for Advancement of Flight Sciences The George Washington University Langley Research Center, Hampton, VA 23681-0001	

9. SPONSORING/MONITORING AGENCY NAME(S) AND ADDRESS(ES)	10. SPONSORING/MONITORING AGENCY REPORT NUMBER
National Aeronautics and Space Administration Langley Research Center Hampton, VA 23681-0001	NASA CR-191550

11. SUPPLEMENTARY NOTES

Langley Technical Monitor: Karen D. Brender
Originally published as Master of Science Thesis by the first author.

12a. DISTRIBUTION/AVAILABILITY STATEMENT	12b. DISTRIBUTION CODE
Unclassified - Unlimited Subject Category 18	

13. ABSTRACT (Maximum 200 words)

The current low frequency microgravity requirements for Space Station Freedom (SSF) call for a level of less than 1 μ-g over 50% of all the laboratory racks for continuous periods of 30 days for at least 180 days per year. While this requirement is attainable for some of the laboratory modules for the Permanently Manned Configuration (PMC), it can not be met for the Man-Tended Configuration (MTC). In addition, many experiments would prefer even lower acceleration levels. To improve the microgravity environment, the Microgravity Enhancement System (MESYS) will apply a continuous thrust to SSF, to negate the disturbing gravity gradient and drag forces. The MESYS consists of a sensor, throttle-able thrusters and a control system. Both a proof mass system and accelerometer were evaluated for use as the sensor. The net result of the MESYS will be to shift the microgravity contours from the center of mass to a chosen location. Results indicate the MESYS is not feasible for MTC since it will require 5,073 kg of hydrazine fuel and 7,660 watts of power for 30 days of operation during average atmospheric conditions. For PMC, the MESYS is much more practical since only 4,008 kg of fuel and 5,640 watts of power are required.

14. SUBJECT TERMS			15. NUMBER OF PAGES
Space Station Freedom, Microgravity			118
			16. PRICE CODE A06

17. SECURITY CLASSIFICATION OF REPORT	18. SECURITY CLASSIFICATION OF THIS PAGE	19. SECURITY CLASSIFICATION OF ABSTRACT	20. LIMITATION OF ABSTRACT
Unclassified	Unclassified	Unclassified	